5-2015

The production, properties and applications of the zinc imidazolate, ZIF-8.

John L. Tatarko Jr.
University of Louisville

THE PRODUCTION, PROPERTIES AND APPLICATIONS OF THE ZINC IMIDAZOLATE, ZIF-8

By

John L. Tatarko Jr.
B. ChE., Cleveland State University, cum laude, 2008
M.S. Chemical Engineering, Cleveland State University, 2010
M.S. Electrical Engineering, University of Louisville, 2013

A Dissertation
Submitted to the Faculty of the
J.B. Speed School of Engineering of the University of Louisville
In Partial Fulfillment of the Requirements for the Degree of

Doctor of Philosophy in Chemical Engineering

Department of Chemical Engineering
University of Louisville
Louisville, Kentucky

May 2015

THE PRODUCTION, PROPERTIES AND APPLICATIONS

OF THE ZINC IMIDAZOLATE, ZIF-8

By

John L. Tatarko Jr.

B. ChE., Cleveland State University, cum laude, 2008

M.S. Chemical Engineering, Cleveland State University, 2010

M.S. Electrical Engineering, University of Louisville, 2013

A Dissertation approved on

April 21, 2015

By the following Dissertation Committee

_____

G. Willing PhD

Dissertation Director

_____

Xiao An Fu PhD

_____

Gail DePuy PhD

_____

John Lilly PhD

_____

Jacek Zurada PhD

DEDICATION

To my parents

Finally

ACKNOWLEDGEMENTS

A heartfelt thank you to my advisor Gerold Willing, PhD and the long-time Department Chairperson, James Watters, PhD. Both have provided support and often much-needed humor. A thousand roses to the Department Business Manager Miss Pamela White and Secretary Mrs. Patty Lumley. The problems they solved were herculean in nature. My undergraduate interns Josie Stoner and Daniel Ryan were capable, friendly, and insightful. They did much of the 'heavy lifting'. My hat's off to them!

ABSTRACT

THE PRODUCTION, PROPERTIES, AND APPLICATIONS OF

THE ZINC IMIDAZOLATE FRAMEWORK ZIF-8

JOHN TATARKO

April 21, 2015

Venna, Carreon, and Jasinski produced and characterized the first samples of the zinc imidazolate framework ZIF-8 at the University of Louisville in 2010. In this dissertation the production, properties, and applications of this unique metal-organic framework are explored.

Previously, only minute laboratory amounts (1/4 gram), of ZIF-8 were produced via time-consuming and expensive processes. Production quantities have been synthesized via both a continuous and a batch process using a spray drying operation to effect separation of the solid product (ZIF-8) from the mother liquor. Approximately 85% of the mother liquor (methanol), can be recovered from the spray dryer resulting in magnitude-of-order savings in time and money.

Before any engineering applications could be suggested it was necessary to quantify important physical properties of ZIF-8 not currently available. The density, thermal conductivity, specific heat, and BET surface area were measured via strict ASTM procedures and reported. It was hoped that the massive surface area of ZIF-8 (~ 1300 m^2/g), would effect enhanced heat transfer in engineering applications.

The Heat Transfer Laboratories at the University of Louisville, served as the testing site for the use of the microparticle ZIF-8 as an agent for enhanced heat transfer when mixed in small vol% in synthetic oil. Unfortunately ZIF-8 delivered no such enhancement.

TABLE OF CONTENTS

LIST OF FIGURES

INTRODUCTION

The *Oxford English Dictionary 2nd Ed.* provides the following etymology for the term 'engineer'. First used as a recognized word in English literature in 1592, the word is derived from Late Latin through Old French, Middle English and Modern French: *ingeniatorem, engigneor, engyneour, and ingenieur.* In like manner, the term 'energy' while used by Aristotle, also finds its first appearance in an English publication in 1665. It too is derived from a Late Latin: *energia*. The modern usage of both words is intimately connected. The engineer is a **builder** and modulator of **energy.** It is my claim that any engineering activity is folly if one does not include **economics**. Thus the engineer as an agent of change harnesses scarce resources (energy and money), for the betterment of society. This dissertation is a study of the use of new materials to effect change.

The race to develop novel methods of energy production, utilization, and conservation is going to be catalyzed by the synthesis of superior materials. With radically different structures and properties than well-known (well worn) engineering materials, it is hoped that enhanced adsorption and transport properties will be welcome characteristics. *Metal organic frameworks* have emerged as unique examples of a crystalline porous material with highly desirable properties such as uniform microstructure and high surface area. The exceptional thermal and chemical stability make these ideal candidates for mass and heat transfer applications.

The *zeolitic imidazolate framework-8 (ZIF-8)* is just one of these *metal organic frameworks (MOFs)*. With unit-cell dimensions of 16.32 Å and large pores of 11.6 Å accessible through small apertures of 3.4 Å and a cubic space group (I-4_3m), it provides the surface area necessary for many transport operations. Previous researchers have investigated the use of ZIF-8 in catalysis, membrane separations, and CO_2 sequestration. However not all of the physical, transport, and thermal properties of ZIF-8 have been determined and only minute quantities have been produced during laboratory synthesis. *The intellectual thrust of this dissertation is threefold: the determination of several thermal, transport, and physical properties of ZIF-8, the design and construction of a continuous chemical process to manufacture ZIF-8, and the determination of its effectiveness in heat transfer applications.*

The specific goals of this work are:

1. The determination of the *heat capacity, thermal conductivity, density, and surface area* of ZIF-8
2. The design of a continuous chemical process to synthesize, separate, and filter ZIF-8 via *spray drying*.
3. The analysis of ZIF-8 as a nanoparticle-addition into oil-based heat transfer media

This dissertation is divided into four sections. **Part I** is an exposition of the theoretical aspects of the three specific goals mentioned above with heat transfer enhancement via nanoparticle addition to fluids the most prominent task. To date after more than 15 years of study there is still little consensus on the physical mechanisms involved. A major component of this research was the scale-up of the laboratory synthesis of ZIF-8 into a

continuous chemical process. Initially ZIF-8 was only made in minute quantities: ¼ gram at a time. It was the author's belief that a *spray drying* process could effect the separation of MOFs from the mother liquid more efficiently. Spray drying entails simultaneous heat and mass transfer and is a complex process. A properly tuned spray dryer produces a uniform controlled-size nanoparticle and the fundamentals of the spray drying process are explained in this section. In addition the principles of the reactor design and process synthesis are also proffered here.

At the heart of scientific and engineering progress is meticulous experimentation, precise data collection and thoughtful analysis. Having read hundreds of papers over the last 3 years this author has sadly come to the conclusion that much of what has been published in the so-called peer-reviewed journals is just garbage. The dross from this has seeped into our culture and nurtured a hysteria-driven media. All researchers have the cloud of *confirmation bias* hanging over their heads and responsible scientists take pains to avoid this. As much as it distresses one to see years of experimentation dashed to pieces, researchers must make an effort to *disprove* all of their hypotheses. I am passionate about education and have made an effort to train my interns in proper data collection and analysis. Tools are available for the diligent researcher to remove confirmation bias and the theory behind **best-subsets regression** and **self-organizing feature maps** (SOFMs) is exposed in **Part I.** A caution is offered here. These techniques along with *computer simulations* and *forecasting* are for use by the discriminating scientist and one should not fall in love with any one method. All models are poor representations of reality.

Part II consists of a fairly comprehensive literature review of the state-of-the-art with concentrations in heat transfer enhancement with nanofluids, spray drying, and MOFs (especially ZIF-8). A thorough search was made for commercial applications of heat transfer enhancement and even after more than 15 years of research there is a dearth of literature on any scaled-up successes. The author believes now is the time for this to change. The next step for funding on this project should be the purchase of a small HVAC chiller and the construction of a pilot-plant size cooling lab. **Part III** comprises the most important part of this dissertation; the experimental methods and results. The last two years has been devoted to a massive amount of property determination, reactor-design and construction, the study of novel separation processes (spray drying), and finally heat transfer experimentation. Adherence to scrupulous laboratory techniques and sound data collection and analysis yields meaningful results. Based on experience, it was decided to conform to strict ASTM protocols for the determination of important thermal and transport properties of ZIF-8. The actual recipes are included as appendices. The design of reactors and separation processes is the exclusive bailiwick of the chemical engineer and this researcher believes he has produced a winning scaled-up process. X-ray diffraction (XRD) studies confirm the synthesis of ZIF-8 in the continuous process which is modeled here. Molecular dynamics simulations of *Brownian motion* along with process simulations in *Simulink* are included in **Part III.** Finally, viscosity studies of the nanofluid complete the compilation of parameters necessary for the heat transfer study. Brief descriptions of equipment, computer programs for simulations, and laboratory methods are included here with the formal procedures and algorithms relegated to appendices. Careful attention to random and systematic errors along with rigorous

statistical methods was employed throughout the experimental scheme. Unfortunately this has not been a hallmark of previous researchers in the Heat Transfer Laboratory at the University of Louisville.

An analysis of the experimental results, some conclusions, and suggestions for future work comprises **Part IV**. Some have accused this author of overextending the scope of this dissertation. The presentation of a thorough and comprehensive study has been the ultimate goal and yet there is still much fodder for those wishing to further the study of novel tunable materials, especially the MOFs, and applications in renewable energy, catalysis, and carbon dioxide sequestering. In summary, this work is devoted to the discovery, synthesis, characterization, and use of novel materials (MOFs) to effect efficient and economical energy utilization. It is accomplished through mathematical and chemical engineering analysis in conjunction with rigorous laboratory experimentation.

I

THEORY

1. The Physics of Nanofluid Behavior

A nanofluid is described as an engineered *colloid* (see **Fig. I 1.3**) consisting of a base fluid infused with nanoparticles. Suspensions of these solid particles, (with major dimensions less than 100nm) flowing through a pipe, have long been thought to have the potential for enhanced transport properties. Specifically, studies[53] show that there is a substantial increase in the convective heat transfer coefficient of a nanofluid when compared to the base fluid. The increase depends on the size, geometry, and concentration of the particles along with the thermal properties of the base fluid and particles. The mechanism of heat transfer enhancement might be explained by the following proposals.

1. The thermal *conductivity* of the colloidal mixture is increased by the nanoparticles.
2. The random movement of the nanoparticles within the base fluid causes *convection* due to various *slip* mechanisms.

These convective currents flatten the temperature distribution within the nanofluid thus increasing the ΔT between the fluid and the pipe wall[54]. It is the increase in temperature

gradient that augments the heat transfer, see **Fig. I 1.1**. If the two-phase mixture behaves as a continuous Newtonian fluid the **continuity equation**, **equation of motion**, and **energy equation** act as governance for the continuum flow regime. Mathematical manipulation of these equations results in the derivation of the various forces acting on nanoparticles within the fluid-the *slip mechanisms*.

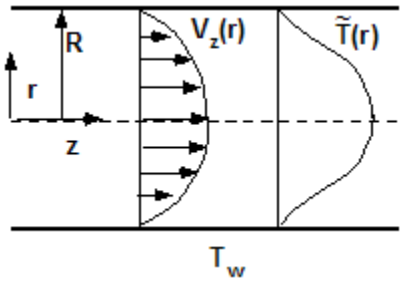

Fig. I 1.1 This is an example of the standard fully-developed fluid flow and temperature profile in a circular horizontal tube. A prevailing theory regarding the addition of nanoparticles to a base fluid suggests that the resulting thermal dispersion caused by the *slip mechanisms* 'flattens' the velocity profile causing greater Δ T between the nanofluid and the tube wall. Increased heat transfer is predicted[55].

For an incompressible, steady state, nanofluid the continuity equation becomes:

$$\nabla \cdot \boldsymbol{v} = 0 \qquad \text{(I 1)}$$

Where $\boldsymbol{v}$ is the velocity vector. Physically: what is going 'out' is what came 'in'.

Under similar conditions, the equation of motion is:

$$\rho (D\boldsymbol{v} / Dt) = -\nabla P + \mu \Delta \boldsymbol{v} \qquad \text{(I 2)}$$

Physically: the change in fluid momentum (motion) is a result of changes in pressure and the resultant viscous forces throughout the velocity field. The energy equation is:

$$\rho\,(De/Dt) = -\partial q_i/\partial x_i - P(\partial U_i/\partial x_j) - \tau_{ij}(\partial U_i/\partial x_j) \qquad \text{(I 3)}$$

Physically: the time rate of change in energy per unit volume of fluid is equal to the supply of heat per unit area per unit time, the work per unit volume per unit time and the irreversible transfer of mechanical energy into heat per unit volume per unit time.

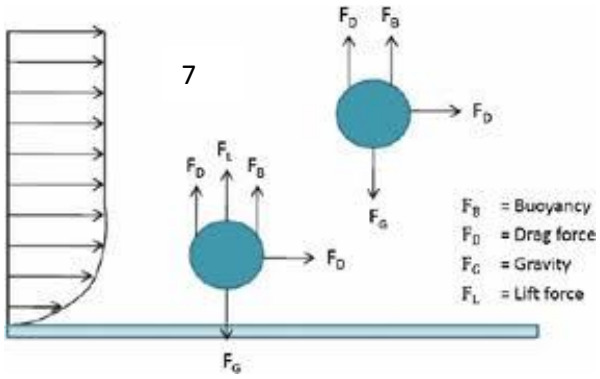

Fig. I 1.2 Here is an example of a 'flattened' flow profile and a schematic of various forces, *drag*, *Saffman's lift*, *buoyancy*, and *gravity* acting on a solitary particle infused into a fluid[55]. Now imagine the fluid with millions of these particles

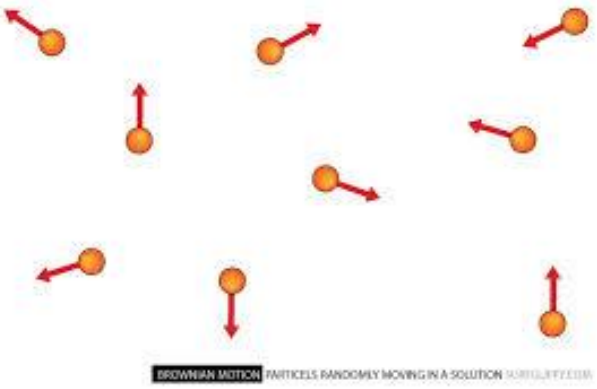

Fig. I 1.3 The chaotic random behavior of nanoparticles in a fluid known as *Brownian motion*[56]. A fluid infused with suspended particles is known as a *colloid*. Surprisingly, it is theorized that Brownian motion does little to enhance heat transfer.

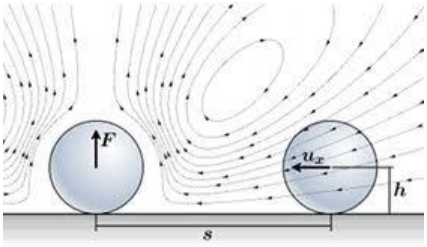

Fig. I 1.4 The *thermophoresis* effect generated in a field of temperature gradients acts in a manner vis-a-vis the field as an attractive force[57].

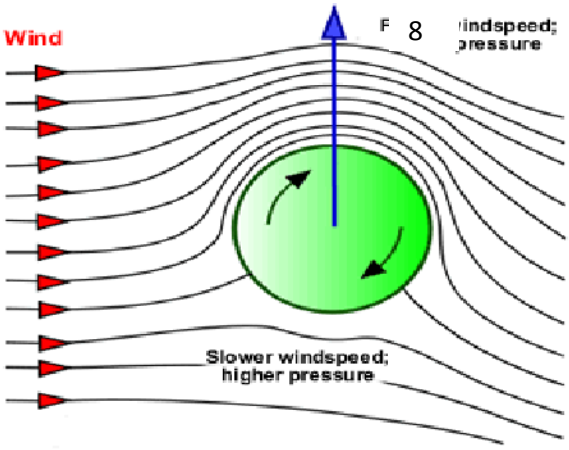

Fig. I 1.5 The *magnus* effect becomes evident in a flow field resulting in particle rotation and lift[58]. This principle describes the behavior of a curveball or 'rising' fastball thrown by a baseball pitcher.

It is theorized that the sum of behaviors depicted in **Fig. I 1.2 - Fig. I 1.5** inclusive might account for the energy exchange between the nanoparticles, base fluid, and tube wall. The term *slip mechanism* refers to the vectorial relationship between a nanoparticle and the base fluid which results in an increase or decrease in the amount of energy exchange. The forces contributing to slip, seven in number, can be deduced from a *scaling analysis* of the governing equations of the fluid continuum. Scaling analysis permits the development of tractable mathematical models of transport processes. The nanofluid is considered a

continuum if the *Knudsen* number Kn, is 'small' (Kn < 0.3). The Knudsen number is defined:

$$Kn = \lambda / d_p \tag{I 4}$$

where d_p is the is the nanoparticle molecular diameter and λ is the *mean free path* of the base fluid molecules[54]. The mean free path is defined:

$$\lambda = \frac{9}{\pi N_A P \sqrt{2}\, d_m} \tag{I 5}$$

where R is the universal gas constant, T is the absolute temperature, P is the absolute pressure, N_A is Avogadro's number and d_m is the molecular diameter of the base. The mean free path of our base fluids, *Amsoil* and *Therminol 66* has been calculated as ≈ 0.250. Therefore for our ZIF-8 nanoparticles ranging in molecular diameter from 50 nm to 200 nm, the nanofluid qualifies as a continuum. Viscosity studies of the nanofluid will experimentally confirm the existence of the continuum.

The governing equations for the nanofluid then become a *mass balance* (continuity equation), a *momentum balance* (equation of motion), and an *energy balance* (energy equation) around the system. It is helpful and clarifying to consider the equation of motion of the nanoparticle in the Lagrangian frame of reference.

$$m_p (dv_p/dt) = \sum F \tag{I 6}$$

$$\sum F = F_D + F_G + F_B + F_T + F_L + F_R + F_M \tag{I 7}$$

The forces affecting the nanoparticle include the drag force F_D, gravity F_G, Brownian motion force F_B, the thermophoresis force F_T, Saffmen's lift F_L, a rotational force F_R, and the Magnus effect F_M. The author presents this lengthy exposition only to emphasize the complexity of the physics involved in the behavior of nanofluids. Inter-particle dispersive forces such as Van der Waals are neglected due to the small contributions to energy exchange. All of the above forces are functions of nanoparticle concentration, geometry, the base fluid, nanoparticle velocities and densities, the thermal conductivities, and base fluid temperature gradients. Critical to the analysis is the *time scale* necessary for a

nanoparticle to *diffuse a length equal to its diameter* under each of the seven forces and it is assumed that the model system is laminar fluid flow in an horizontal circular tube. An example of *scaling analysis* is depicted in the **Sample Calculations** section of the **Appendix**.

Brownian motion refers to the random motion and collisions of the nanoparticles within the base fluid. Temperature gradients within a nanofluid impose a force on infused nanoparticles opposite to the direction of the gradient. This is known as *thermophoresis*. Freely suspended particles subjected to shear flow within a fluid experience 'lift', *Saffman's force*, and 'rotation perpendicular to flow' the *Magnus force*. It is the sum of these forces along with *gravity,* and *drag* that contribute to the degradation and/or augmentation of energy exchange.

For spherical particles, The Brownian and drag forces are only significant in nanofluids infused with particles measuring less than 10 nm in diameter[54]. *Molecular Dynamics* methods of simulation tend to corroborate the lack of any effect on energy exchange between the nanoparticle and base fluid due to Brownian motion. The other five forces

contribute to enhanced energy exchange between the nanoparticle the base fluid and tube wall due to thermal dispersion. This argument might lead to the belief that calculation of heat transfer enhancement due to the addition of nanoparticles into a base fluid would be simple and linear. More than fifteen years of experimentation disproves that[2]. Recounting our original hypothesis: heat transfer is enhanced via *conduction* and *convection* when nanoparticles are added to a base fluid. At the solid (nanoparticle)-liquid interface there exists molecular ordering (layering) which results in a type of thermal boundary layer known as the *Kapitza resistance.* This phenomena deteriorates conduction. Differences in the vibrational and electronic properties of various materials cause the scattering of an energy carrier as it attempts to traverse the interface. Mathematically, this might be portrayed as an extension of Fourier's law:

$$Q = \Delta T/R = G\Delta T \qquad \text{(I 8)}$$

Where G is the thermal boundary conductance; the inverse of resistance R. There are instances where high thermal resistance is desirable; thermal isolation of components within the turbines of a jet engine. There the macro-condition can be manipulated. However for the nanofluid the effects are more pronounced and deleterious due to the microscopic scale. It is difficult to quantify G for the nanofluid.

Agglomeration (see **Fig. I 1.9**) also results in the deterioration of both the conductive and convective transport modes in a nanofluid. In addition to deteriorating the thermal performance, there are few studies measuring the effects of nanoparticle agglomeration on rotating equipment such as pumps.

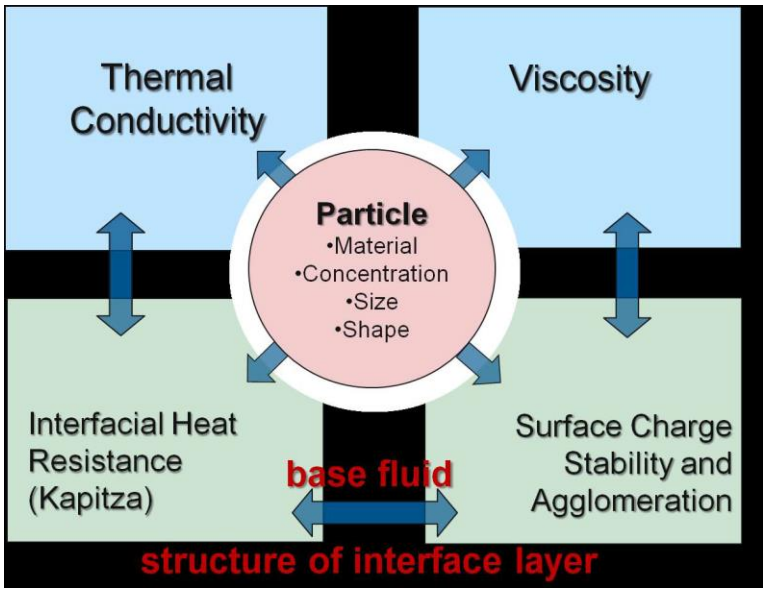

Fig.I 1.6 Timofeeva *et al.* devised a cartoon to show the various interactions at-play within the nanofluid[64]. Results from this present study corroborate the various synergies and deficiencies. Nanoparticle agglomeration in addition to decreasing effective heat transfer imposes a penalty on pumps and turbines by increasing the viscosity of the nanofluid.

A surfactant lowers the interfacial tension between a liquid and a solid permitting more intimate contact and weak bonding forces (Van der Waals). In addition to the use of surfactants, some effort has been made to quantify the effect changes in pH (surface charge) will have on nanofluid stability. This is especially pronounced when novel materials such as ZIF-8 which is highly polar (charged), are used as a nanoparticle addition.

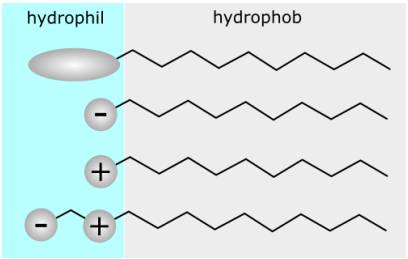

Fig. I 1.7 An example of a surfactant; one part 'loves' (hydrophil) the charged side. The other 'hates' (hydrophob) the charged side[66].

Heat transfer via *conductivity* is accomplished by electrons and phonons. Thus in addition to convective currents created through the thermal dispersion process energy is also transmitted due to point-to-point contact of the nanoparticles with the base fluid and the tube or vessel walls.. Stimulation of the crystal lattice structure of a solid results in a quantized sound wave and the generation of the pseudo-particle *phonon*. Since the sound wave has a wavelength and a wave vector (momentum), energy can be transmitted. A phonon is the smallest possible excited state of a mechanical system [68].

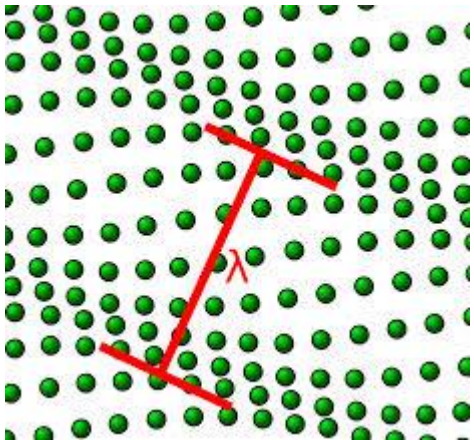

Fig. I 1.8 As the crystal lattice structure is 'stressed' the resulting wave contains energy which can be transmitted in the form of a quasi-particle-a *phonon*. This effect occurs even at extremely low temperatures and thus it might be expected to contribute to the heat transfer enhancement attributed to nanoparticle addition to a base fluid[67].

Fig. I 1.6 is a pictorial depiction of the various parameters contributing to heat transfer enhancement in the nanofluid. There exists a subtle interplay between these factors that add or detract from the effects and thus it is difficult to predict exactly what changes in each parameter might accomplish. Timofeeva[64] and her co-authors attempted to rationalize the various effects which are depicted in **Table 1** on the next page.

Table 1 Systems Engineering Approach to Nanofluid Design[64]

Nanofluid Properties	Parameters	Nanoparticle Material	Concentration	Shape	Size	Base Fluid	Zeta Potential/ Fluid pH	Kapitza Resistance	Additives	Temperature
Stability	↑↑	Δ	Δ	Δ	●↓	◌	●	x	●	?
Density	↑↑	●	●↑	x	x	●	x	x	x	x
Specific Heat	↑↑	●	●↓	x	x	●	X	x	x	Δ
Thermal Conductivity	↑↑	○	●↑	○	●↑	Δ	○	●↓	Δ	○
Viscosity	↓↓	Δ	●↓	●	●↓	●↑	●	X	○	●
Heat Transfer Coefficient	↑↑	●	●↑	●	●↑	●	●	●↓	○	●
Pumping Power Penalty	↓↓	x	●	●	●↑	●	●	x	○	●

Symbols: ● Strong Dependence ○ Medium Dependence Δ Weak Dependence x No Dependence ? Unknown Dependence

↑↑ The larger the better ↓↓ The smaller the better ↑ Increase with increase in parameter ↓ Decrease with increase in parameter

In summary, the addition of nanoparticles to a base fluid is predicted to increase the overall system heat transfer and this has been experimentally verified[53]. This effect occurs via various mechanisms some, but not all, which have been espoused in this section of the work. Of the three modes of heat transfer, it is permissible to state that *conduction* and *convection* will have the greatest effect upon engineering fluids flowing within a tube. Energy transfer via *radiation* will be negligible.

If the nanofluid exists as a continuum, the governing equations describing the fluid behavior are known as the *equations of change*: the continuity, momentum and energy equations. Scaling analysis of these equations permit the development of tractable models of nanoparticle behavior within the base fluid and consequential enhancement of transport properties.

In addition, scaling analysis of the equations of change permits the generation of various dimensionless numbers so critical to analysis of complex engineering systems. Among these are the Reynolds number **Re**, which describes fluid flow and the Peclet and Nussult numbers **Pe** and **Nu** which describe heat transfer both on macro and microscopic levels. Willing and Tatarko have been among the first to use these metrics to describe heat transfer enhancement due to nanoparticle addition to base fluids. Innovative use of simple but powerful linear and non-linear regression techniques on the experimental data generated for this study clarifies and augments the information contained in **Table 1.** This analysis comprises an important part of this dissertation. Most importantly, the intellectual thrust of this study is the improvement in the heat transfer coefficient **h**, due to the addition of nanoparticles into a flowing fluid system.

There are two different approaches to heat transfer experiments; one with constant **Q**, the heat flow, and one with constant temperature. For this study the experiments were conducted with constant heat flow.

$$h = \frac{Q}{T_w - T_f}, \tag{I 9}$$

T_w and T_f are the temperatures of the tube wall and fluid respectively. The units for **h** are J / ˚C.

$$Q = \frac{\dot{m}\ Cp\ \Delta T}{Area}, \tag{I 10}$$

Where . is the mass flow rate is in kg/s, C_p is the specific heat in J / kg˚C and the area of the flow tube is in m^2. The constant **Q** is delivered electrically via a Variac-controlled heat tape wrapped around the flow tube (see **Part III** on the experimental set-up of the heat transfer rig) and the ΔT is the difference between the inlet and outlet temperatures. Combining the two equations results in the following:

$$h = \frac{\frac{(T_o - T_i)\ Cp\ \rho\ \dot{V}}{\pi\ d\ L}}{\bar{T_w} - \bar{T_f}}, \tag{I 11}$$

Where ρ is the density in kg / m^3 and V̇ is the volumetric flow rate in m^3 / s. The symbols d and l refer to the diameter and length in meters of the heat transfer section of the flow tube.

Calculation of the Reynolds number **Re**, is among the first one makes when describing fluid flow[74]:

$$\mathrm{Re} = \frac{\text{inertial forces}}{\text{viscous forces}} = \frac{\rho \mathbf{v} L}{\mu} = \frac{\mathbf{v} L}{\nu} \qquad \text{(I 12)}$$

Where ρ is the density of the fluid in kg / m^3, v is the velocity vector in m /s, L is the characteristic length in m, and μ is the dynamic viscosity of the fluid in kg / (m*s). Reynolds numbers >> 1.00 denote a condition where the force of the fluid flow predominates over the force of the fluid viscosity. There exists a value, highly dependent on the system geometry, where the flow transitions from laminar (layered orderly flow) to turbulent (chaotic swirling flow). In a circular tube, turbulent flow occurs when **Re** > 3000. This dissertation contains studies and results from observations made during laminar flow.

Heat transfer at the boundary of a surface within a fluid is described by the Nusselt number **Nu**[74].

$$\mathrm{Nu}_L = \frac{\text{Convective heat transfer}}{\text{Conductive heat transfer}} = \frac{hL}{k} \qquad \text{(I 13)}$$

In a nanofluid, the surface of interest would occur at the nanoparticle/base-fluid interface. Intuitively, an engineer would think that analysis of the changes in **Nu** within a fluid system would characterize the heat transfer effects; k is in W / (m*K)

For the transport of heat within a flowing fluid system another dimensionless number generated from the scaling of the *equations of change* is the Peclet number **Pe**[74]**:**

$$\mathrm{Pe} = \frac{\text{advective transport rate}}{\text{diffusive transport rate}} \qquad \text{(I 14)}$$

This is the ratio of convective flow of heat (advection) to the thermal diffusion (conduction). Experimentally, Tatarko[53] has shown that the Peclet number is perhaps the best descriptor of heat transfer in a nanofluid.

The Prandtl number **Pr** is a dimensionless number often listed in material property tables for it is derived without any time-scaling of the equations of change[74].

$$\mathrm{Pr} = \frac{\nu}{\alpha} = \frac{\text{viscous diffusion rate}}{\text{thermal diffusion rate}} = \frac{c_p \mu}{k} \qquad \text{(I 15)}$$

The **Pr** characterizes the relative thickness of the velocity boundary layer to the thermal boundary layer[74]. The Peclet number is the product of the Reynolds number and the Prandtl number.

$$\mathbf{Pe} = \mathbf{Re} * \mathbf{Pr} \qquad \text{(I 16)}$$

For mass transfer applications, the Schmidt number **Sc**, relates the momentum boundary layer to mass diffusion boundary layer{74}:

$$\mathrm{Sc} = \frac{\nu}{D} = \frac{\mu}{\rho D} = \frac{\text{viscous diffusion rate}}{\text{molecular (mass) diffusion rate}} \qquad \text{(I 17)}$$

Where D is the mass diffusivity in m^2 /s and υ is the kinematic viscosity in m^2 / s.

The Peclet number is the product of the Reynolds number and the Schmidt number.

$$\mathbf{Pe} = \mathbf{Re} * \mathbf{Sc} \qquad \text{(I 18)}$$

These dimensionless numbers contain the independent variables that comprise the transport system and thus are helpful when submitting the experimental data for statistical

analysis. It is instructive to note that this researcher has shown[53] that just as in the analysis of real chemical reactors, the condition of fluid flow is critical to the analysis of heat and mass transfer effects due to nanoparticle behavior. This is evident in the data obtained for heat transfer calculations and that also obtained for the calculation of simultaneous mass and heat transfer phenomena present during spray drying. The *slip mechanisms* that drive convective heat transfer during fluid flow within a circular tube are also responsible for the same effect within the cyclone during spray drying.

A literature search (**Part II)** of the latest research in the theoretical, computational, and experimental underpinnings of the physical mechanisms responsible for nanoparticle assisted heat transfer yields little consensus even after 20 years of study. The phenomenon is complex and a unified theory may never become available. This underscores the gravity of well-designed empirical data collection and analysis. The mechanisms and theoretical analysis proffered in this section of **Part I** are as plausible and valid as those espoused in any number of journals. Finally, in this section we discuss the validity of Brownian motion as one of the slip mechanisms responsible for the enhanced heat transfer behavior of nanoparticle infused base oils.

From kinetic theory[75]: $\kappa_B = D_B * C_p$

Where: κ_B is the thermal conductivity of the nanoparticle

D_B is the thermal diffusivity of the nanoparticle

C_p is the specific heat of the base fluid.

Likewise for the base fluid: $\kappa_F = D_T * C_p$

Then: $\kappa_B / \kappa_F = D_B / D_T$

The ratio of the Brownian motion contribution to thermal conductivity to the thermal conductivity of the base fluid is denoted by the ratio of the nanoparticle diffusivity to the thermal diffusivity of the base fluid[75]. As an example in a water suspension:

Let the nanoparticle have a radius: $r = 5$ nm

D_T for water is: $D_T = 1.4 * 10^{-7}\ m^2 / s$

η the viscosity for water is: $\eta = 1.3 * 10^{-3}\ kg/m\ s$

The Stokes-Einstein formula: $D_B = k_B * T / \eta * 6 * \pi * r$

Where k_B Boltzmann's constant; $k_B = 1.4 * 10^{23}\ J / K$

Yields: $D_B = 4.5 * 10^{-11}\ m^2/s$

Then : $\kappa_B / \kappa_F = D_B / D_T = 3.2 * 10^{-4}$

The very small ratio shows that Brownian motion has little effect on thermal transport[75]. Heat transfer via conduction (thermal diffusivity D_T) is faster than particle diffusivity D_B. This can be shown experimentally via simulation (**Part III**).

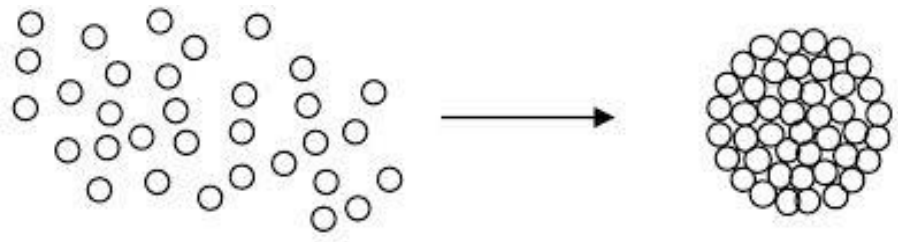

Fig. I 1.9 Thermodynamically, all systems seek to minimize the total free energy and the surface energy in particular. As the surface area is maximized, the free energy decreases. This leads to particle **agglomeration**. For a nanofluid this condition results in a decrease in performance due to the loss of thermal dispersion[59]. Nanoparticle agglomeration can be avoided by providing suitable *surfactants* which maximize the attractive forces between unlike molecules compared to those of like molecules.

2. The Zeolitic Imidazolate Framework ZIF-8

Zeolitic imidazolate frameworks (**ZIFs**) are a subclass of metal organic frameworks (**MOFs**). Like traditional **zeolites,** high surface areas, cage-like structures and thermal, mechanical, and chemical stability are well represented within this class of materials. In ZIFs, a metal such as zinc is linked through nitrogen atoms by ditopic **imidazolate** to form neutral frameworks. Proper synthesis and curing methods results in tunable pore sizes formed by the 4-,6-,8- and 12-membered-ring ZnN_4. The well-studied[47] ZIF-8 has large pore diameters of 11.6 Å and has been suggested as a candidate for catalysis, carbon dioxide sequestration, and other novel separation processes. Because of ease of synthesis; common materials and room-temperature reaction conditions, and a relatively large surface area we propose ZIF-8 as a nominee for use in the study of nanoparticle-enhanced heat transfer media. Willing and Tatarko have studied the effects of copper nanoparticles introduced into oil-based fluids at low wt% with resulting heat transfer enhancement up to 25%. The full mechanism explaining this phenomenon is a source of intense research and some heated debate.

In contrast to the basic zeolitic structure, ZIF-8 uses the **imidazole** structure as a bridge instead of oxygen: (T-Im-T). **Fig.I 2.2** shows a schematic of this polar, planar 5-membered ring with the formula: $(CH)_2N(NH)CH$. Imidazole is amphoteric, that is, it can act as either an acid or base. While this fact is not especially important for physical applications such as heat transfer, this **organic linker** provides adsorption sites necessary for carbon dioxide capture which can then react at the Zn vertices of the structure. **Fig. I 2.3** exemplifies the synthesis pathway of ZIF-8. The polarity of the imidazole molecule requires consideration when introducing these structures into nonpolar oils.

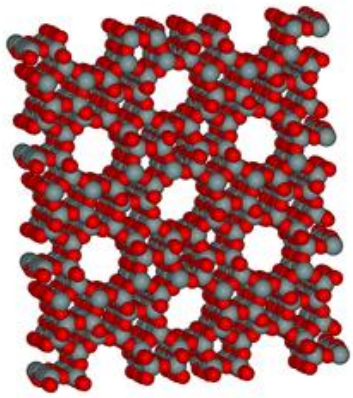

Fig. I 2.1 The basic **zeolite** structure of ZSM-5 showing cage-like formations and a microporous crystalline structure. Over 206 different frameworks have been identified and synthesized. About 40 occur in nature[88]. ZSM-5 consists of **pentasils**; 8 five-membered rings. Like all zeolites, **oxygen** acts as a **bridge** between the metals (T-O-T, where 'T' is a metal). In this case silicon and aluminum are at the vertices.

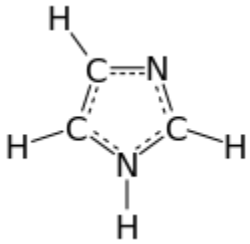

Fig. I 2.2 The imidazole molecule has a proton (H^+), which can be located on either of the nitrogen atoms resulting in 2 tautomeric forms. Because it is polar it is readily soluble in water yet it is also **aromatic** due to the presence of 2 π-electrons on the protonated nitrogen and one π-electron from each of the other 4 members of the ring. This molecule acts as an organic linker in the ZIF-8 structure[47].

In a typical synthesis, 0.3 g of zinc nitrate hexahydrate [$Zn(NO_3)_2{\cdot}6H_2O$], is dissolved in 11.3 g of methanol and stirred vigorously. A solution of 0.66 g of 2-methylimidazole [$C_4H_6N_2$], and 11.3 g of methanol is simultaneously prepared, added to the former

solution, and stirred for various times. The resultant product, suspended particles, is twice washed and centrifuged at 3000 rpm. **The yield is quite small**; less than 0.25 g.

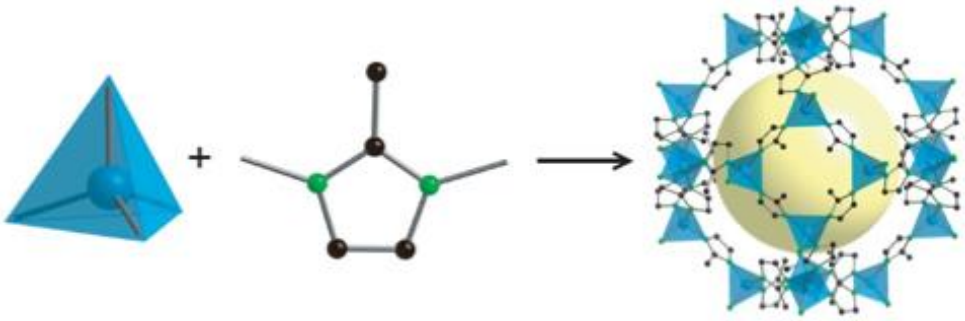

Fig. I 2.3 The synthesis of ZIF-8 is depicted by the addition of the ZnN_4 tetrahedra with the imidazole molecule. Carbon atoms are in black and the nitrogen molecules are green. Hydrogen has been omitted. The yellow inscribed sphere represents the maximum size of any adsorbed molecule. Amazingly, it has been reported that the ZIF-8 structure has a surface area of up to $2000m^2$ per gram[47,49]. All transport phenomena and heat transfer in particular are highly dependent upon surface area.

Venna, Jasinski, and Carreon[49] have pioneered the synthesis and characterization of the zeolitic imidazolate framework, ZIF-8. Of paramount importance is the elucidation of the crystalline growth kinetics via the **Avrami** model. **Fig. I 2.4** a schematic of the transformation, reveals 3 separate regions.

The dependence of transformation on pH leads to the belief that some solution-based metastable phase initiates the crystal growth and coexists in equilibrium with increasing population of ZIF-8[49]. Since we know the *residence times* necessary for the size of ZIF-8 crystal desired and the kinetics of growth it is possible to design a *continuous stirred-tank reactor* (CSTR), for a chemical process whether it be a **batch** or **continuous process**. As the reaction occurs in methanol, a flammable solvent, a nitrogen 'blanket' on

the mixing, reaction, and separation portions of the process is required. Thus, the CSTR makes the most sense in choice of reactors.

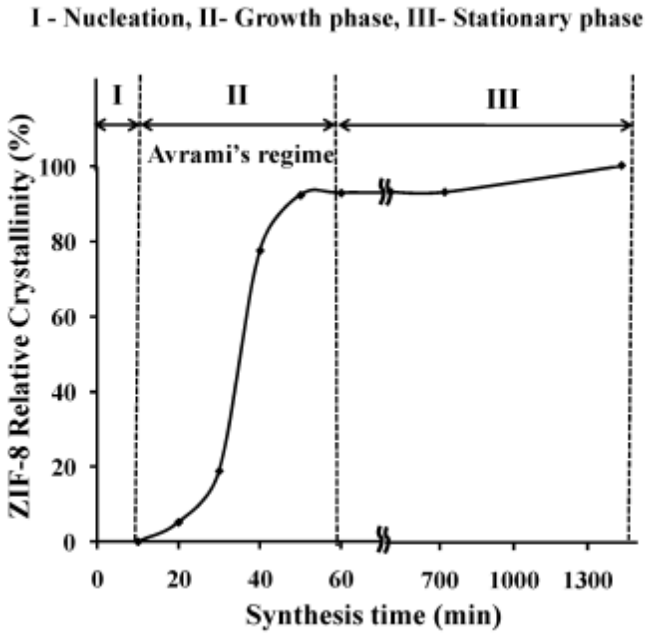

Fig. I 2.4 A plot of the growth of ZIF-8 crystals via Avrami kinetics: $y= 1-exp(-kt^n)$. In this case k, the scaling constant = 5.1 x 10^{-7} and n ≈ 4. Interpretation of the values for **n** follows some loose guidelines. Here a value of 4 suggests random homogeneous nucleation within the parent liquor resulting in spherical shapes[84]. *Region I* corresponds to the **nucleation phase** which establishes the conditions for crystal growth. The majority of transformation occurs in *region II* and there is little further change in *Region III*.

ZIF-8 is a highly polar molecule and its infusion into a base oil as an agent of heat transfer enhancement must be accompanied by a surfactant (cf. **Fig. I 1.8**). Aggregates of these are known as *micelles*. The action of these agents may be classified as **adsorption**, which signifies attachment **onto** a surface rather than **into** it (**absorption**).

Adsorption occurs by way of to 2 different mechanisms; *chemisorption* and *physisorption*.

Physisorption is a relatively weak mechanical or electrostatic process which results from van der Waals attraction between two different chemical species including those in different phases (gas/solid, solid/solid). The chemical properties of each species are not affected in this process which may occur continuously and on a multilayer basis. The results can be easily reversed (desorption). Thus catalysts, some of which are zeolites themselves, can be reclaimed by drying which may drive-off the adsorbed species.

Chemisorption is a strong chemically induced attraction which entails chemical bonds between the adsorbed molecule and an active site on another surface. This occurs only on a single-layer basis and might require an activation energy for initiation.

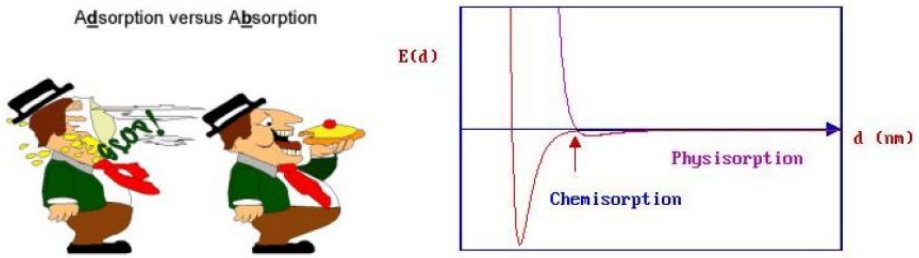

Fig. I 2.5. The cartoon above portrays the difference between the adsorption and absorption. The deep dip of the energy curve represented as chemisorption is characteristic of the strong Lennard-Jones interaction between molecules. Energies less than zero denote attraction[77]. Chemisorption is an irreversible process.

Few of the thermal properties of ZIF-8 necessary for heat transfer studies have been measured and reported in the literature. A significant portion of this dissertation is devoted to the determination of the *thermal conductivity* k, *true density* ρ, and *specific heat* C_p. The determination of total surface area of the ZIF-8 molecule via the BET method is an example of the physisorption process.

3. Spray Drying

A liquid feed consisting of a pure fluid and a solid fraction can be transformed into dried particles by a well-engineered introduction into a closed chamber with a suitable warm drying agent. This process of simultaneous heat and mass transfer is known as *spray drying.* This is a rather novel process yet applications in pharmaceuticals, foods, and fine chemicals abound. The basic theory revolves around the drying kinetics of the droplets[60]. This is not as simple as it sounds for the feed may consist of a slurry, paste, suspension (colloid), or a solution. In addition this is not an equilibrium-staged unit operation but rather a rate-based separation process. The model can be further refined by the addition of particle-particle interactions including those affected by chemistry (pH), or those physically induced such as temperature and pressure gradients and surface tension.

The spray dryer consists of an *atomizer* which transforms the liquid feed into droplets and *contact chamber* where the droplets can intimately contact a stream of hot gas usually consisting of steam or air[60]. The moisture content of the drying gas increases as droplet evaporation continues finally yielding a product of desired dryness. A detailed description of atomizer design and operation is beyond the scope of this dissertation yet it must be noted that there exist families of geometries some rotary or fixed, pneumatic or sonic, some based on gravity feed, some based on centrifugal feed…etc. The geometry and height of the contact chamber can also be varied depending on *flow* of the drying agent. A counter-current, co-current, or mixed gas flow can be used. The most versatile and well-designed (expensive!) of these spray dryers can be re-configured (atomizer and gas flow) depending on the type of feed. See **Fig. I 3.1**.

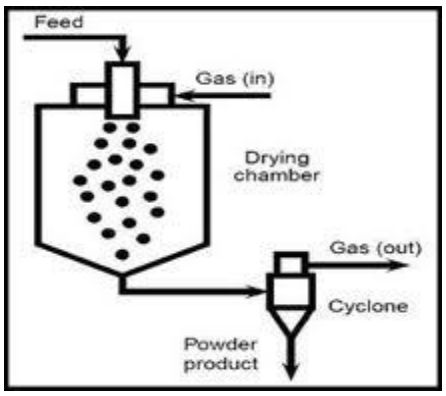

Fig. I 3.1 This is the basic schematic of the spray drying operation imbedded in a continuous chemical process. The feed and drying gas are running co-currently and it is possible to recycle the gas and liquid fraction after purging[62].

Fig. I 3.2 The Buchi B 290 Mini-Spray Dryer processed the ZIF-8 nanoparticle used for the heat transfer experiments in this study. Presently the Buchi Corporation does not make a commercial-scale dryer yet this model has been found in many continuous food and pharmaceutical operations[63].

A schematic of the drying process applicable to feeds containing soluble or undissolved solids is displayed in **Fig. I 3.3.**

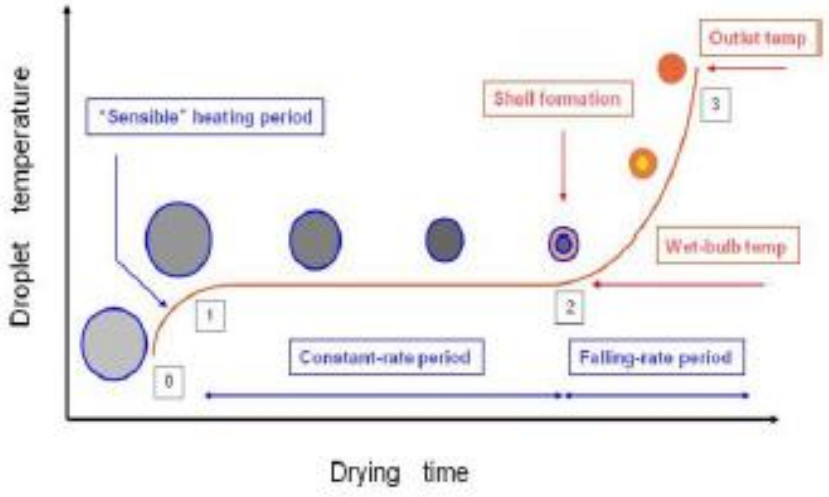

Fig. I 3.3 This schematic of the spray drying process delineates 3 specific periods in the formation of a solid particle. During the period from **0** to **1** no evaporation of solute occurs as the feed and drying gas equilibrate. During the period from **1** to **2** the evaporation of solvent is proportional to the surface area of the droplet (see **Fig. I 3.4**). In the last period of the operation **2** to **3**, the rate of evaporation of solvent decreases as solidification increases and the remaining process is diffusion rate-limited[69].

The droplet drying history is modeled after material and energy balances are performed on a spherical shell, **Fig. I 3.4**.

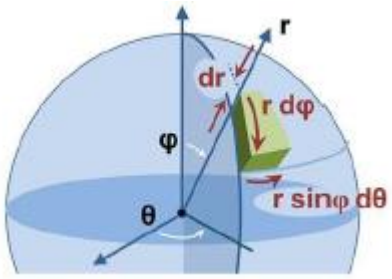

Fig. I 3.4 Since the feed droplet is spherical, temperature and concentration fields are assumed to be radially symmetric and thus for modeling purposes the θ and ψ directions contain no variations{69}.

A complete derivation of the material and energy balances for the drying kinetics of a single droplet in spherical coordinates is included in Breen[70]. In the final analysis both

Breen and Mezhericher[60] concur that the droplet drying process is controlled by the **Peclet** number **Pe**.

$$Pe = \frac{\kappa}{D} \approx \frac{evaporation\ rate}{diffusion\ rate} \qquad (I\ 1\ 9)$$

In a nanoparticle such as ZIF-8 with much porosity and the ability to trap molecules internally it is understandable that at some point solvent diffusion would predominate over evaporation in the production of a solid particle. Both κ and D are in m^2/s.

The change in the concentration of solids radially, is proportional to the concentration itself and the constant of proportionality is the Peclet number[60].

$$\frac{\partial C_i}{\partial r} = Pe \cdot C_i \qquad (I\ 2\ 0)$$

This is in fact the boundary condition for the material balance on the spherical feed droplet. The final product morphology is governed by process parameters such as temperature and flow rate of the drying gas and the latent heat and diffusion coefficient of the solute[69]. For the production of the ZIF-8 nanoparticle, the solid itself was an insoluble within the methanol solution which was almost completely recovered. Thermal and pressure gradients generated during the spray drying process are sufficient to damage the structure of fragile molecules and it is a testament to the robustness of the ZIF-8 molecule that it came out unscathed during drying.

We attempt to examine in some detail the intricacies of the transport phenomena that comprise spray drying.

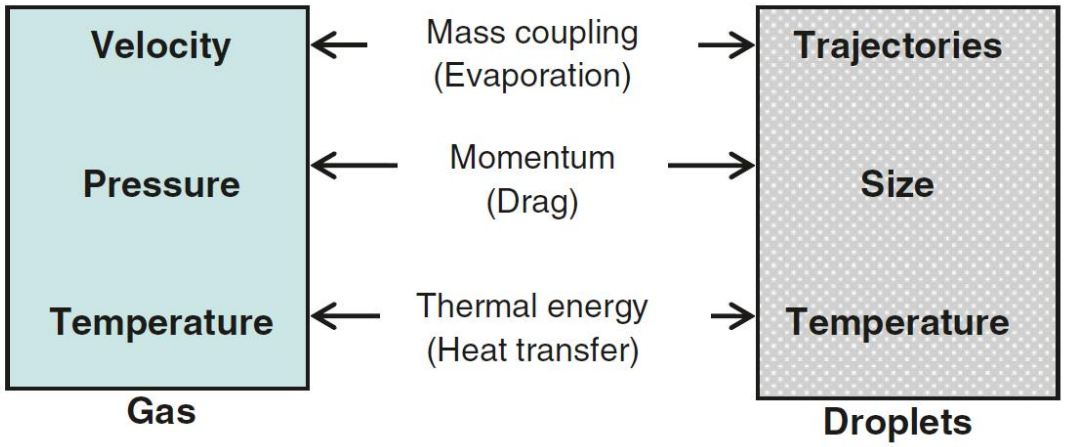

Fig. I 3.5 Within the spray drying process simultaneous heat, mass, and momentum transfer drive the conversion from a colloid/gas mixture to a discrete particle, along with a 'wet' gas, and a reclaimed solvent[76].

The heat and mass transfer between the gas and the particles is derived from the motion of the particles in the Lagrangian frame[76]:

$$m_{\mathrm{p}} c_{\mathrm{p}} \frac{\mathrm{d}T_{\mathrm{p}}}{\mathrm{d}t} = hA_{\mathrm{p}} \left(T_{\mathrm{g}} - T_{\mathrm{p}}\right) + \frac{\mathrm{d}m_{\mathrm{p}}}{\mathrm{d}t} h_{\mathrm{fg}} \tag{I 21}$$

The mass transfer rate (evaporation) between the particles in solution and the dry gas is[76]:

$$\frac{\mathrm{d}m_{\mathrm{p}}}{\mathrm{d}t} = -k_{\mathrm{c}} A_{\mathrm{p}} \left(Y_{\mathrm{s}}^{*} - Y_{\mathrm{g}}\right) \tag{I 22}$$

Where: h is the heat transfer coefficient

k_c is the mass transfer coefficient

h_{fg} is the latent heat of the colloid solution

A_p is the area of the particle

Y_s^* is the saturation humidity of the gas

Y_g is the gas humidity

The heat and mass transfer coefficients can be calculated from correlations[76].

$$Nu = \frac{hd_p}{k_{ta}} = 2 + 0.6\,(Re_d)^{1/2}\,(Pr)^{1/3} \tag{I 23}$$

$$Sh = \frac{k_c d_p}{D_{i,m}} = 2 + 0.6\,(Re_d)^{1/2}\,(Sc)^{1/3} \tag{I 24}$$

$D_{i,m}$ is the diffusion coefficient of the mother liquid vapor (in this case methane) and k_{ta} is the thermal conductivity of the parent fluid. As a review[76] the Prandtl and Schmidt numbers:

$$Pr = \frac{c_p \mu}{k_{ta}} \tag{I 25}$$

$$Sc = \frac{\mu}{\rho_g D_{i,m}} \tag{I 26}$$

4. The Design of a Chemical Reactor for the Production of ZIF-8

The design of chemical reactors is perhaps the defining characteristic of the chemical engineering profession. Something as mundane as a cigarette qualifies as a type of tubular rector yet the modeling, construction and control of actual reactors to effect efficient chemical production is complicated and often highly non-linear in nature. Lack of a realistic, mathematically tractable model inhibits the design of a control system.

The *continuous stirred-tank reactor* (CSTR) is used throughout the process industry for the continuous inflow of multi-fluid reactants resulting in the outflow of a reacted product. These types of reactors are easy to construct out of a variety of alloys or non-alloys (glass), and can be clad with a jacket for heating and/or cooling so temperature control is possible. The CSTR can be modeled as one with perfect mixing and thus it is assumed that the product composition leaving the vessel is identical to that of contents within. The product of the chemical reaction within the CSTR is a function of the *residence time* within the vessel $\boldsymbol{\tau}$, and the *rate of reaction* of component 'A' $\mathbf{r_A}$. As a choice of reactor, *conversion* within the CSTR is not optimum so a large volume is required. It is the benchmark reactor however whenever a liquid-phase reaction must be experimentally verified and it is the choice of control systems designers when testing new algorithms or hardware. PIDs, and robust controllers along with adaptive, fuzzy, and predictive-type systems have been successfully tested-on and fitted to these reactors.

The performance equation for the CSTR is:

$$V / F_A = X_A / -r_A \qquad \text{(I 27)}$$

Where V is the reactor volume, F_A is the flow rate of component A, X_A is the conversion of component A, and r_A is the reaction rate of component A.

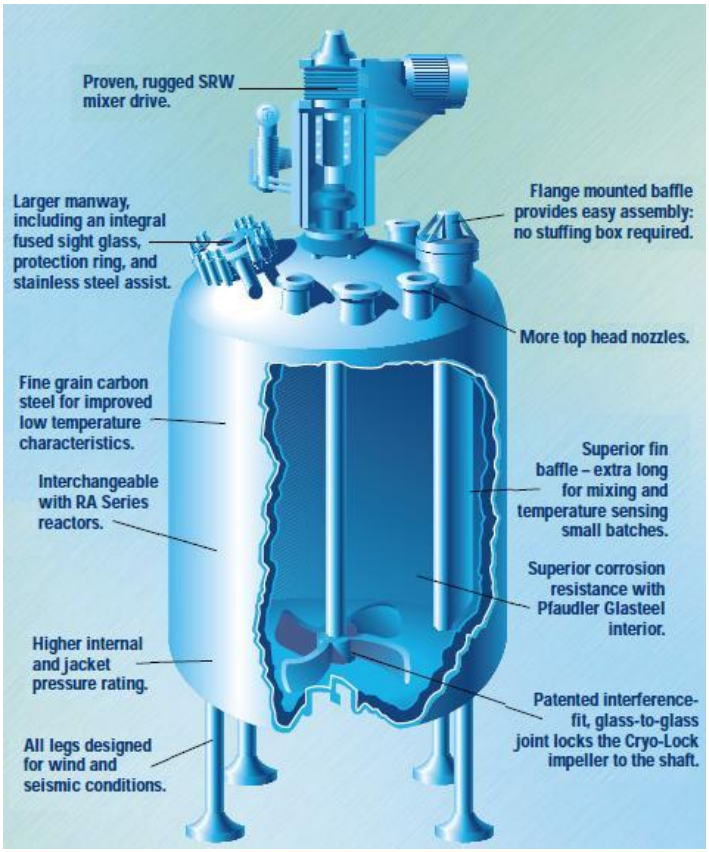

Fig. I 4.1 This reactor designed by Pfaudler Inc is the perfect example of a Continuous Stirred Tank Reactor (CSTR)[66]. This particular model is glass-lined for the production of highly corrosive materials Our nanoparticle ZIF-8 may best be produced in a reactor of this type.

The *residence time* τ, is the average amount of time a discrete quantity of reagent spends inside the tank. Along with the performance equation (I 27), the design of the CSTR can be accomplished by realizing:

$$\tau = V / V_0 \qquad \text{(I 28)}$$

In a chemical process the reactor may not always be limiting operation and thus the volume of the reactor can be sized accordingly. V_0 is the flow rate of the product in m^3/s.

Fig. I 4.2 Here is the actual design of the CSTR system used for the production of ZIF-8 for this study. It consists of two mixing tanks each equipped with a peristaltic pump which had to be calibrated for flow rates. The Armfield CSTR itself is approximately 1 liter in volume and is fitted with a probe for measuring conductivity and/or pH. In addition it is possible to add various control schemes to the operation[71]. For this process the spray dryer throughput was the limiting step; 1 liter of liquid per hour.

Critical to the analysis of chemical reactors is the calculation of 2 different dimensionless numbers which characterize the process. The **Dahmkohler** number relates the reaction time scale to the rate of mass transfer via convection.

$$\mathrm{Da} = \frac{\text{reaction rate}}{\text{convective mass transport rate}} \tag{I 29}$$

For Da >> 1, the reaction rate is much greater than diffusion and reaches equilibrium very quickly compared to species migration. When Da << 1, diffusion comes to equilibrium before the chemical reaction. Equally important is the **Peclet** number which relates advective to dispersive transport; the mixing characteristics of real reactors.

$$\mathrm{Pe} = \frac{\text{advective transport rate}}{\text{diffusive transport rate}} \tag{I 30}$$

When the kinetics of the reaction are known **Da** and **Pe** can be calculated. There are two forms of the Peclet number. For thermal transport:

$$\mathbf{Pe} = \mathbf{Re\ Pr} \qquad \text{(I 31)}$$

Where **Re** is the Reynolds number and **Pr** the Prandtl number.

For mass transfer:

$$\mathbf{Pe} = \mathbf{Re\ Sc} \qquad \text{(I 32)}$$

Where **Sc** is the Schmidt number.

The Reynolds number is defined as:

$$\mathbf{Re} = \frac{\rho\, v\, D}{\mu} \qquad \text{(I 33)}$$

The Prandtl number is defined as:

$$\mathbf{Pr} = \frac{C_p\, \mu}{k} \qquad \text{(I 34)}$$

The Schmidt number is defined as:

$$\mathbf{Sc} = \frac{\mu}{\rho\, D} \qquad \text{(I 35)}$$

Where:

ρ is the density in kg/m^3

D is the characteristic diameter in m

C_p is the specific heat in J / kg ˚C

μ is the kinematic viscosity in m^2 / s

k is the thermal conductivity in

5. Data Analysis

The collection and analysis of data both qualitative and quantitative is at the heart of all experimentation. There is a huge and ever increasing cadre of so-called researchers poorly trained in the proper use of *statistical methods* for data analysis. This is not opinion. Scrutiny of the 'peer-reviewed' journals confirms that assertion. Couple that with *confirmation bias,* the desire to 'force' the experimental results to confirm your scientific hypothesis: one wonders how much grant money has been wasted and how much scientific progress has been thwarted.

Regression analysis describes a family of statistical techniques that attempts to provide relationships between independent and dependent variables so inferences about the future might be obtained. The specific algorithm employed depends on the amount, type, and condition of the experimental data and the manner in which it was collected. A thoughtful researcher realizes these subtleties and carefully chooses the optimum technique and metric. Systematic and random errors are accounted for and the propagation of these within any experiment and calculation is noted. Judicious selection of the proper technique does much to diminish the effects of confirmation bias. It is rarely admitted. Tatarko[53] in a series of papers was surprised to learn that a common measure of heat transfer, the **Nusselt** number **Nu**, provided confounding results and provided little insight into the effectiveness of nanoparticles as agents of enhanced energy transfer (**Fig. I 5.1**). The **Peclet** number **Pe**, which is the product of the Reynolds number and Nusselt number, was more informatrive (**Fig. I 5.2**). This fact was only exposed by submitting the heat transfer data to an augmented form of analysis known as *best subsets regression*.

Let's look at the tools the data analyst has at hand. What might be called *exploratory data analysis* (EDA).

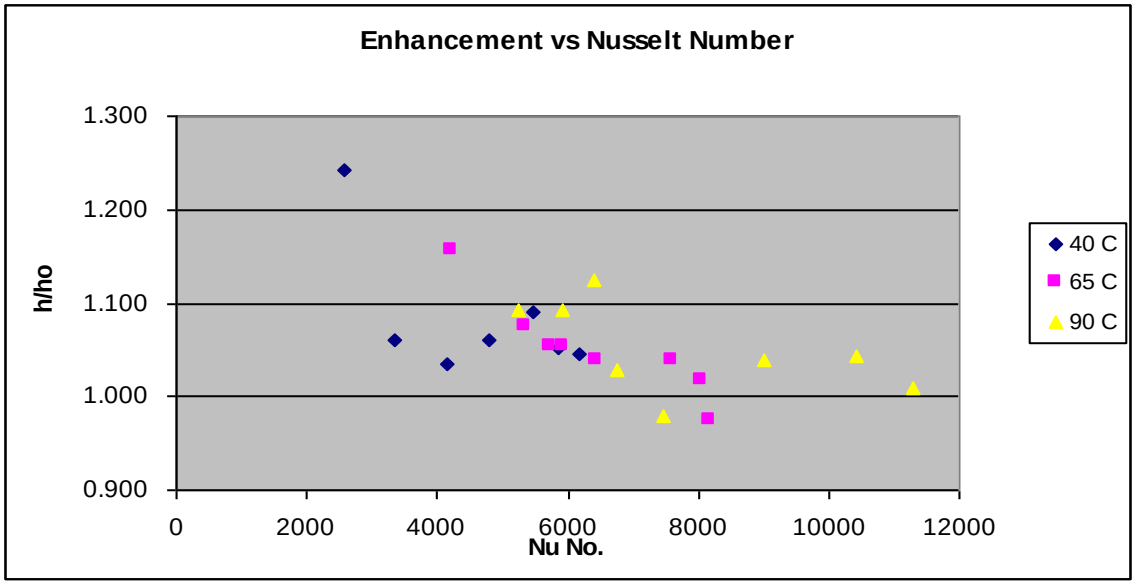

Fig. I 5.1 In a study by Tatarko conducted in 2011, the effectiveness of copper nanoparticles 60 nm in diameter, infused into a base oil of Amsoil 0W-30 was investigated. The measure of effectiveness was the increase in **h**, the heat transfer coefficient over the base oil $\mathbf{h_0}$. The Nusselt number is a recognized predictor of heat transfer behavior yet this plot offers little insight into any trends. In fact in 2 instances the heat transfer coefficient got worse (< 1.000) as **Nu** increased.

Cheap computing power has made the management of huge data sets tractable and there exists the so-called *trinity of selection*[72].

1. **Statistical tests**: chi-square, t-tests, significance, F, … etc.
2. **Criteria**: R-squared, adjusted R-squared, Mallows' C_p, MSE… etc.
3. **Stopping Rules**: p-value flags.

In addition the statistician must decide how to deal with outliers, gaps, and clumps. The correct regression algorithm is one that permits all of the data to be represented without

bias. The choice of variable selection is not always easy. In experiments that comprise this dissertation there exist a multitude of variables effecting the flow of energy from the nanoparticles to and from the base oil and to and from the tube wall (cf. **Part 1**).

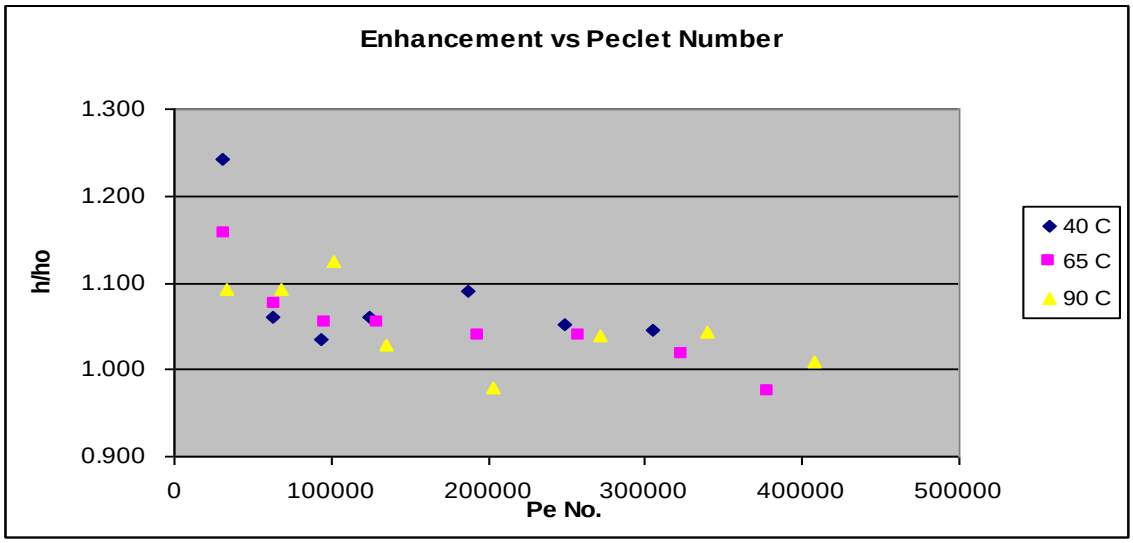

Fig. I 5.2 Under the same conditions as in **Fig. 5.1**, calculation of **Pe** provided a clearer picture of the heat transfer enhancement. The Peclet number is the product of the Reynolds number and the Prandtl number: **Pe** = **Re** * **Pr**. Thus the enhancement results in a combination of effects created by the fluid flow (**Re**) and the thermal properties (**Pr**) of the base fluid and the nanoparticle. The decision to investigate other predictors of heat transfer behavior was guided by insights gained through the use of *best subsets regression* of the huge data set.

The *best subsets regression* algorithm helps the statistician choose the model that best represents the data based on statistical criteria. Each, some, or all of the independent variables and any combination or multiple of them can be submitted for analysis. It is at this point that engineering expertise must prevail. The analyst must submit as detailed a collection of independent variables as necessary to describe the process, yet, the model must not be too complicated. The best subsets regression technique while powerful must be used by the discriminating scientist or engineer. In the hands of the novice it might

lead to dangerous conclusions. The dimensionless numbers (**Re**, **Pr**, **Pe**, …etc.), so common to engineering analysis are particularly suited for inclusion into best subsets regression data sets because these are groupings of the independent variables and are on the order of one.

The *self-organizing feature map* (SOFM), or *Kohonen map* provides another powerful non-statistical technique for organizing and analyzing data. This technique takes elements of topology, linear algebra, and probability to provide a non-linear ordering of experimental measurements. A multidimensional (say *p*), data set of variable measurements is converted to a 2-dimensional set of results.

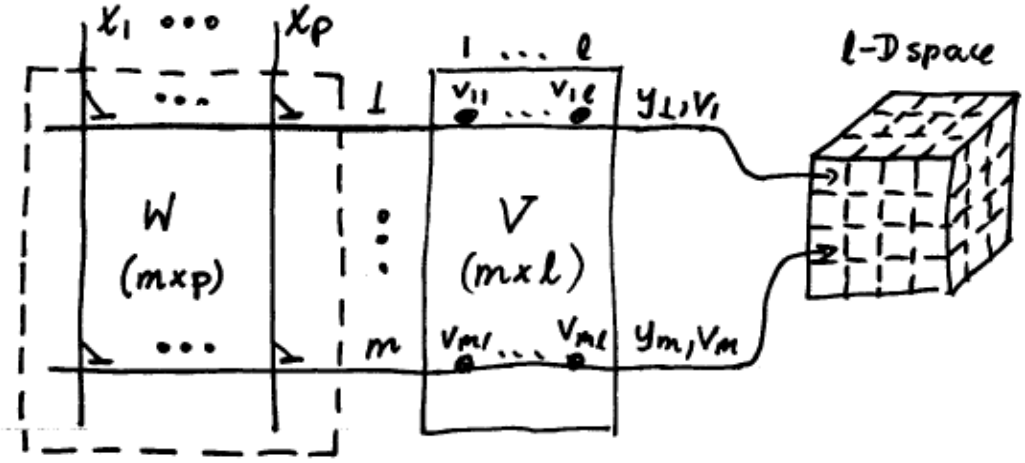

Fig. I 5.3 This is a basic schematic[73] of the process that generates the Kohonen (SOFM) map. The **input space** has a dimension of ***p*** while the **output space** has a dimension of ***l***, usually 2 or 3. The output space is known as a **neuronal space** and the **spatial location** of each neuron in the **topographic map** corresponds to a particular domain or feature of the input[73]. It is the *competition* and *cooperation* between neurons that capture the behavior of the input. The **V** matrix provides the original position of the ***m*** neurons.

The map formation requires a *learning algorithm* that includes *competition* and *cooperation* between neurons. During **competition,** each input vector $\mathbf{x_{(n)}}$ is compared to

a weight vector from **W** the weight matrix and its relation to the position of a neuron in $\mathbf{V}(k_{(n)})$. The 'winning' neuron is based on the minimum distance:

$$\mathbf{x}^T(n) - \mathbf{W}(k(n), :) \qquad \text{(I 36)}$$

During the **cooperation** phase, each neuron within the 'neighborhood' (a distance $\rho(j)$) of the 'winning' neuron has its 'strength' $\Lambda(j)$ updated by a Gaussian function.

$$\Lambda(j) = \exp(\rho^2(j) / 2*\sigma^2) \qquad \text{(I 37)}$$

where σ^2 is the spread of the Gaussian function. So the SOFM algorithm consists of:

1. Compile a weight matrix **W** with a random set of *m* input vectors.
2. Determine the 'spread' σ^2 of the 'neighborhood' function (Gaussian)
3. For every input vector $\mathbf{x}_{(n)}$ determine the 'winning' neuron k(n) and its position V(k)
4. Calculate the 'neighborhood' function and modify the weights of all neurons proportional to the 'neighborhood' function and the distance of each respective weight vector in relation to the input vector.
5. Continue until 'distances' = 0 and all neurons have been ordered.

In a previous study, Tatarko[53] submitted a large data set of experimental heat transfer data for best subsets regression to determine the optimum model of heat transfer enhancement. Subsequently the results were also submitted for Kohonen mapping (SOFM) with the following results (**Fig. I 5.4**).

The results from all analytical tests, but **especially those generated automatically via canned software** must be viewed with skepticism and engineering savvy. The Kohonen maps provide an insightful transformation of multidimensional data into 2 dimensions;

that which we can visualize and understand. For this particular set of data both the *best subsets regression* and the *SOFM* corroborate the uselessness of the Nusselt number when analyzing the heat transfer enhancement of nanofluids. Surprisingly the % wt. fraction results are not conclusive either. Does it mean that this variable is unimportant? Hardly! It is just that this data set does not reveal information on this variable. Perhaps another analytical technique would glean more information. The thoughtful and diligent researcher appreciates that.

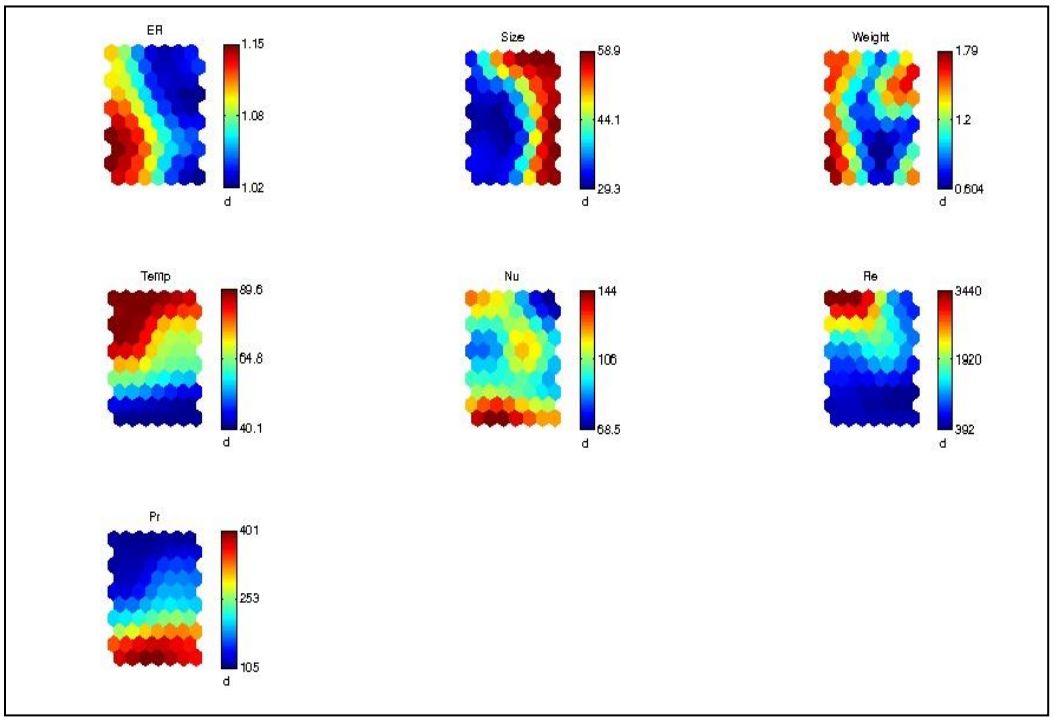

Fig. I 5.4 The results of submitting a huge data set of experimental heat transfer data for Kohonen mapping subsequent to best subsets regression analysis. The *enhancement ratio* ER, is a comparison of the heat transfer coefficient of the nanoparticle-enhanced fluid to the base oil. It is to be maximized at 1.15. The 7 maps correspond topologically on a one-to-one basis. Thus the particle size should be kept small: 29.3nm. The Reynolds number and temperature should be kept low. The Prandtl number and thus the Peclet number should be kept in the medium to low range. The mappings for the wt% and Nusselt number are

more problematical. There are 'hot' spots roaming throughout the map. There is no definitive classification and this must be observed by the discriminating researcher. Compare the mathematical approach to data analysis afforded by the SOFM versus the intuitive effort compiled in **Table 1**.

Systematic and random errors encountered during data collection along with the effects of propagation must be accounted for by the conscientious analyst. Systematic errors include those involved in the operation of laboratory test equipment. Most instruments have a standard of known value against which calibration can be made. It is part of the researcher's task to instruct technicians in the proper methods and intervals. It should be noted that a particular piece of equipment in the Heat Transfer Laboratories at the University of Louisville has been a massive source of systematic error. This problem is addressed in **Part III** of this dissertation. Random errors can never be eliminated yet the effects and propagation of these effects throughout the calculation of results must be addressed. The propagation of measurement errors of items such as temperature, fluid velocity, and density may render any experimental results and conclusions meaningless.

The determination of property values for ZIF-8 is crucial in determining its effectiveness as an agent of heat transfer enhancement. In order to assure a confidence level of 95% it was calculated that at least 25 different measurements of properties such as density, specific heat, and BET were to be made. Graphs of results are to include the appropriate error bars and any other values are to be reported with the appropriate statistics. Before reporting values for any chemical or physical properties to a peer-reviewed journal, samples should be submitted to another independent testing agency for corroboration. For this dissertation the error bars consisted of the **standard error** (std. err.)**.** std. err. = std. dev. / √ sample size

It is tempting to assume that all measurements and associated errors are normally distributed. This should be demonstrated.

This researcher is passionate about education and has assumed the role of mentor to 2 interns. Instruction in the proper calibration, use, and maintenance of laboratory equipment along with the use of personal protection items comprises an important part of the education of an engineer and scientist. This is the necessary first step in the collection and analysis of meaningful data.

II

LITERATURE REVIEW

1. Heat Transfer Enhancement via Nanoparticles

One of the major goals of the National Nanotechnology Initiative (NNI) strategic plan in 2007 was advancement of a world-class nanotechnology research and development program. In this plan, fundamental nanoscale phenomena and processes were to be among the most important research areas spanning multiple disciplines with applications in solar energy, heating, ventilation, and air conditioning (HVAC), and renewable resources.

The term "nanofluids" was coined by researchers at Argonne National Laboratory and refers to a two-phase mixture composed of a continuous liquid phase and dispersed nanoparticles in suspension[2]. The nanoparticles added are typically on the order of 100 nm or less at volume fractions less than 5%. Even at these low volume fractions, significant thermal conductivity enhancements have been reported based on the nanomaterials and base fluids used.[2-7] Since the first report of nanofluids, there have been hundreds of articles written on the subject of nanofluids. One early study by Choi and colleagues [8] which utilized CNTs of 25nm in diameter and 50μm in length dispersed in a poly (α-olefin) (PAO) oil found that the thermal conductivity was enhanced by 160% over the base fluid at a volume fraction of only 1%. A more recent study by Chen and

Xie [79]. observed a 10% to 28% enhancement in thermal conductivity of silicon oil-based multi-walled carbon nanotubes (MWNT) nanofluid.

Practically, the heat transfer coefficient of a nanofluid is more important than the thermal conductivity since this determines how effectively the heat can be transferred within a system. Different particle sizes, shapes, aspect ratios, and volume fraction have been studied by research groups around the world[10-13]. Commonly used base fluids include water and ethylene glycol (EG). Jwo et al.[80] applied Al_2O_3/water nanofluid to a multi-channel heat exchanger system. The overall heat transfer coefficient was enhanced by a maximum of 19% at 1.0 wt %. Xie et al [13] observed a significant increase of heat transfer coefficient of up to 152% using MgO nanoparticles dispersed in a mixture of distilled water and ethylene glycol over a Reynolds number range of 300 to 1500.

There are limited results for heat transfer enhancement using oils either in laminar or turbulent flow reported in literature. Chun et al.[81] determined that heat transfer coefficients increased as particle loading increased from 0 to 0.5 vol% for Al_2O_3/transformer oil nanofluids. It was also found that over a Reynolds number (Re) range of 100 to 450, larger nanoparticle sizes (43nm) showed a slightly larger enhancement in heat transfer coefficients when compared to smaller nanoparticle sizes (27-43nm). A more interesting result showed that rod-like alumina (7 nm diameter with an aspect ratio of 50 to 200) displayed higher heat transfer coefficients at lower Re but lower heat transfer coefficients at higher Re when compared to the larger nanoparticles over the Re range of 100 to 450. The researchers postulate that this may be due to alignment of the rods at the thermal boundary layer in the pipe at lower Re. Choi and colleagues [11] used spherical and rod-shaped Al_2O_3 and AlN dispersed in transformer oil

to make nanofluids. All three types of nanofluids showed small enhancement of heat transfer coefficient at a Reynolds number range of 100 to 500. A maximum of 20% increase was observed for AIN/transformer oil based nanoparticles at a volume fraction of 0.5%. Yang et al.[82] found that a graphite nanoparticle loading of 2 vol%, in a mixture of two synthetic oil based nanofluid showed little enhancement of the heat transfer coefficient. However at a particle loading of 2.5 vol%, there was a 22% increase in the heat transfer coefficient at a temperature of 50°C at low Reynolds. As the temperature increased to 70°C, the enhancement of heat transfer coefficient decreased slightly to 15%.

To date, most of the work done in the field of heat transfer enhancement via nanoparticle addition involved the use of metals or metal oxides with high conductivities. These nanoparticles did have rather small total surface areas. The ZIF-8 molecule has a low conductivity but extremely large surface area: approximately 1000 m^2 / g. If there is to be enhanced heat transfer with this nanoparticle some insight into possible mechanisms might be forthcoming.

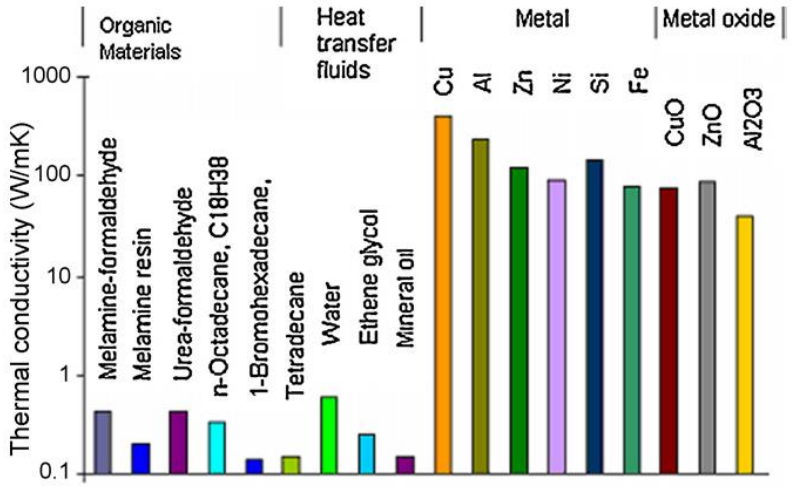

Fig. II 1.1 A comparison of the conductivities of various compounds/elements[83].

Saidur *et al* [84] discussed some of the challenges of potential commercial applications of nanofluids while expounding rapturously about the benefits and long-term outlook. The challenges revolved around colloid stability, increased pumping requirements, and the cost of production. It should be noted that the discussion of economics in this paper is rare and welcome. If

$$Q = h\ A\ \Delta T \qquad \text{(II 1)}$$

There are three items we can change to effect increased heat transfer; Q.

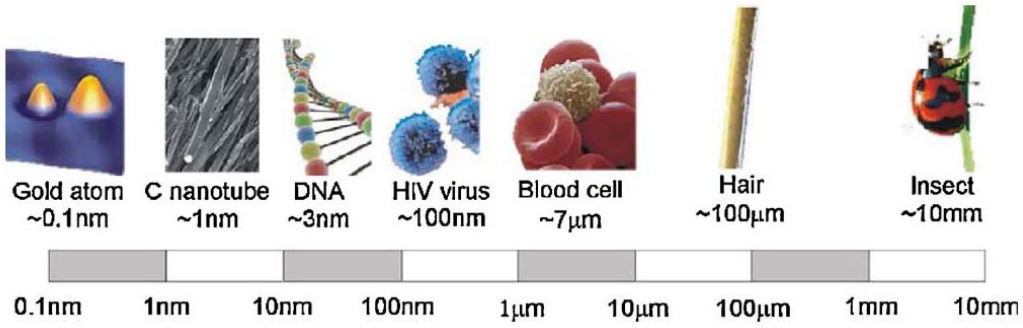

Fig. II 1.2 A cartoon depicting the comparative size scale of various items. Most people have little understanding of these relationships and that is part of the inertia behind the lack of commercial application of nanoparticles in HVAC systems[84].

The area (A) may be increased, the temperature difference (ΔT) increased, or the heat transfer coefficient (h) increased. Microelectronic applications are size-restricted and some materials are heat-sensitive so the alternative is an amplification of the heat transfer coefficient. This is the goal of nanoparticle addition to fluids. **Fig. II 1.3** is a depiction of the various current applications. Most of us as consumers would not recognize many of these.

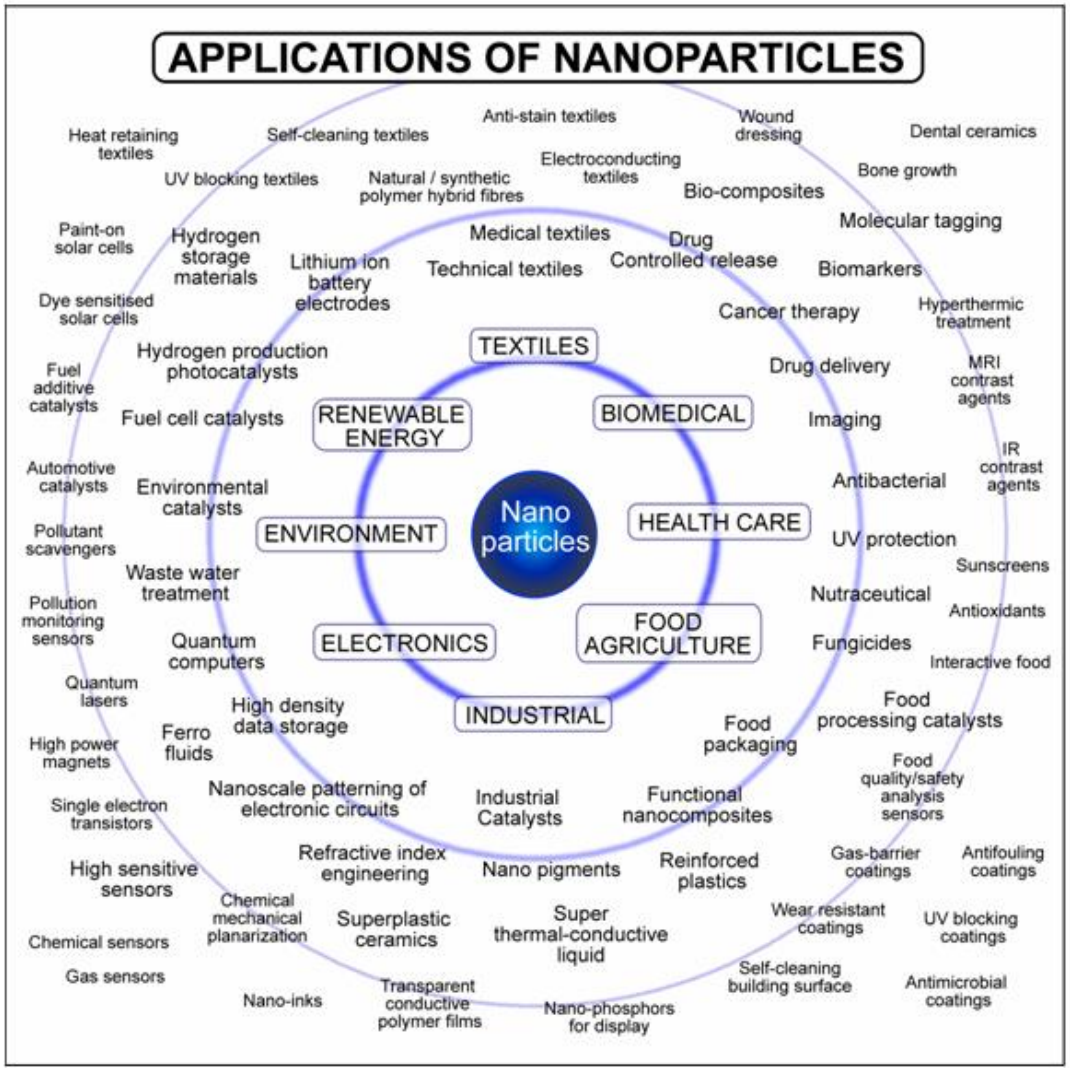

Fig. II 1.3 Current and hoped-for applications of nanoparticles. Few of these are consumer-identifiable and most have limited use. It will be in this generation that huge breakthroughs come into vogue[85]

Interestingly, this paper mentions the effect of surfactants as perhaps an unrecognized key to the enhancement mechanism. The optimum amount of 'stabilizer' (Saidur's term for surfactant), reduces nanofluid viscosity and permits minimum agglomeration. This could be an area for more research. As a testament to this research, Saidur emphasizes the

enormous disparity in the results obtained by different researchers, the lack of a coherent theoretical mechanism, and the unpredictability of long-term nanofluid stability. Mentioned are glowing reports in the fields of HVAC, solar energy, machining, transportation, and medicine. Not surprisingly, few of these involve commercial applications. This review article purports that the nanoparticle business is currently approaching $1 billion per year.

Pang[86] *et al*, authored a review paper on thermal conductivity, the most studied property, of nanofluids. Included is an exposition of various mathematical models for calculating the effective thermal conductivity along with theoretical mechanisms that may explain the behavior of nanoparticles infused into a base fluid. It is claimed that among the most controversial topics concerning nanofluids are theories surrounding aggregation due to Brownian motion, formative nano-convection, and the molecular nanolayer.

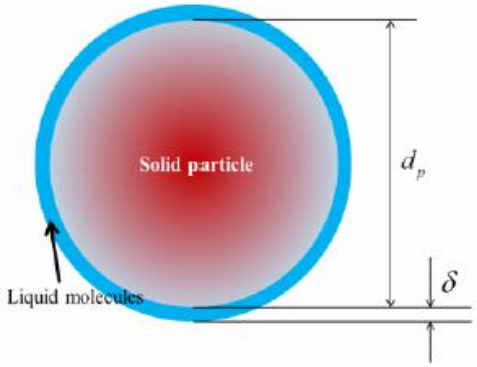

Fig. II 1.4 The molecular nanolayer, theorized by Yu and Choi, is used to explain the enhanced thermal conductivity afforded by the nanoparticle. *Effective medium theory* did not accurately predict this effect for particles < 1μm. Thermal diffusion takes place in the layer δ. This is not to be confused with the Kapitza resistance layer which is prevalent among agglomeration of nanoparticles. There has been no experiment yet to determine the thickness of δ[86].

The development of the molecular nanolayer is just one part of the thermal conductivity model. It is followed by the *layering mechanism* which helps to explain bulk thermal disffusion.

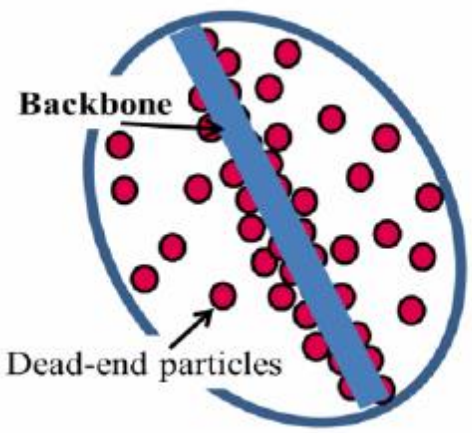

Fig. II 1.5 The layering effect of nanoparticles. It is speculated that thermal conductivity is enhanced due to increased ordering along the backbone. This composite theory by Yu and Choi is plausible only when Brownian motion plays an integral part. It has been shown that thermal diffusion via bulk motion is orders of magnitude greater than that afforded by Brownian motion[86].

The authors posit two forms of Brownian motion within the nanofluid: collisions between the nanoparticles which can cause agglomeration, and *nano-convection.* There exists an optimum level of agglomeration that enhances thermal conductivity. The actual sizes and shapes of the nanoparticles greatly influence the level of agglomeration. Whenever experiment did not coincide with the theory the authors stooped to blaming the Kapitza resistance. This is dubious science yet the authors claim some success with larger nanoparticles. Pang includes a collection of correlations for calculating the effective value of themal conductivity.

The long term stability of nanofluids is addressed in a paper composed by Nine *et al*[87]. His premise: the lack of commercial applications of nanofluids is attributed to the almost certain degradation and destabilization of nanoparticles in the base fluid. In a series of experiments, metallic nanoparticles were shown to have been oxidized and agglomerated with loss of thermal conductivity. Repeated cycling between hot and cold temperatures accelerated this degradation. More importantly once the nanofluid has been subjected to a boiling cycle, amounts of nanoparticles were shown to have been deposited (fouling) on heat transfer surfaces[87].

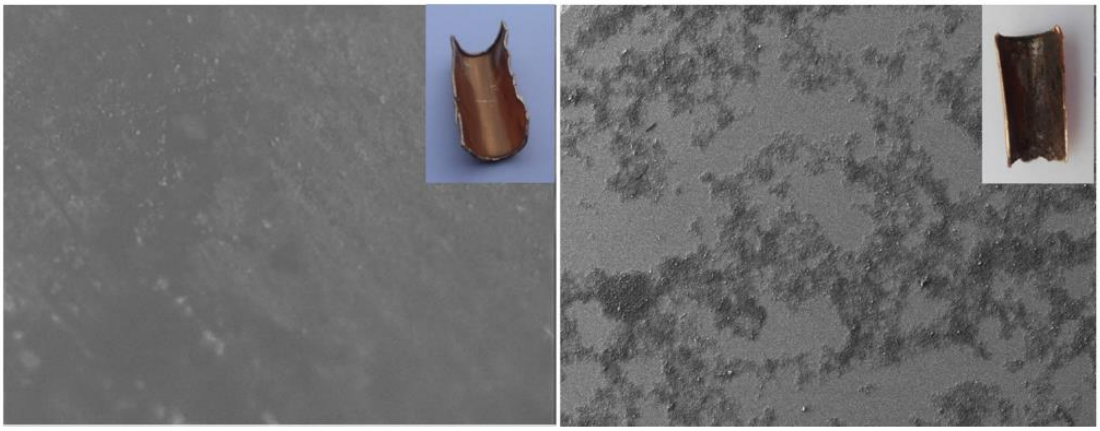

Fig. II 1.6 Fouling and corrosion of heat exchangers is a massive expense in the process industries. Nine[87] is the first author to report the deposition of nanoparticles on heat transfer surfaces after a cycling period. Surface tension and roughness play roles in the process. Changes in these surfaces affect the heat transfer coefficient. These photos were taken after only 2 weeks of cycling. The heat transfer rig at the University of Louisville may have already been fouled due to years of use.

Since the volume fraction of nanoparticles within the base is so small any fluid destabilization or deposit of material on heat transfer surfaces may render the thermal enhancement negligible.

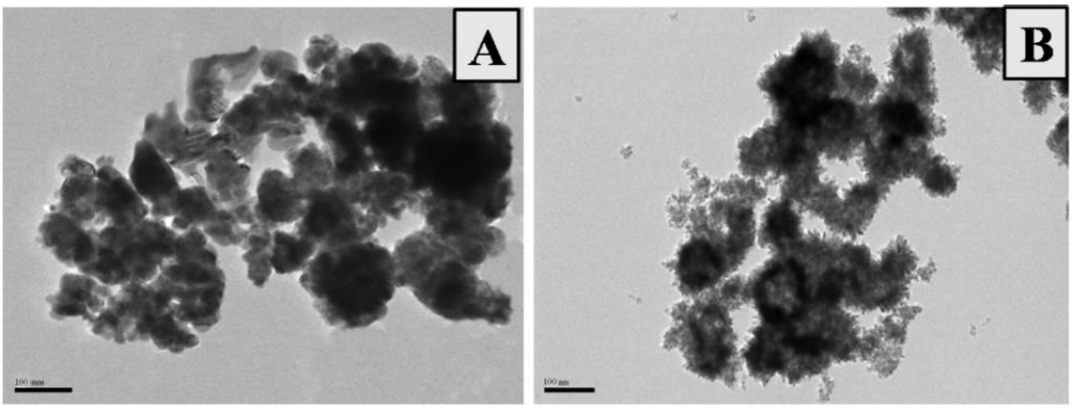

Fig. II 1.7 Increased agglomeration [A] of Cu nanoparticles after 24 hours of cycling[87].This was expected. What was not expected was an actual decrease in the size along with a change of shape of the nanoparticles themselves [B]. Fluid stability and the thermal enhancement is nullified.

This paper offers experimental evidence depicting the rapid degradation of a nanoparticle infused base oil. Fouling of heat transfer surfaces along with morphological changes of the nanoparticle portray as more sources of systematic error. How many experiments were done and papers written without consideration of this phenomena?

Zerradi and his co-authors presented a paper purporting a new correlation for calculateing the Nusselt number of various nanofluids and subsequently the thermal conductivity[88]. **Table 2** on the next page is a compilation of previously popular incarnations. Although Tatarko[53] has shown that the Nusselt number is not an accurate predictor of heat transfer behavior within the nanofluid, these correlations could become welcome additions in the search for accurate values of conductivity, **k**. The general form of **Nu**:

$$Nu = f\left(\mathrm{Re}, \mathrm{Pr}, \frac{k_p}{k_f}, \frac{(\rho c_p)_p}{(\rho c_p)_f}, \phi, \text{dimensions and shape of particles}\right) \quad \text{(II 2)}$$

Where the subscripts f and p refer to the base fluid and nanoparticle respectively. The density is denoted by ρ and the volume fraction θ.

Table 2[88] Popular correlations for the Nusselt number

References	Nusselt number	
Acrivos and Taylor [23]	$Nu = 2 + 0.5RePr$	(2)
Whitaker [25]	$Nu = (2 + 0.4Re^{1/2} + 0.06Re^{2/3})Pr^{0,4}(\mu_b/\mu_o)^{1/4}$	(3)
White [27]	$Nu = 2 + 0.3Re^{0,6}\,Pr^{1/3}$	(4)
Gnielinski [28]	$Nu = 0.012(Re^{0.87} - 280)Pr^{0.4}$	(5)

The authors proposed to use the elegant and simple Gnielinski correlation as a foundation. Instead of using the standard Reynolds number, the authors used the *Brownian motion Reynolds number* based on kinetic theory and convective flow in the Stokes region.

$$\mathrm{Re}_m = \frac{1}{v}\sqrt{\frac{18k_bT}{\pi\rho d}}, \quad \text{(II 3)}$$

The kinematic viscosity is ν, and Boltzmann's constant is k_b. The temperature is T and ρ and d refer to the density of the base fluid and the particle diameter. Thus the functional relationship becomes:

$$Nu = f(\mathrm{Re}_m,\ \mathrm{Pr},\ \phi) \quad \text{(II 4)}$$

This results from the authors' claims that the Nusselt number is a function of the nanoparticle alone[88]. It is posited that via Monte Carlo simulation and experiment the new correlation predicts the Nusselt number and thermal conductivity within about 4%.

Two points need to be made. In a previous paper, Tatarko[53] proposed the use of dimensionless numbers based solely on the nanoparticle. From personal experience, 4% accuracy is about all one can expect from molecular simulation studies. This may not qualify as *technical accuracy* since it only justifies 2 significant figures.

$$Nu = \alpha' Pr^p (\mathrm{Re}_m^q + \beta')(\phi + \chi') = Pr^p (\alpha\phi + \beta \mathrm{Re}_m^q + \chi\phi \mathrm{Re}_m^q + \delta) \quad \text{(II 5)}$$

Notice the terms α, β, χ, and δ. These are coefficients rendered when experimental data is 'fit' to the equation; a common numerical technique. This is the authors' equation-of-choice for the correlation[88].

As important as the measurement of transport properties of the nanofluid so too is the method of preparation. This is the premise of a paper submitted by Haddad *et al*[89]. Metallic and non-metallic nanoparticles seem to require different treatment when attempting to infuse these into a base fluid. Two opposed processes dominate here; *agglomeration* and *sedimentation.* Nanofluids are thermodynamically unstable due to the high surface energies of the particles themselves. In an attempt to minimize this energy, particles motivated by Van der Waals forces tend to agglomerate and maximize the surface area. Gravity forces sedimentation. One of the premises underpinning the definition of nanofluid is that no chemical reaction occurs between the base fluid and the

particle. The authors present a review of the preparation techniques for 11 different nanofluids and compile a lengthy table of the results. What is best gleaned from this tome is the dependence of nanofluid stability on the *zeta potential.* The zeta potential ξ, is the voltage difference between the base fluid and a thin layer of fluid surrounding the nanoparticle (cf **Fig. II 1.8**)

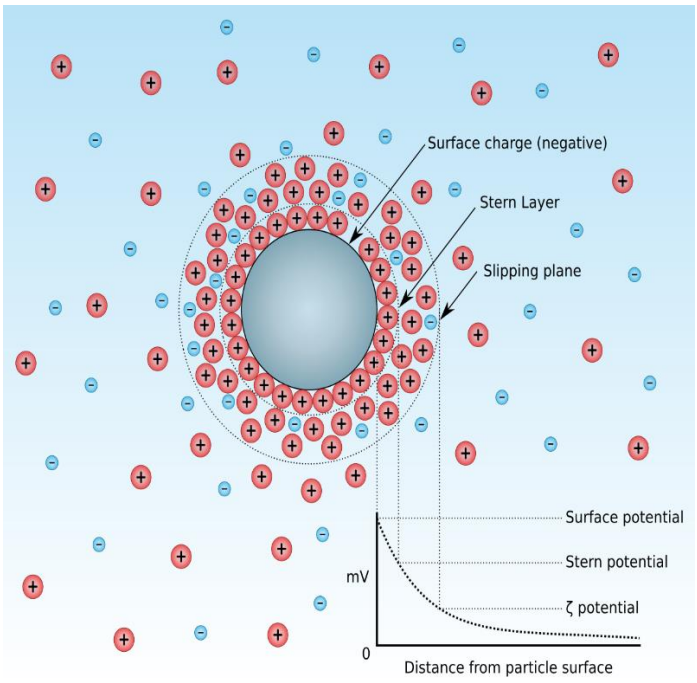

Fig. II 1.8 A diagram showing the parameters that comprise the *zeta potential*, a key indicator of colloid (nanofluid) stability[90]. At the *isoelectric point*, the solution has no net charge. Thermodynamically, charged surfaces tend to form double layers and changing the pH of a nanofluid can alter the isoelectric point and thus the stability.

Colloidal solutions (nanofluids) with the zeta potential < 5 mv agglomerate immediately. Values above 30 mv are stable while those greater than 60 mv render enhanced stability[89]. In summary it is a challenge to effect homogeneity at the optimum level of aggregation without altering the thermal or transport properties of a nanofluid. Often a combination of techniques is necessary to accomplish long term success. *Sonication*, the

use of sound waves for mixing, *along with pH control*, and the use of *surfactants* round out the three accepted methods[89]. The future commercial successes of nanotechnology revolve around the ability to keep the particles in solution while inhibiting sedimentation and agglomeration.

P.D. Shima and John Philip[91] espoused the use of the *effective mean theory* (EMT) originated by J.C. Maxwell in 1881 for calculating *k* the thermal conductivity of a nanofluid.

$$\frac{k}{k_f} = \frac{1 + 2\beta\phi}{1 - \beta\phi} \qquad \text{(II 6)}$$

Where *k* is the conductivity of the nanofluid, k_f the base fluid, θ, the volume fraction of the nanoparticle and $\beta = (k_p - k_f) / (k_p - 2\,k_f)$.

Ali, El-Leathy, and Al-Sofyany experimented with an Al_2O_3 / water nanofluid in the radiator of an automobile[92]. Similar to results obtained by scores of researchers including Tatarko, heat transfer enhancement ~ 14% occurs at an optimum volume fraction of 1% and decreases dramatically at higher concentrations. The goal here is the miniaturization of the automobile cooling system because of the increased heat transfer and thus a reduction in weight. This was strictly a laboratory demonstration and made no mention of the fouling of system components or the degradation of the nanofluid over time.

Hussein, *et al*[93] conducted laboratory experiments and molecular simulations in the laminar and turbulent flow regions with the standard Al_2O_3 and water-glycol system. The

usual results were obtained however what is notable is the suggestion that perhaps circular tubes do not offer the most surface area and best platform for heat transfer enhancement via nanofluid technology. More testing and analysis was to follow.

In a beautifully designed apparatus Anoop, Cox, and Sadr[93] examined the efficacy of a SiO_2-water nanofluid in heat exchangers (**Fig. II 1.9**). With much hope the researchers found that the heat transfer enhancement afforded by the nanofluids ~ 5% was nullified by the increase in pressure drop, degrada 57 thermal properties and the fouling of heat transfer surfaces within the heat exchangers. At this time it appears that the use of nanofluids within heat exchangers will be limited.

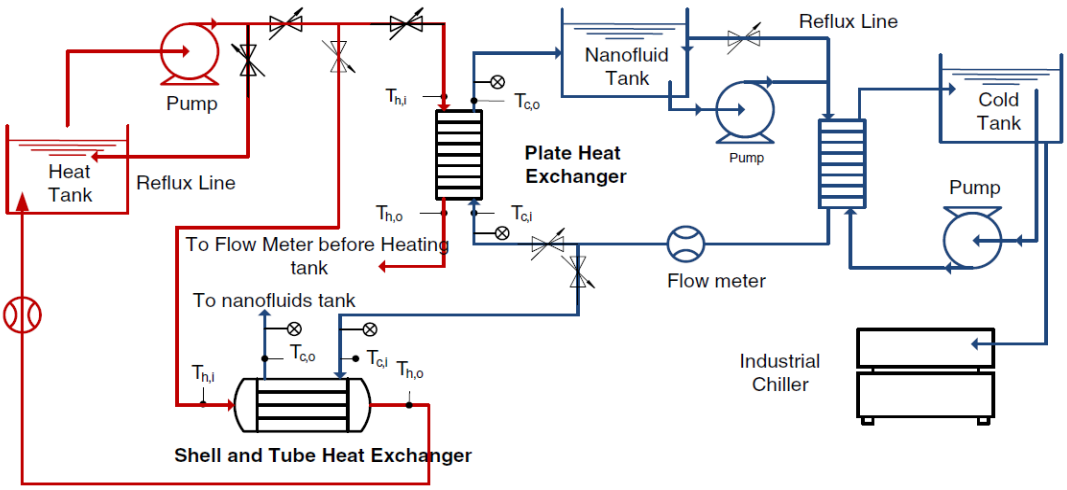

Fig. II 1.9 A heat exchanger train designed and built by Anoop *et al*[93]. Although no samples were removed from the system to determine the extent of fouling or nanofluid degradation the authors verified the increase in pressure drop throughout the test rig. The meager heat transfer enhancement of 5% could not justify the increased pumping costs. It appears that the addition of surfactant necessary for sustained suspension of the nanaoparticles in fact alters some of the thermal properties.

Referencing **Fig. II 1.4**, It is theorized by Xuan, Li, and Tie[95], that the addition of surfactants greater than 0.1 wt% affects the thermal boundary layer so aversely that heat transfer enhancement is negligible. This provides a plausible explanantion for the wide disparity in results obtained by many researchers over the last 20 years. Increased attention to the roles of surfactants and pH is warranted.

As important as thermal conductivity is so is *specific heat* C_p . In a comprehensive review paper Sharul *et al*[96], presented results of more than fifty researchers on the specific heats of various nanoparticle/base-fluid couples. What is particularly noteworthy is the lack of agreement between experimental values and those obtained from accepted correlations. The best results were obtained by generating an equation through a 'fit' to the experimental data. Even so, there is an average error in the results of about 2 %[96]. This is disconcerting for now we have errors beginning to mount-up. The error in thermal conductivity is also between 2 % and 5 % [91]. There is the concern with the addition of surfactants to the base fluid necessary for a stable nanofluid, and the increased (yet unmeasured) thermal resistance generated during fouling. Compounding the problem is unknown systematic error associated with laboratory equipment along with natural variation. A back-of-the-envelope calculation indicates that experimental heat transfer enhancement less than 7 % is probably meaningless. Improved methods of analysis of the important thermal, caloric, and transport ptoperties of these nanofluids is warranted.

An accepatble correlation for the specific heat of the nanofluid[96]:

$$(C_p)_{nf} = [(1-\phi)(\rho C_p)_f + \phi(\rho C_p)_n]/[\phi\rho_n + (1-\phi)\rho_f] \qquad \text{(II 7)}$$

Where φ is the volume fraction of the nanoparticle and the subscripts *f* and *n* refer to the base fluid and nanoparticle respectively. The density is ρ. The article in conclusion claims that specific heat varies with temperature, particle size and shape, and volume fraction. This is the standard (monotonous) claim of all of the previously cited scripts.

In an attempt to theoretically account for particles size in the model and correlation for thermal conductivity, a group of researchers in Singapore[97] developed a beautifully conceived extended model of Maxwell's classical treatise on conductivity.

Much has been made-of the conductive and convective properties of the nanoparticle-enfused base oil and this has been exhaustedly analyzed *ad nauseum*. Said *et al*[98] investigated the radiative properties of nanofluids with an eye to enhancing heat transfer within solar energy applications. This was accomplished via study of the optical properties of the nanofluids through electromamgentic wave analysis. The absorption properties of nanofluids within the visisble spectrum (sunlight) is dependent on size, shape and concentration. More precisely, these researchers found that for solar energy applications the concentration (volume fraction) had to be closely controlled. High concentrations (> 1%) resulted in the creation of a boundary layer at the nanofluid-solar panel interface: think Kapitza resistance. Radiation and thus thermal absorption was great but much was immediately lost to the surroundings with little transfered to the nanofluid within the solar panel. Volume fractions at the low end did not adequately capture available radiation[98]. Again we must remember that the composition of the nanofluid is dependent on the synthetic process, single-step or two step, and the negation of agglomeration. The two-step method involves the infusion of previously synthsized

nanoparticles into a suitable base oil along with copious amounts of dispersants. Stearic and Van der Waals forces are neutralized and the pH altered to enhance stability.

The current state-of-the-art in solar energy applications is the **direct absorption solar collecter** (DAC). Water a fluid with a notoriously low thermal conductivity has traditionally been used as the thermal transfer agent. Some researchers claim 5% to 10% improvement in heat transfer upon the addition of carbon nanotubes, graphite, or silver nanoparticles[98]. The goal of solar energy applications is the reduction of carbon dioxide and dependence on fossil fuels.

Interestingly, the radiative absorption properties of water within the solar collectors was increased nine times upon the addition of nanoparticles. This led to a heat transfer enhancement of aproximately 10%. This effect decreased dramatically after just a few heating-cooling cycles[98]. The researchers were certain that this difference was caused by a disintegration of nanofluid stability. Recall that it was previously mentioned in this work that fouling and nanoparticle metamorphosis was apparent in nanofluid systems after just a few cooling-heatng cycles[87]. Shear forces have a huge effect. The key to harnessing the radiative absorption properties of nanofluids is in the understanding of light scattering; Rayleigh and Mie theory. This dissertation is not an expose on the matter of light yet Said and his coauthors[98] make a compelling theoretical argument for pusuing radiative enhancement of thermal fluids with nanoparticles and present 2 figures that help us understand the effects. Controlled and efficient absorption of light, critical to solar energy applications, is intimately related to synthesis of an optically stable nanofluid composed of rock-sold nanoparticles and thermally efficient base fluids.

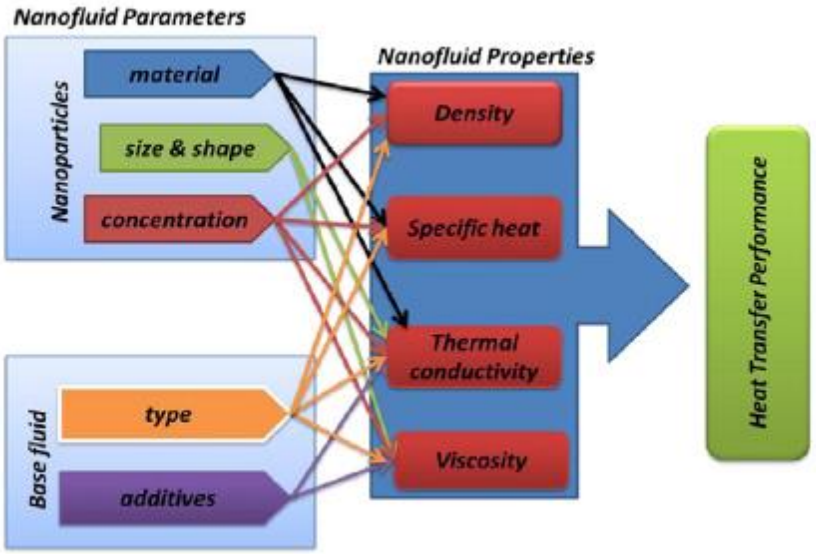

Fig. II 1.10 A summary of items[98] mentioned throughout this work that affect the heat transfer performance of nanofluids. Notice the cross-linking effects. Additives such as dispersants have a marked effect on viscosity and thermal conductivity. What is missing from this figure is the effect of pH which can also be adjusted with various compounds. A significant amount of work in this dissertation was devoted to the determination of the density, specific heat, and thermal conductivity of ZIF-8. To the best of my knowledge this work is the first to record these values.

Fig. II 1.10 and **Fig. II 1.11** depict the effects and significance of particle size and the absorption and scattering of light. The control of particle size and shape, (tunable properties) is part of the panache of nanoparticle technology. There are a number of synthetic tricks available to the thoughtful and diligent researcher which produce a desired particle geometry. A true triumph. What cannot be emphasized enough is the lack of nanofluid stability demonstrated and documented in paper after paper reviewed by this author of this dissertation. A cursory review of theses and dissertations prepared by my predecessors displays a lack of understanding of this phenomenon.

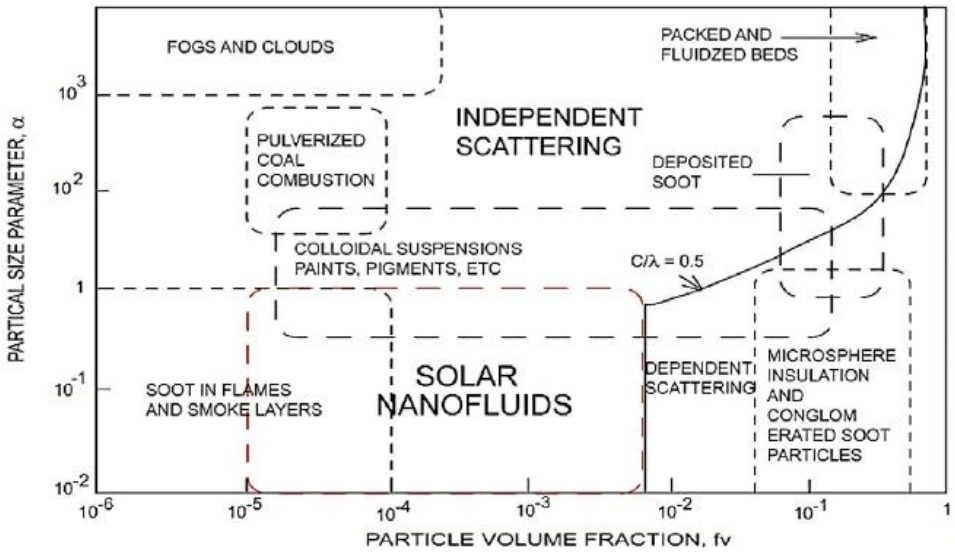

Fig. II 1.11 This schematic[98] presents a guide for the synthesis of nanoparticles suitable for use in a solar collector. The solar collector takes radiative energy from the sun and transfers it to a fluid, typically water. The addition of nanoparticles is said to enhance this heat transfer. The vertical axis, known as the *size parameter α*, is the ratio π*D / λ where D is the particle diameter and λ is the wavelength of light. Since the wavelength of visible light is about 10 times greater than the diameter of most nanoparticles (< 100 nm), Rayleigh light theory predominates[99]. Turning attention to the horizontal axis, the volume fraction, it can be seen that there exists a relatively small set of size/geometry/concentration combinations that will effect enhancement. Said and his co-authors[98] reviewed 122 papers that reveled in the ability to create tunable nanoparticles that satisfied these requirements and enhanced heat transfer in solar collectors by as much as 10%. Sadly in the conclusion, the researchers admitted that much of the purported results were short-lived due to nanofluid instability and in reality many of the results were irreproducible. Interestingly, most of the work in the reviewed papers was completed with carbon nanotubes and/or silver nanoparticles. The ZIF-8 nanoparticle is characterized by the preponderance of the imidazole linker over the zinc molecule (cf **Part I Fig. I 1.10**). It is more 'organic' than 'metallic'. What optical properties of this nanoparticle could be exploited?

Boqi, Xiao, Yi, and Lingxia[100] developed a novel method of determining thermal conductivity of nanoparticles using Brownian motion and fractals. The **fractal**

dimension of a nanoparticle can be used to help analyze the behavior of nanofluids. The following relation characterizes the fractal dimension d_f.

$$\Phi = \beta^{2-d_f} \qquad \text{(II 8)}$$

where φ is the nanoparticle concentration and β is the ratio D_{min} / D_{max} of the nanoparticle diameters in a fluid. The authors claim that nanoparticles in a nanofluid are fractal objects. Thus fractal theory can be used to predict transport properties of nanofluids[100]. The complete analysis hinges upon the consideration of Brownian motion as an important contributor to heat transfer enhancement. A fractal expression of the average nanoparticle diameter D_{avg} is given by:

$$D_{max} = [\,(4 - d_f) / d_f\,]^{1/4} * D_{avg} \qquad \text{(II 9)}$$

The co-authors[100] claim that the thermal conductivity k, of the nanofluid is a function of the thermal conductivities of the base fluid and nanoparticles, the average diameter of the nanoparticles in the base fluid, the nanoparticle concentration, the **fractal dimension**, and the physical properties of the base fluid. A **fractal** is a geometric entity that repeats in various configurations. The **fractal dimension** is a measure of complexity and need not be a whole number: a line segment would have a fractal dimension of '2'. The molecule that is the basis of this dissertation ZIF-8, the cage-like synthetic zeolite, is a prime example of a fractal (cf. **Part I, Fig. I 2.2, Fig. I 2.3, Fig. I 2.4**). The authors make some curious logical leaps when rationalizing the calculation of the thermal boundary layer. It was claimed that the hydrodynamic boundary layer of each base-fluid molecule could be approximated by the following relation:

$$\delta = 3 * D_f \qquad \text{(II 10)}$$

where D_f is the diameter of the base fluid molecule and δ is the diameter of the hydrodynamic boundary layer. The thermal boundary layer δ_T can then be expressed by[100]:

$$\delta_T = \delta / Pr \qquad \text{(II 11)}$$

where Pr is the Prandtl number. The fractal dimension is used in calculating the average radius of the nanoparticle in the base fluid. The researchers finally arrive at an equation that depicts the effective thermal conductivity $\mathbf{k_c}$ of the nanofluid [100]:

$$k_c = \frac{Q_c}{A_t \frac{\Delta T}{\delta_T}} = \frac{CD_f k_f \left[\frac{3}{\alpha}\sqrt{\frac{2k_B T}{\pi \rho_n}}\frac{\left(K^{1/2-d_f}-1\right)}{2d_f-1} + \frac{2\left(K^{1-d_f}-1\right)D_{max}^{1/2}}{d_f-1}\right]}{\Pr\left(1-K^{2-d_f}\right)\left(2-d_f\right)^{-1} D_{max}^{3/2}} \qquad \text{(II 12)}$$

The parameters in equation (15) have been previously defined but the most important parameter above is '**C**' which has an empirically determined value of **236.** This value was necessary to fit the experimental data to the equation. Although the authors use a thermal boundary layer based on Brownian motion (previously shown to be unimportant), their experimental results and conclusions corroborate some of the results obtained by Tatarko and Willing [53]. The effective thermal conductivity of the nanofluid decreases with an increase in the average size of the nanoparticle[100]. Smaller nanoparticles infused into a base fluid at a relatively low concentration have an increased thermal conductivity and thus enhanced heat transfer. It might be possible to correlate the fractal dimension with optical and absorption properties of nanofluids. In a humorous aside, Boqui *et al* sneak into the last section of the paper a disclaimer concerning the use of Brownian motion as basis for this analysis. They readily admit that nanoparticles greater than 16 nm do not

correlate with Maxwell's effective medium theory for the calculation of thermal conductivity and a correction might be necessary to the empirical constant '**C**' based on the size of the nanoparticle. Is it any wonder the value of '**C**' was 236?

Michaelides[101] presents a very thorough review paper on transport properties of nanofluids explaining in more detail most of the topics presented in **Part I** of this dissertation. In laminar flow of nanofluids at least 2 distinct *length-scales* must be considered; that of the nanoparticle with length **α** and that of the base fluid **L**. Turbulent flow might also require consideration of eddy-current lengths. In addition there are *time-scales* related to the thermal behavior of the nanoparticle and the base fluid[101]:

$$\tau_{th} = \frac{\alpha^2 \rho_s c_s}{3k_f} \quad \text{and} \quad \tau_{f\,th} = \frac{4L^2 \rho_f c_f}{k_f} \tag{II 13}$$

In addition there are timescales involved in the *flow* (equation of motion) of the nanoparticle and the advective flow of the nanofluid[101]:

$$\tau_M = \frac{2\alpha^2 \rho_s}{9\mu_f} \quad \text{and} \quad \tau_{fM} = \frac{L}{u} \tag{II 14}$$

These terms though foreign-looking are just derived from the Navier-Stokes equations and represent an attempt to render them dimensionless. In this case the drag coefficient and thermal conductivity become equal to 1 and solutions to the equations for various geometries and boundary conditions become tractable. All of the dimensionless numbers

so prevalent in chemical engineering are ratios of the pertinent timescales that relate momentum, heat, and mass transfer.

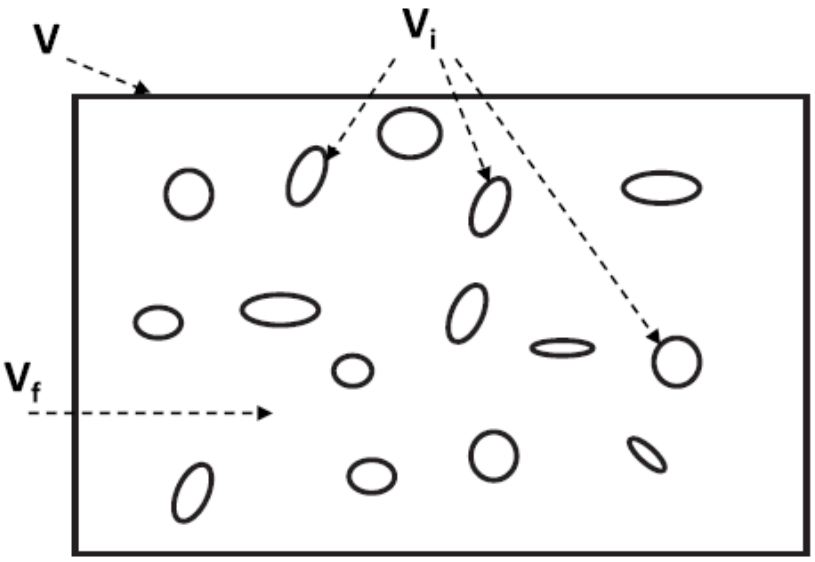

Fig II 1.12 This seemingly innocuous diagram shows a total volume **V** composed of the base fluid $\mathbf{V_f}$ and clusters of nanoparticles $\mathbf{V_i}$ which comprise a continuum. What delineates the nanofluid from a colloid is the ratios of volume to surface area[101]. The $\mathbf{V_i}$ is composed of '**n**' uniform spheres with radii **α**. The surface to volume ratio is **3 / α**. As the numbers **n** increase while keeping the total volume the same (smaller particles) the surface to volume ratio increases. Any processes dependent on surface area such as absorption, heat transfer, catalysis, or chemical reaction should be enhanced with the addition of nanoparticles.

Relative positions of nanoparticles within the base fluid are determined by these various forces[101]:

1. Bulk fluid motion
2. Various slip (lift) mechanisms
3. Electric forces between particle

4. Hydrodynamic forces between particles and particle-to-wall interactions.

Agglomeration is highly dependent on electric surface charges and the dielectric properties of the base fluid.

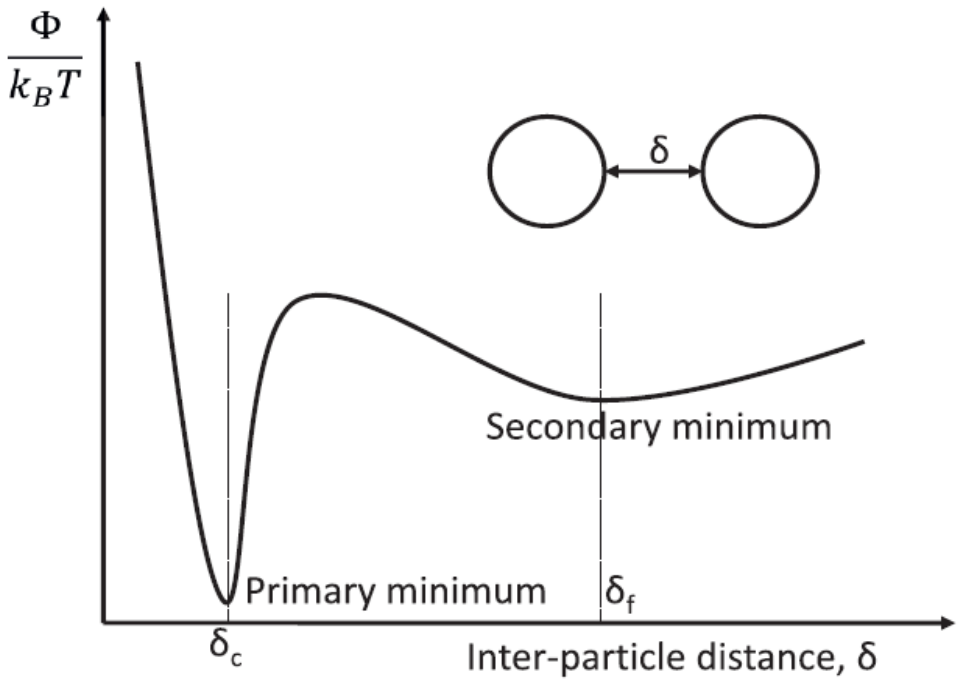

Fig. II 1.13 A potential energy diagram showing force versus distance. The primary minimum corresponds to **agglomeration**. The negative slope of the energy curve indicates particle–to-particle attraction. The 'deep' well portends a very strong bond which would be hard to break. The secondary minimum points to a much weaker attraction (shallow well) known as flocculation. These clusters **flocs** are easily broken during shearing, turbulence, or particle-wall interactions[101].

From an engineering point of view it would seem that volumetric flow through a channel is more important than viscosity[101]. This **bulk viscosity** is a function of nanoparticle distribution and should probably be measured via capillary tube and a differential pressure rather than a rotating viscometer. **Fig. II 1.14** on the next page describes effects of nanoparticle distribution.

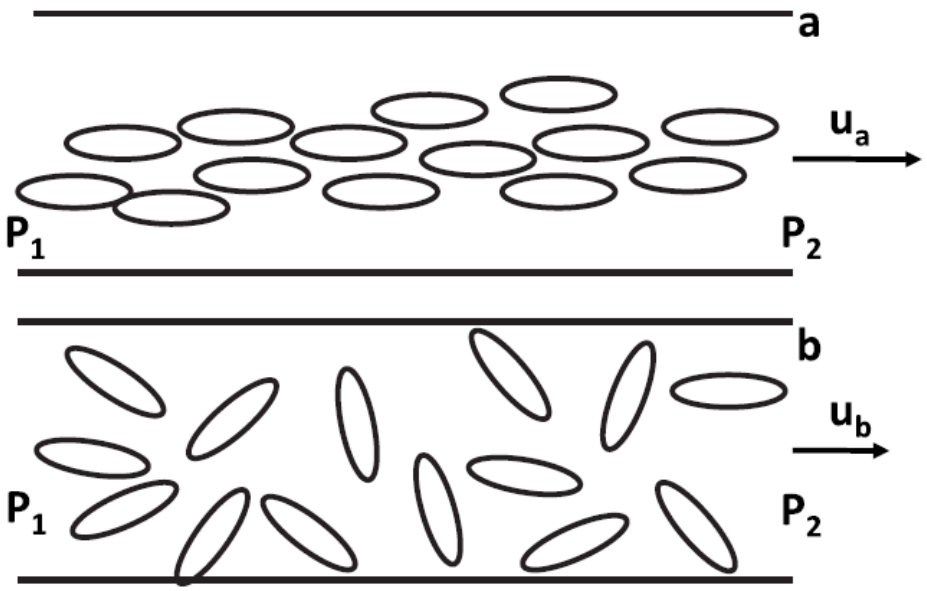

Fig II 1.14 Nanoparticles oriented according to Case $\mathbf{u_b}$ (lower figure) will have a greater viscosity than Case $\mathbf{u_a}$ above. It should now be apparent how critical electric forces between particles are. The two cases are analogous to 'laminar' versus 'turbulent' flow[101]. Note that the sizes and numbers of particles in each case are equal.

Michaelides makes an important point concerning the preparation of nanofluids for testing. It is not uncommon in peer-reviewed articles for the type and concentration of an added surfactant to be omitted. Surfactants have a substantial effect on the viscosity of nanofluids. Paradoxically, the thermal conductivity **k**, is dependent on aggregates and chain formation. Thus referring to **Fig II 1.15**, the thermal conductivity of Case **b** is greater than Case **a**. Remember it was previously mentioned that nanoparticles were often deformed and reduced in size subsequent to shearing after passing through a pump or turbine. Thus the thermal conductivity of a nanofluid may not be constant.

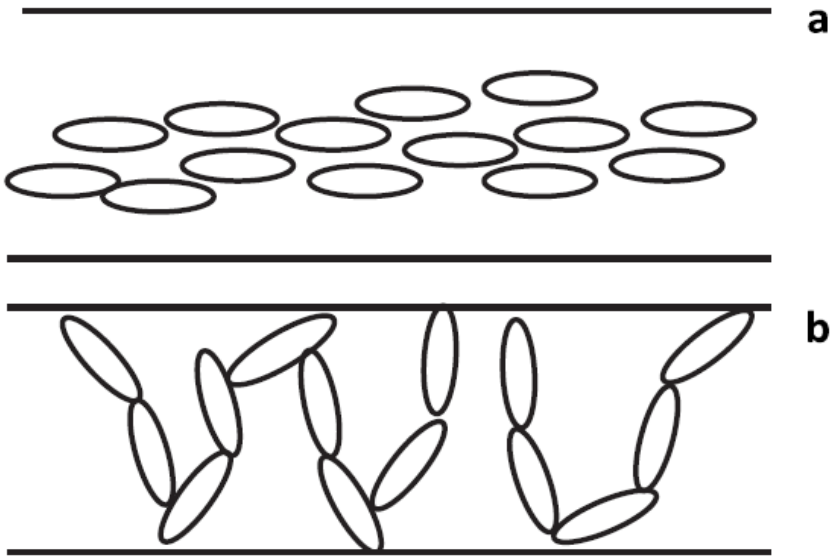

Fig. II 1.15 Thermal conductivity **k** of a nanofluid is enhanced when aggregates and chains are formed[101]. This is not a static condition and thus **k** may not remain constant. The thermal conductivity of Case **b** is greater than Case **a**[101].

In a paper that has important implications for the Heat Transfer Laboratories at the University of Louisville, Leong *et al*[118] studied entropy generation of nanofluids in circular tube flow. Based on the first and second laws of thermodynamics, a thermal system is optimized when entropy generation is minimized[118]. Enhanced heat transfer reduces entropy generation and irreversibility. The authors concluded the following:

1. Entropy generation is decreased as nanoparticle volume fraction is increased.
2. Entropy generation is decreased when the circular tube length is increased.
3. Entropy generation increases with increasing temperature.
4. Diameter changes of the circular tube have little effect on entropy generation[118].
5. Increased mass flow rate increases entropy generation.

The entropy discussed above is in fact a dimensionless quantity ψ defined as :

$$\Psi = S_{gen} / [Q / (T_w - T_i)] \quad \text{(II 15)}$$

In a problem that has yet to be resolved in the pumping of nanofluids through an enclosed thermo-fluid system it must be remembered that higher pressure drops require increased pumping power. Both the Stanton number and Eckert number are required when attempting to minimize entropy generation within a thermal system[118]. The Stanton number is defined:

$$St = \frac{h_{nf}}{\rho_{nf} u_{nf} c_{p.nf}} \quad \text{(II 16)}$$

The Eckert number is defined as[118]:

$$Ec = \frac{u_{nf}^2}{c_{p,nf} T_w} \quad \text{(II. 17)}$$

The convective heat transfer of the nanofluid, h_{nf}:

$$h_{nf} = \frac{Nuk_{nf}}{d_h} \quad \text{(II 18)}$$

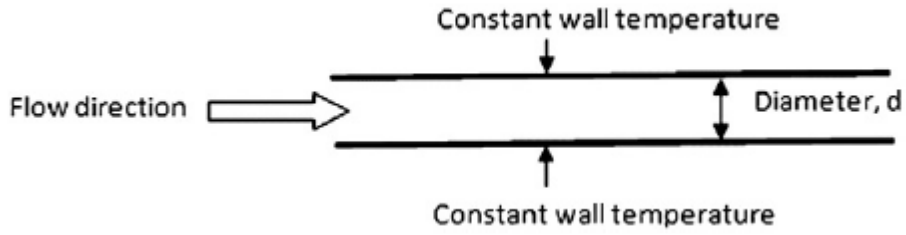

Fig. II 1.16 One of two possible ways to study energy effects and nanofluid flow. By contrast The University of Louisville heat transfer rig is supplied with constant heat, **Q** and the temperature differences measured[118].

where Nu is the Nusselt number and k_{nf} is the thermal conductivity of the nanofluid. The velocity of the nanofluid through the tube is u_{nf} and the temperature at the wall of the circular tube is T_w.

Computational fluid dynamics (CFD) has recently become an important investigational tool for the determination of process parameters, equipment dynamics, or material properties too difficult or impossible to measure directly. It is a complement to experimentation. Kamyar, Saidur, and Hasanuzzaman[119] in 2012 authored a paper on the use of CFD for the analysis of nanofluid behavior. The basic dissection of a problem involves these three steps[119]:

1. Integration of all of the conservation equations over a defined control volume.
2. Changing the obtained integral equations into algebraic equations via discretization.
3. Solution of the algebraic equations via numerical iterative methods.

The researchers rightly assert that for nanofluid flow with Peclet numbers greater than 10, the assumption of single-phase flow might not be justified[119]. Indeed they also posit the concept of the Richardson number **Ri** as a possible portent of two-phase flow. The Richardson number is a measure of buoyancy within a system:

$$\mathbf{Ri} = \mathbf{Gr} / \mathbf{Re}^2 \qquad \text{(II 19)}$$

where **Gr** is the Grashof number. An increasing Richardson number is indicative of non-uniform particle distribution within the nanofluid[119]. The thermophoresis and Dufour effects, both slip mechanisms that increase heat transfer within a nanofluid, suggest the use of a two-phase nanofluid model as the optimum for use in CFD studies. This results in a modified expression of the conservation equations necessary for modeling[119].

There is a substantial gap between 10 years of research on heat transfer enhancement and bona fide engineering applications. Wu and Zhao in a review paper from 2013[120], posit on many of the contradictory experimental results, lack of fundamental explanatory theory, and irrational assumptions used by a host of researchers. They decry the lack of a comprehensive database of nanofluid thermo-physical properties yet do little to discuss some of the results presented by others on specific hard-core engineering problems: fouling, nanoparticle shearing and size degradation, nanofluid stability, and experimental error propagation. More positively they do suggest that CFD studies may give insights into the interactions of nanoparticles and the flow boundary layers[120].

As a counterpoint to the paper of Wu and Zhao, Liu and his co-authors[121] presented on the enhancement of heat exchanger efficiency due to nanofluids. This is an example of old-school hard-core engineering meeting state-of-the-art technology. Heat exchanger design and analysis had gone through decades of evolution and there was little to be gained from changes to the physical model itself. The authors use the concept of **number of transfer units** (NTU) in their exposition.

Assuming a two-stream ($\mathbf{m_1}$ and $\mathbf{m_2}$) heat exchanger with one stream $\mathbf{m_1}$ enhanced with nanoparticles, the NTU is related to the *overall heat transfer coefficient* **U** by[121]:

$$NTU = \frac{UA}{C_{\min}} \tag{II 20}$$

where A is the overall surface area and C_{min} is the minimum of $\mathbf{C_{p1}}*\mathbf{m_1}$ and $\mathbf{C_{p2}} * \mathbf{m_2}$. The enhanced NTU is described by:

$$\frac{NTU}{NTU_0} = \frac{UA}{(UA)_0} \qquad \text{(II 21)}$$

where the subscript 0 refers to the baseline. This is similar to quantities generated in the Heat Transfer Laboratories at the University of Louisville: $\mathbf{h / h_o}$, the enhancement factor. The authors were sure to also explain that the enhancement was optimal for a shell and tube heat exchanger with 2 liquids involved. A cross-flow exchanger with ambient air as a cooling agent did not experience much enhancement. This is standard in the industry. Air-cooled heat exchangers whether via natural or forced convection are cheap yet not very effective at removing massive amounts of energy. Nanoparticle-enhanced fluids do little to improve this.

Hung and his co-authors[128] help understand the heat-exchanger concept further. The heat transfer coefficient of air in natural convection is approximately 5-25 W/m^{2}K and for forced convection, 10-200 W/m^{2}K. Water however has a much larger coefficient: for natural convection, 20-100 W/m^{2}K and for forced convection, 50-10,000 W/m^{2}K. The researchers hope to find a particular nanoparticle to enhance the heat transfer coefficient **h**, so that the design of the heat exchanger can be made smaller. A very solid attempt is made to quantify the uncertainty in the measurement of thermal conductivity, flow rate, voltage, weight, and temperature[128]. The uncertainty in the thermal conductivity is[128]:

$$u_{m,k} = \sqrt{(\Delta k_t/k_t)^2+(\Delta W/W)^2+(\Delta T/T)^2} \qquad \text{(II 22)}$$

If the thermal conductivity is accurate to ± 5% and the weights accurate to ± 0.01 gram and the temperature measurement accurate to ± 0.05º C, the best accuracy of the

experiment is about 5 %. This is consistent with calculations done by this researcher. Heat transfer enhancement less than 5% is not worthy of consideration due to propagation of errors.

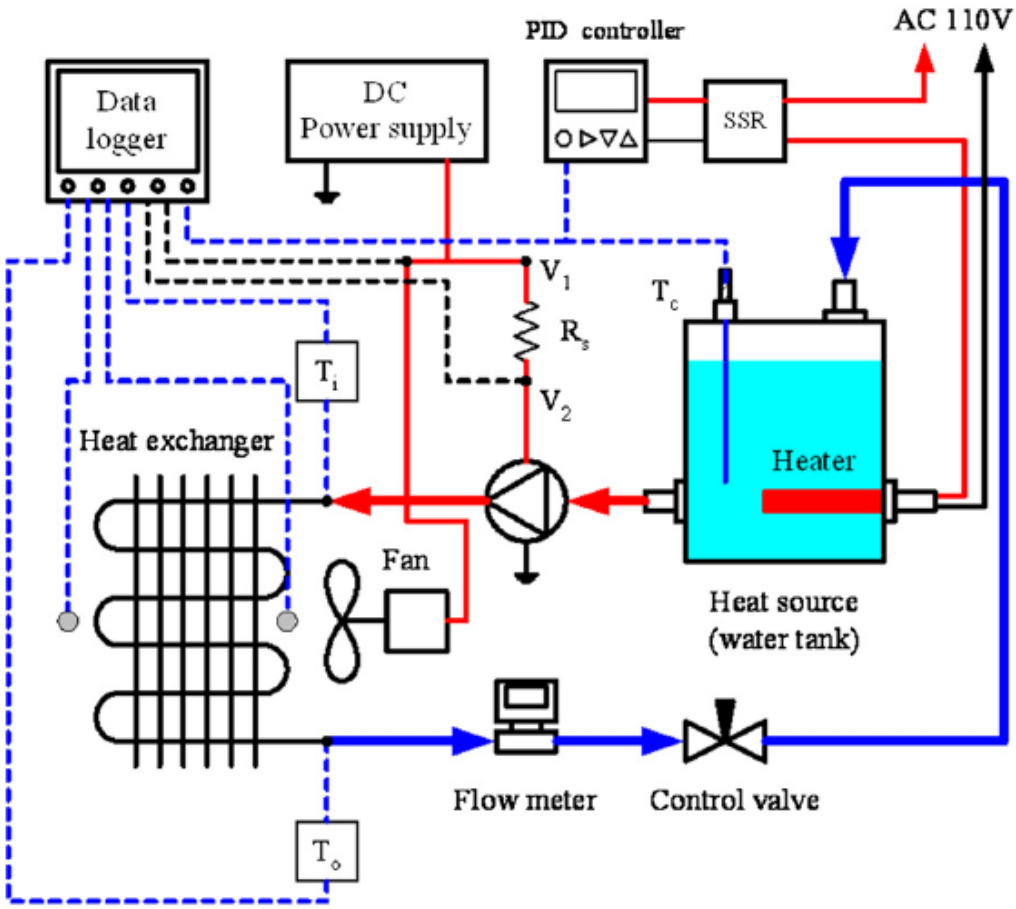

Fig. II 1.17 The heat transfer rig designed and built by Hung *et al*[128] This is much more sophisticated than the apparatus available for use in the Heat Transfer Laboratories at the University of Louisville. The presence of the fan makes studies of forced convection possible. However the presence of more equipment adds to increased sources of error.

As it has been found in our own heat transfer laboratories, the best enhancement occurs at low temperatures, 30-40º C. This results in a decreased heat exchanger area of about 1%

for every percent of enhancement. Unfortunately the high volume-percent of nanoparticles in the base oil required to effect this results in increased pumping power.

To summarize the literature regarding heat transfer enhancement with nanoparticles over the last 15 years:

1. Experimental results of heat transfer studies obtained are rarely reproducible.

2. Nanoparticles processed via mechanical pumps and compressors are subject to agglomeration and physical distortion.

3. Nanoparticle addition to heat transfer agents may lead to hastened and increased fouling of tubes and pipes.

4. Heat transfer enhancement less than 5% may be considered negligible due to increased pumping costs and propagation of errors in calculations.

2. ZIF-8 Synthesis and Properties

The synthesis of ZIF-8 has been somewhat problematic. It is relatively easy to make [47,49] yet the yield is quite small; only ¼ gram per reaction. For any type of testing purpose or use as an engineering material this is unacceptable. In addition there is much waste of methanol, the mother liquor. Demir *et al* [102] proposed a scheme to reduce this waste thus making favorable effects environmentally and economically. In a typical synthesis, 2.4 g of zinc nitrate hexahydrate [$Zn(NO_3)_2 * 6H_2O$] was dissolved in 90.4 g of methanol. An additional solution of 5.3 g of 2-methyl imidazole was dissolved in 90.4 g of methanol. The solutions were combined, stirred for up to one hour, and centrifuged to obtain a solid product. The mother liquor was poured off and retained. The product was washed and centrifuged 2 additional times before drying for 24 hours in an oven at 80°C [47,49,102]. The molar composition of the mixture prior to centrifuging was 1 Zn^{2+} to 7.9 2-methyl imidazole, to 695 methanol. This reaction and a scaled-up version for spray drying analysis, produced the ZIF-8 used for study in this dissertation. The ratio of methanol to Zn^{2+} determines the average particle size, in nanometers, of the product. In this case 238nm [102]. The authors of the article tried three separate techniques to make use of the retained original solution for further synthesis of ZIF-8.

The mother liquor was aged for 24 hours before any additional processing. In process A, additional amounts of [$Zn(NO_3)_2 * 6H_2O$] were added and centrifuged to obtain additional ZIF-8 product. In process B and C the pH of the solution was raised from 7 to 9 and additional amounts of [$Zn(NO_3)_2 * 6H_2O$] added [102]. The flow chart on the next page depicts the recycle process.

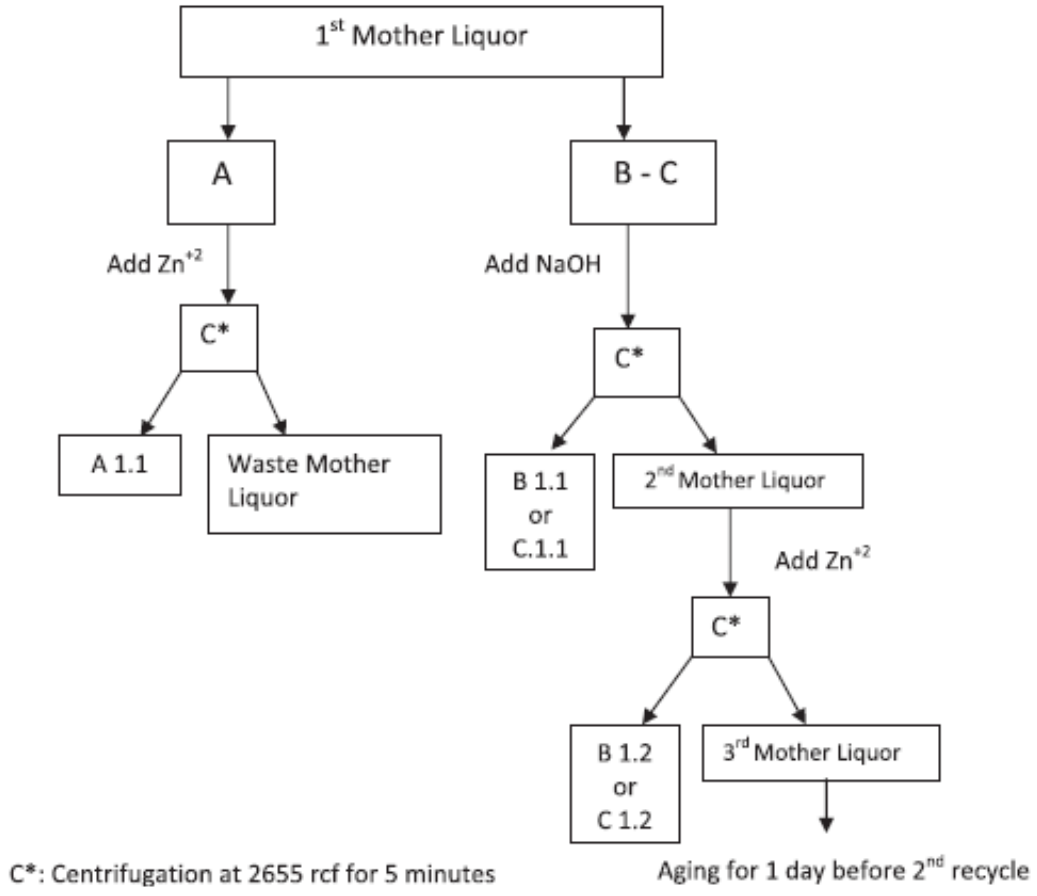

Fig. II 2.1 A flow chart depicting the recycle of the mother liquor for additional synthesis of ZIF-8. The adjustment of pH in process B helps precipitate additional product. XRD patterns produced by the authors show the characteristic fingerprint of ZIF-8. The reuse of the mother liquor doubles the product[102].

It will be shown in **Part III** that while the author's efforts are laudable, the spray drying process is far superior in the production of product and the reclamation of methanol.

Chen, Yang, Zhu, and Xia [103] in an article published in the *Journal of Materials Chemistry A*, also espouse some additional methods of ZIF-8 synthesis. It should be remembered that ZIF-8, a metal-organic framework, (MOF), falls in the class of materials

known as zeolites. It is estimated that the world-wide market for zeolites is currently at 350 billion dollars annually [103]. **Table 2.1**[103] below shows relationships between traditional zeolites and the newer class of MOF's.

Table 2.1

Comparison content	Zeolites	Zeolitic imidazolate frameworks
Framework type	Inorganic	Inorganic-organic
Composition	Si; Al; O	Zn; Co; C; N; H and more
Secondary building units	$[SiO_4]$ and $[AlO_4]$	$M(Im)_2$
Topology	Around 200	Found over 100; the number may increase exponentially
Stability	Depending on the Si/Al ratio, thermal and chemical stability are generally high	Thermal stability up to 500 °C and high chemical stability in organic and aqueous media
Compatibility	Poor interaction with polymers	Better compatibility with organic polymers
Functionality	Tuneable Si/Al ratio; generally difficult in functionalisation	Rich chemical functionalities with organic linkers
Development	Over 50 years	Around 10 years
Application prospects	Low-cost; large scale for industry applications	Expensive; potential for industry applications

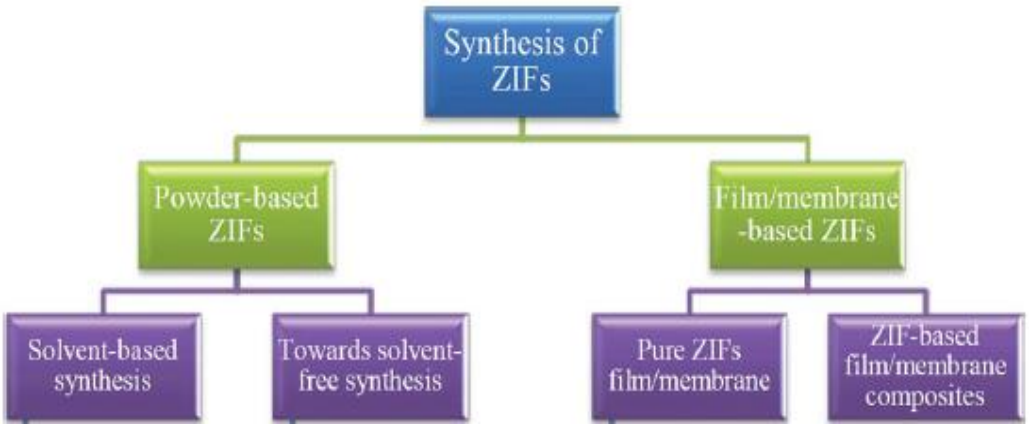

Fig. II 2.2 The current state of the art[103] in the production of a newer class of zeolites known as MOF's, **metal organic frameworks**. Work at the University of Louisville has produced world-class examples of product in each category. The work in this dissertation is focused on the production of powder-based ZIF-8 via a solvent based synthesis. Researchers in Prof. M. Carreon's group have produced ZIF film

The authors claim that the addition of sodium formate enhances the production of tunable crystal sizes in the range of 10 nm to 65 nm. The current rage in ZIF-8 synthesis revolves around the use of aqueous ammonia [103]. It also is supposedly a modulator of particle size and in fact much cheaper than solvent methods using organics.

The solvent based methods are quite inefficient and thus costly. Large-scale production of ZIF's via this method is just not possible. Most recently, some *mechanico-chemical* methods using ion and liquid-assisted grinding in a ball mill in the presence of salts has produced acceptable forms of ZIF-8. **Fig.2.3** below gives a schematic of the process [103].

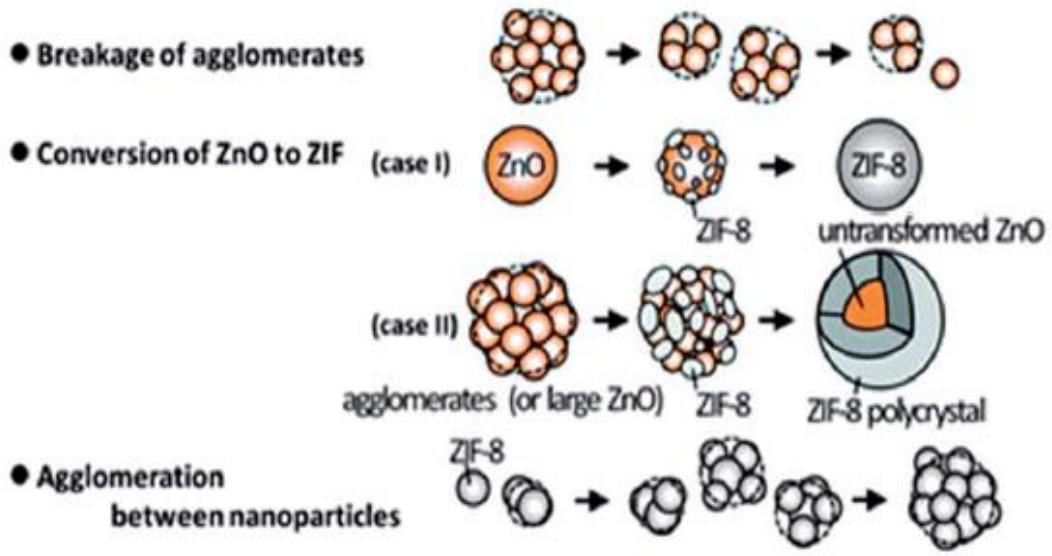

Fig. II 2.3 This is a schematic of three simultaneously occurring processes that facilitate the production of ZIF-8 from zinc oxide in the presence of 2-methyl-imidazole and ammonium salts. Interestingly enough, the original size of the ZnO determines the size of the resulting ZIF-8 crystal [103].

Researchers have realized that the future for these MOF's, regardless of the outstanding properties hinges on cost-effective production.

Tan, Bennett, and Cheetham[104] in a paper published in 2010 reported some physical properties of the ZIF-8 molecule. These were closely tied to the framework density. The authors claimed an elastic modulus of 3 to 10 GPa and a hardness of 300 MPa to 1.1 GPa. A physical density of 0.95 g/cm^3 was reported[1002]. Elastic modulus, is a measure of intrinsic stiffness under load[104] while hardness indicates a resistance to plastic deformation. The elastic modulus in this paper was determined via a nano-indentation technique and was inversely correlated to the porosity. The ZIF-8 molecule resides in the lower end of densities in the MOF/ZIF family; it is highly porous with a large void space[104], yet it still retains a robust elastic modulus. It has become evident to this researcher that the ZIF-8 molecule is more 'organic' than metallic.

Previous studies have shown ZIF-8 to have very large surface areas ~1200 m^2/g which are available for the capture and adsorption of various molecules such as carbon dioxide. A number of researchers are exploring alternate methods of synthesis in hopes of achieving more plentiful yields. Low *et al*[105] recently published a paper devoted to the production of the 3-dimensional sphere-like ZIF-8 from the 2-dimensional layered ZIF-L via a phase transformation. The usual method of MOF synthesis is one of reaction, crystallization and transformation within one pot. The authors claim that their more novel method of construction may open-up new avenues for the tuning of physical properties.

The researchers Chen, Bai, Zhu, and Xia[106] attempted to take a different approach to the synthesis of ZIF-8. The usual one-pot approach as noted in the previous paragraph required an inordinately large ratio of 2-methyl imidazole (MIm) to Zn^{2+} ; 70:1. This led to much waste and has prompted some to seek out better paths to construction of a 'greener'

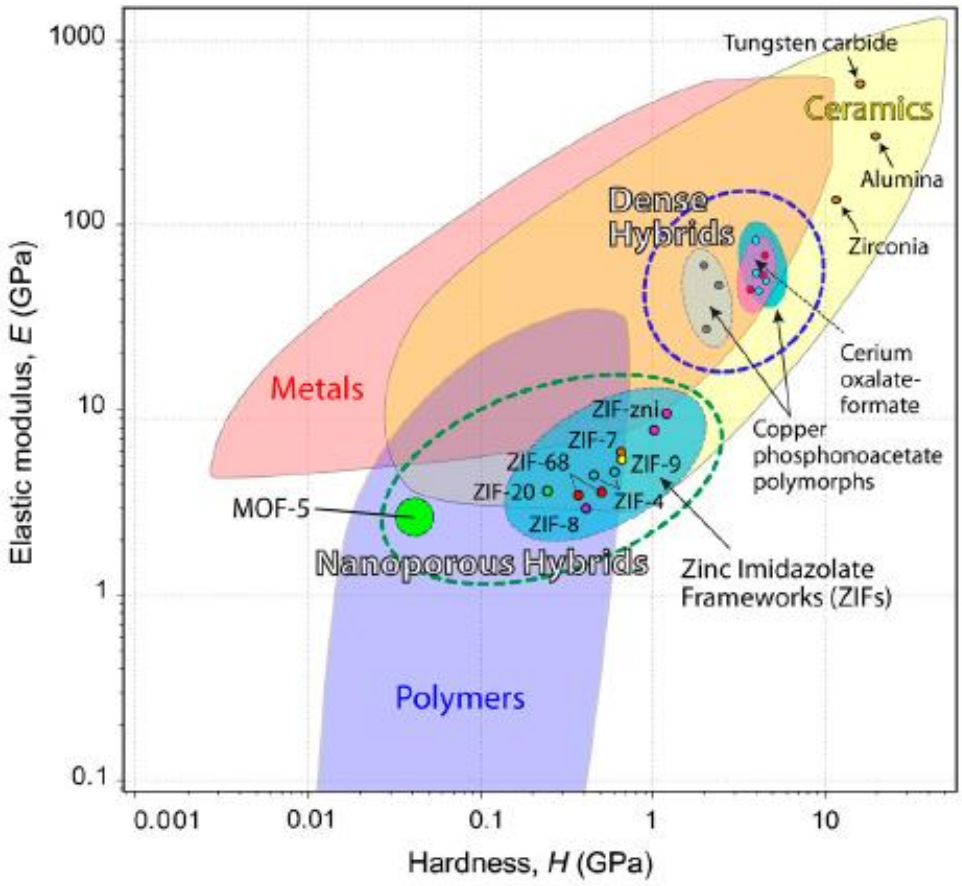

Fig. II 2.4 This schematic is a particularly informative picture of two of the most important physical properties of a material; its elastic modulus and its hardness. Notice where ZIF-8 fits into the hierarchy of nano-porous molecules and more traditional engineering materials[104].

ZIF-8 molecule. Kida *et al*[107], claimed to have built the ZIF-8 molecule from an aqueous solution at room temperature with a ratio of MIm to Zn^{2+} of 20 to 1. This researcher has attempted to reproduce these results and has failed three times. This has led to some jaded views on research and truthfulness within the scientific community. Chen *et al*, attempted to synthesize ZIF-8 in in an aqueous ammonia solution at

stoichiometric ratios. Two mmoles of zinc nitrate hexahydrate (0.585 g), were dissolved in water an added to a solution of water with 35 wt % ammonia and 4 mmoles of 2-methyl imidazole (0.323 g). The reaction produces, it is claimed, at room temperature, true crystalline ZIF-8 after 24 hours. As usual the product was centrifuged ,washed, and dried numerous times. The authors produced SEM micrographs and XRD patterns that compared favorably with the prototypes synthesized by Venna[47,49].

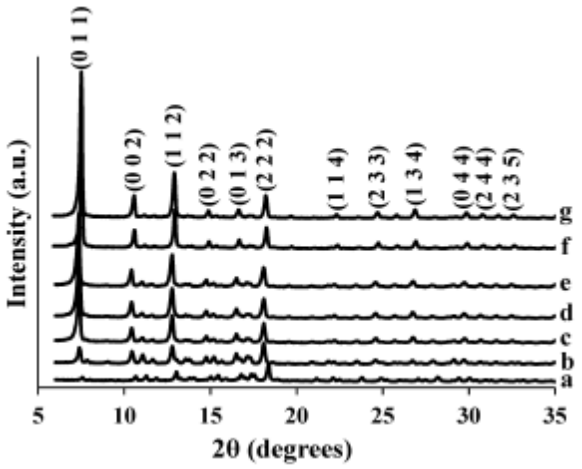

Fig. II 2.5 The XRD patterns generated by the product of the synthesis of Venna *et al.* The structural evolution of ZIF-8 over time: a) 20 minutes, b) 30 minutes, c) 40 minutes, d.) 50 minutes, e) 60 minutes, f) 12 hours, g) 24 hours[47,49]. This was a solvent-based reaction instituted with a massive excess of MIm. The kinetics of this transformation follow Avrami's law[47,49].

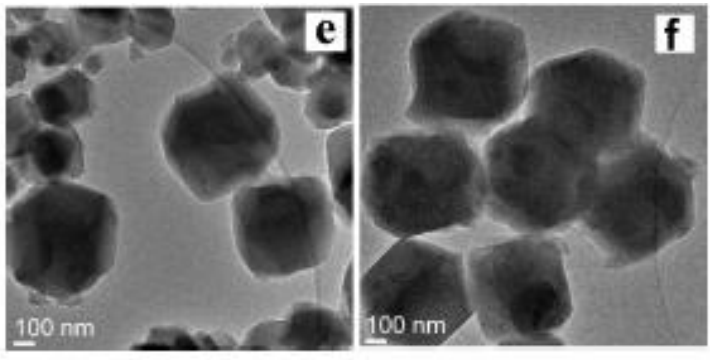

Fig. II 2.6 TEM micrographs of ZIF-8 generated by the solvent based process of Venna *et al*[47,49].

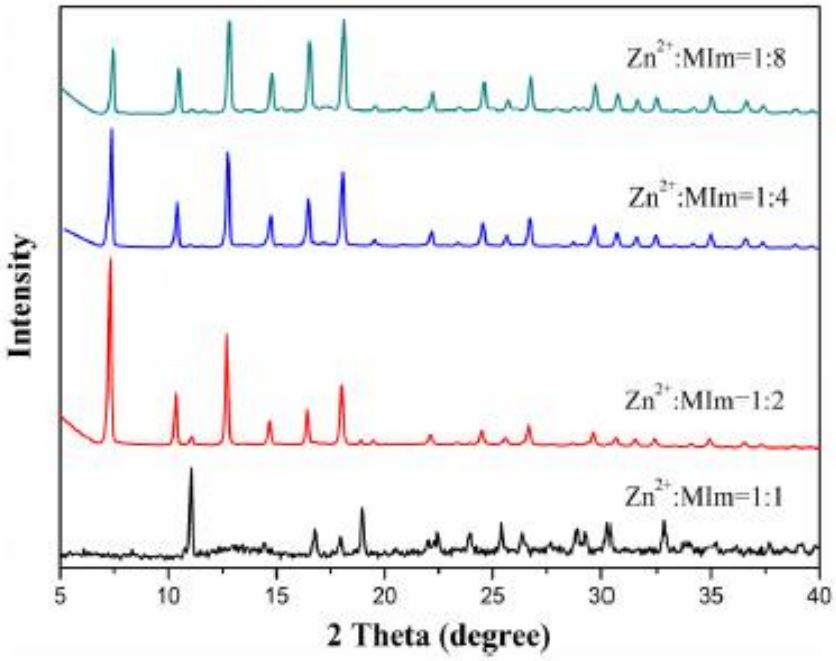

Fig. II 2.7 The XRD patterns generated by the synthesis of ZIF-8 in an aqueous solution of 35% ammonia. The Zn^{2+} MIm ratio of 1:1 is somewhat suspect, (there appears to be another product), yet the other reactions produce a product that compares favorably with those depicted in **Fig. 2.5** at a more reasonable ratio of reactants[107].

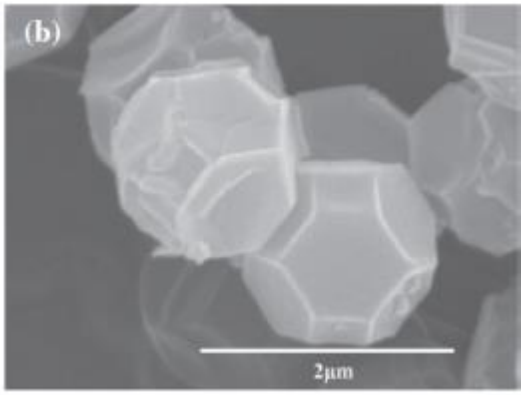

Fig. II 2.8 SEM micrographs of a ZIF-8 product synthesized from an aqueous ammonia solution (35%) in a Zn^{2+} / MIm / ammonia molar ratio of 1:4:400. The sizes

and morphology compare with the molecules depicted in **Fig 2.6**[107]. Like all ZIFs this product required a long drying period; about 24 hours.

The production of ZIF-8 requires a stoichiometric ratio of Zn^{2+} to 2-methyl imidazole at 1:2. The researchers claim that the size and morphology of the ZIF-8 crystal can be controlled by adjusting the concentration of ammonia. If this report is valid and the results reproducible, this method provides an efficient and cost-effective path to the synthesis of ZIF-8[107]. An economic analysis is always germane to engineering proposals.

The previous discussion centered around novel and enhanced synthetic regimes for the production of ZIF-8. A paper generated in 2014 by Bazer-Bachi *et al*[108], noted that while many alternative schemes for the synthesis of various MOFs are currently being proposed, little effort has been made to explore alternative methods of *framework shaping*. Since the catalytic and adsorption properties are so highly valued in a material like ZIF-8 are there mechanical methods available to shape the highly porous framework? This might be called *extreme tuning*. These researchers submitted 0.1 gram samples of ZIF-8 to compression testing at 18 kN. About 90% of the crystallinity and total BET surface area (1433 m^2/g) was preserved. It was previously noted that ZIF-8 had decent hardness and elastic modulus properties[104]. The application of a compression force and the determination of subsequent physical characteristics will provide information necessary for scaled-up production of these MOFs for use in industrial reactors and separation columns. In fact these ZIF-8 molecules are being *pelletized*. The authors claim that the catalytic activity remained the same after *tableting* (compression), and in fact when considering the 10% reduction in area the activity had increased[108]. The result;

more pellets (of smaller size), can be introduced into a packed-bed reactor. The 10% loss of crystallinity and resulting amorphization was also inconsequential. A schematic on the next page gives a pictorial of the process.

Fig. II 2.9 The tablets shown in the photograph are a result of compressing ZIF-8 at a force of 6.8 kN. It can be seen that there would be a definite advantage in the mechanical loading of these tablets into a reactor or column[108].

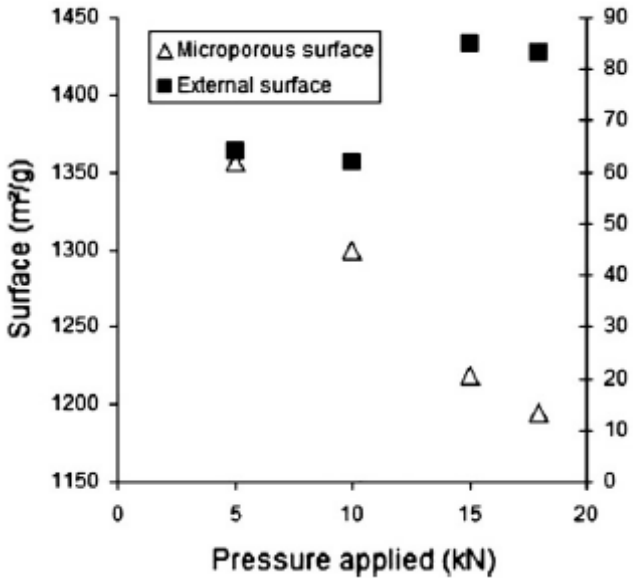

Fig. II 2.10 This graph while seemingly contradictory shows that as the microporous surface area of ZIF-8 decreased dramatically during compression, the external surface area remained constant or increased. If the catalytic activity remained constant that leads to the belief that almost all of the reactions / separations are taking place at the surface and not within the voids[108].

The **Fig. II 2.10** above may provide some information on the thermal properties of ZIF-8. It is well known that this MOF is going to have massive surface area. Is all of that area available for heat transfer? Will this be an example of an 'organic' nanoparticle that might act as an enhancer of heat transfer? The results will come in **Part III**.

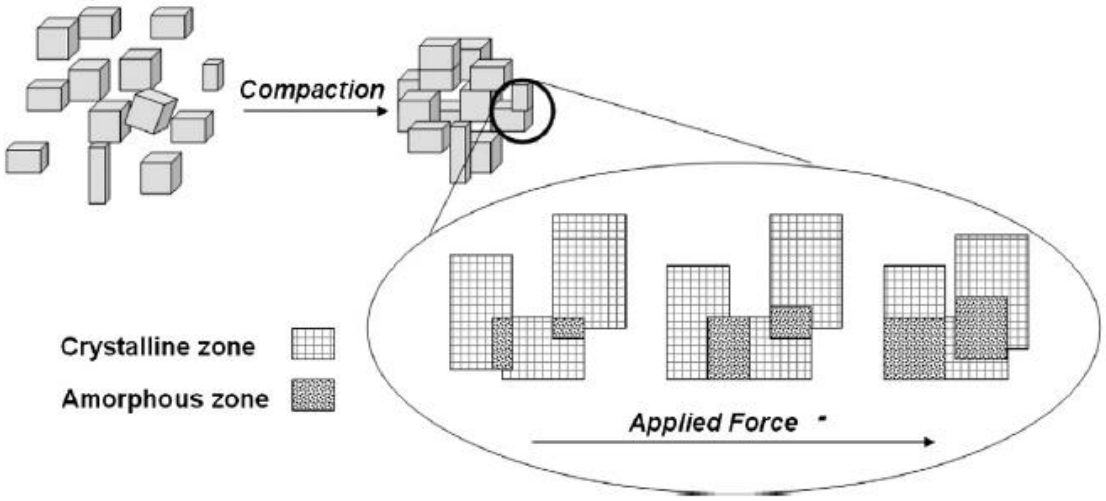

Fig. II 2.11 This schematic depicts the compression (pelletizing) of ZIF-8. As more force is applied the area of amorphous regions increases[1008]. Is there an optimum region?

ZIF-8 is usually synthesized via a solvent-based, microwave initiated, or ammonia-enhanced aqueous solution. Cho, Jun Kim, Se-Na Kim, and Ahn proposed a *sonochemical* approach to synthesis in a pH-adjusted solution. The sonic waves cause the collapse of the ZIF-8 crystal structure and thus a reduced size[109]. After pelletizing (cf. **Fig. II 2.9** and **Fig. II 2.11**) the catalytic properties remained the same. In contrast to other synthetic routes, the researchers claimed a near stoichiometric ratio of Zn^{2+} to MIm along with small amounts of triethylamine were introduced into a custom-made tube reactor fitted with a sonic bar. The yield was approximately 85%[109]. The tableted ZIF-8

products measured in the 400-500 μm diameter range. The authors after much experimentation claimed that this technique could reduce the total synthesis/pelletizing process down to about 2-3 hours. This would be highly desirable for industrial applications.

In an issue of the *Journal of Physical Chemistry C*, Zhang and Jiang used molecular dynamics simulation to extract the thermal conductivity of ZIF-8 and reported it as 0.165 W/mK [110]. This simulation is particularly interesting because of the 'organic' nature of ZIF-8. Molecular dynamics simulation me[87] the forces between colliding molecules. Prescriptions from statistical thermodynamics translates these forces into physical properties. Statistical thermodynamics is the bridge between classical mechanics and thermodynamics. The formula for thermal conductivity κ is:

$$\kappa = \frac{V}{3k_B T^2} \int \langle \vec{J}(0) \cdot \vec{J}(t) \rangle dt \qquad \text{(II 23)}$$

where V is the volume, k_b is Boltzmann's constant, T is temperature, and J is the heat flux. The brackets < > denote time average[110]. In turn, the heat flux $\vec{J}$ is:

$$\vec{J} = \frac{1}{V}[\sum_i E_i \vec{v}_i - \sum_i \vec{\vec{S}}_i \vec{v}_i] \qquad \text{(II 24)}$$

where v_i is the velocity of atom i, E_i is the total energy both kinetic and potential, and S_i is the symmetric stress tensor[110]:

$$\vec{\vec{S}} = \begin{bmatrix} S_{xx} & S_{xy} & S_{xz} \\ S_{xy} & S_{yy} & S_{yz} \\ S_{xz} & S_{yz} & S_{zz} \end{bmatrix} \qquad \text{(II 25)}$$

The stress tensor includes contributions from stretching, bending, torsion, Lennard-Jones, and columbic interactions. This set of parameters is run in what is known as the *NVT* ensemble where the volume and temperature are held constant. A number of molecules are placed in a 'box' (mathematical) and allowed to collide. The force of each collision is measured and averaged over time. The transport properties can then be calculated. As a check, the molecules are then submitted to the *NVE* ensemble and any statistical anomalies in calculated property values noted. Interestingly Zhang and Jiang ran another set of simulations in an attempt to deduce any lattice vibrations (phonons) due to heat flux. Remember from **Part I**, it was noted that *phonon transport* was one possible mechanism for enhanced heat transfer due to the addition of nanoparticles.

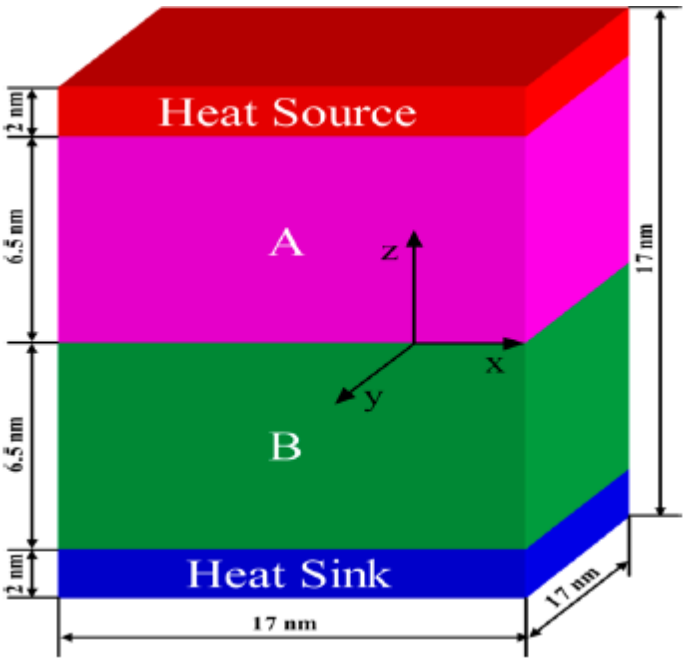

Fig. II 2. 12 In an analogous yet inverse manner to the original *NVT* simulation, a heat flux is imposed on a set of atoms and the side-to-side-interactions (vibrations) measured. The mathematical 'box' contains 10 unit cells in each direction[110].

The heat flux from $J_{A \rightarrow B,\alpha}$ that is from A to B in the α direction is given by:

$$J_{\mathrm{A}\rightarrow \mathrm{B},\alpha} = -\frac{1}{2S}\sum_{i\in \mathrm{A}}\sum_{j\in \mathrm{B}} F_{ij\alpha}(v_{i\alpha} + v_{j\alpha}) \qquad \text{(II 26)}$$

where S is the cross-sectional area between A and B, $F_{ij\alpha}$ is the force between atoms i and j in the α direction and $v_{i\alpha}$ and $v_{j\alpha}$ are velocities of the i and j molecules[110]. The majority of phonon contribution to the overall thermal conductivity, (60%), comes from vibrations in the z direction[110].

To summarize the literature search on the topic of ZIF-8 properties and production it should be emphasized that little was available on actual determination of hardcore properties such as thermal conductivity, specific heat, and density. That left the bulk of that work to us in the Heat Transfer Laboratories at the University of Louisville. Some progress has been made in alternative and more efficient methods of synthesis of the ZIF-8 molecules with an eye to engineering economy. For all of the efforts found in the literature search this author still believes the use of a spray dryer as separation unit will afford greater yields and possible recovery of most of the methanol solvent. Experimentally, it will be interesting to see whether all of the surface area of the ZIF-8 molecule will be available for heat transfer. The literature indicates that it will not (cf **Fig II. 2.10**).

3. Spray Drying

One of the problems encountered when this study of ZIF-8 was begun was the tedious method of production and resulting low yield from its synthesis. A large excess of 2-methyl imidazole was required for the reaction to proceed and much of the methanol mother liquor was discarded. It took approximately 2.5 hours to make ¼ gram. It was thought that perhaps a more efficient and economical path might be found. In the previous section (**II. 2**) a number of authors proposed different synthetic routes. This researcher chose a different tack and approached the problem from a unit operations perspective; the use of *spray drying* to separate the solid ZIF-8, the product of reaction, from the mother liquor in production-size quantities.

Vehring, Foss, and Lechuga-Ballesteros authored a paper[111] on the theoretical and experimental foundation for the use of spray dryers in industry. This tome is in fact a compilation, review and expansion on much of the previous work done on spray drying. In addition to providing an analytical model and a numerical solution to the coupled heat and mass transfer equations, the researchers built an improved *droplet-chain chamber* to study the time evolution of single droplets. Experimental verification of the heat and mass balances during spray drying is complicated by many droplet-to-droplet interactions. The droplet-chain technique generates a single droplet at a time via a vibrating orifice into an atmosphere of controlled humidity. The time to distance relationship vis-à-vis the droplet size and shape can be correlated. Droplet-droplet collisions are minimized. The difference between the vapor pressure of the solvent and its partial pressure in the gas phase is the driving force for drying. The rate of evaporation is balanced by the energy flux required for the enthalpy of vaporization and

the energy flux to the droplet surface[111]. As solvents evaporate solutes migrate to the droplet center.

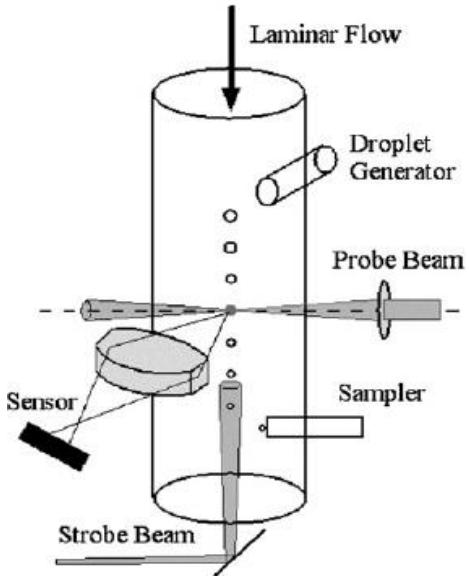

Fig II.3.1 The improved droplet-chain chamber constructed by Vehring *et al*. One of the probes, a laser, determines the droplet size by measuring the elastic scattering pattern. The second laser measures the time-distance evolution[111].

The equation governing the evolution of the solvent free particle is expressed by Fick's 2nd law of diffusion:

$$\frac{\partial c_i}{\partial t} = \frac{D_i}{r_s^2}\left(\frac{\partial^2 c_i}{\partial R^2} + \frac{2\partial c_i}{R\partial R}\right) + \frac{R\partial c_i \partial r_s}{r_s \partial R \partial t}, \qquad \text{(II 27)}$$

where c_i is the concentration of the solvent D_i the diffusion coefficient of solute i, and r_s is the droplet radius. $R = r / r_s$ is the normalized radial coordinate[111]. The steady-state evaporation of the solvent is proportional to the surface area. This equation has an analytical solution which does not take into account the changing diffusion coefficient.

However the droplet-chain technique permits calculation of the initial drop diameter d_0 emerging from the vibrating orifice plate exactly[111]:

$$\rho = c_{\mathrm{f}} \cdot \left(\frac{d_0}{d_{\mathrm{g}}} \right)^3 \qquad \text{(II 28)}$$

where ρ is the density of the particle, c_f is the concentration of the solute and d_g is the final particle diameter. It was determined that two dimensionless parameters described the particle formation succinctly: the Peclet number *Pe,* which describes the change in surface accumulation due to diffusion and the solute saturation *S*, which predicts precipitation[111]. To be sure, particle formation includes nucleation, crystal growth, and shell buckling mechanisms, yet the above numbers accurately predict the particle formation well. This knowledge along with use of the improved droplet-chain mechanism can help tune particle sizes and design possible coatings for enhanced heat and mass transport.

Anandharamakrishna in an interesting article[112], claims that an important parameter to considered in the spray-drying process is the residence time distribution (RTD) of the particle in the chamber. In review, spray drying involves 4 distinct processes: 1.) atomization of the liquid feed, 2.) contact between the spray and the drying medium (usually hot air or nitrogen), 3.) moisture evaporation, and 4.) separation of the particle from the drying stream. A schematic on the next page **Fig II. 3.2**, depicts the location of these processes[112]. Complete tomes could be written on each of these yet the author uses computational fluid dynamics (CFD) to promote the concept of RTD. This concept is particularly important when dealing with temperature-sensitive proteins and

pharmaceuticals. Excessive RTD denatured some proteins. At this time no methods exist to measure the RTD of individual particles. Thus CFD studies were necessary. Complicating the issue further is the fact that the particle-particle and particle-drying gas interactions occur in the turbulent regime.

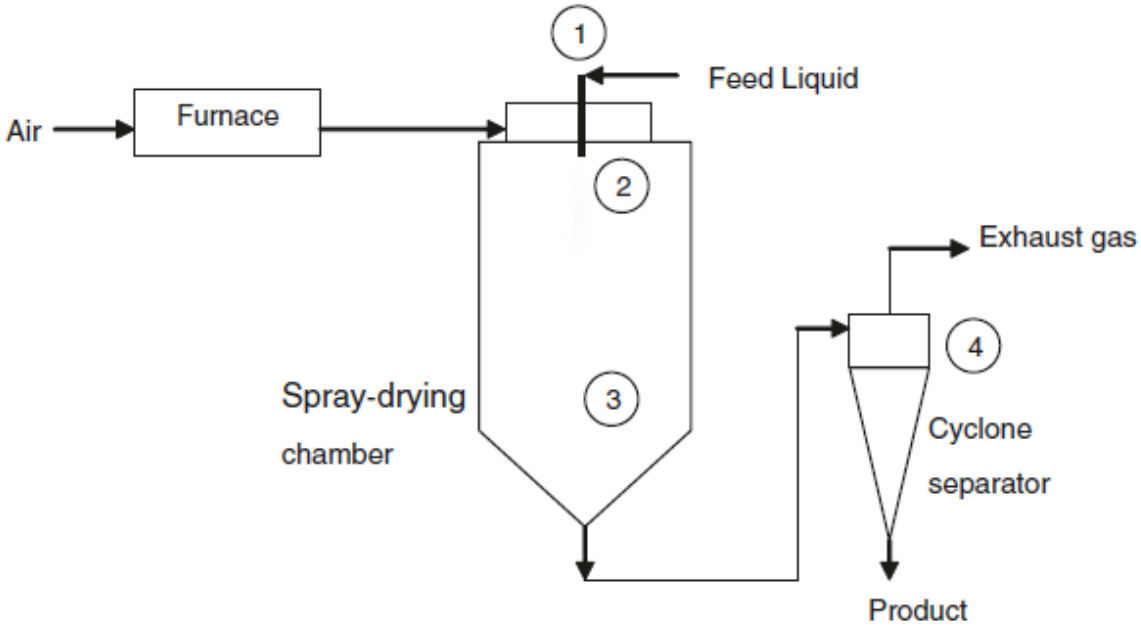

Fig. II 3.2 The spray drying process depicting 1.) atomization, 2.) spray-gas contact, 3.) evaporation, and 4.) separation. Residence time distribution is critical in sections 2.) and 3.)[112].

In contrast to the work by Vehring *et al*[111], Vincente *et al*[113] studied the kinetics of the drying process on a molecular level. These researchers claim that fast evaporation and short drying times promote smooth spherical particles while the concentration solute in the feed c_f determines the relative thickness of the particle skin. Thus drying is controlled by droplet size d_D temperature T_{out} and concentration c_f[113]. While it seems that this writer has reviewed a number of papers with similar titles in this dissertation it is important to note that this is only a small fraction of what has been read. Each paper presented has

offered an augmentation of previous information. Vincente and his co-authors have tried to present a rational approach to identifying and quantifying the various parameters affecting the spray drying process[113]. A schematic detailing their work is presented in **Fig. II 3. 3**. This is a vast improvement in a similar cartoon presented by Masters[115].

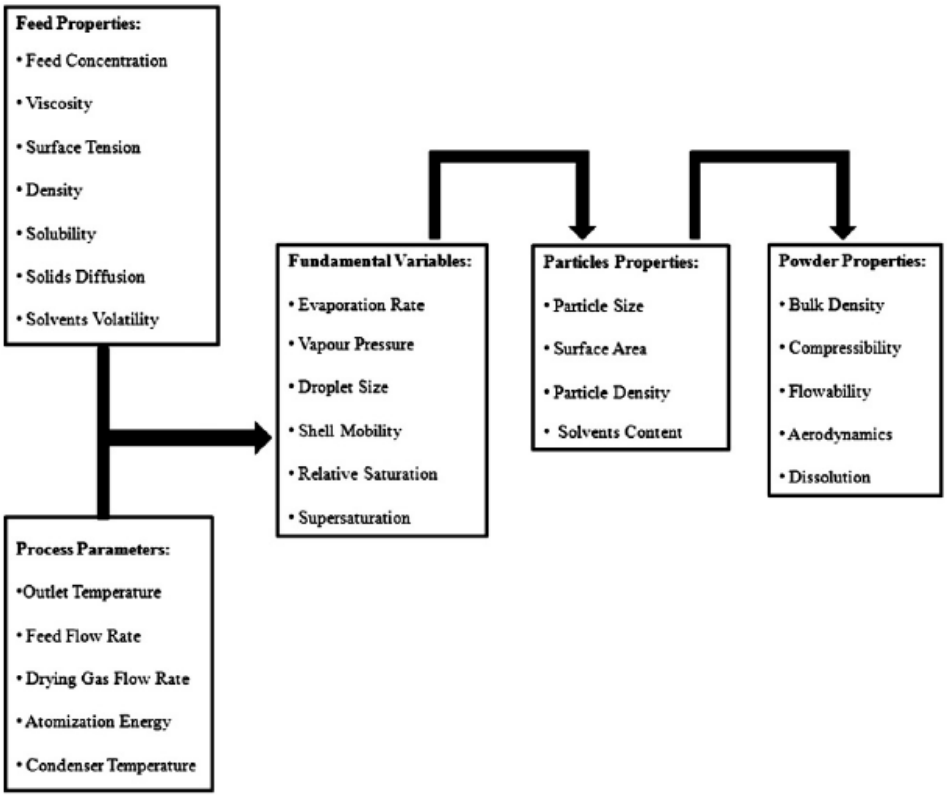

Fig. II 3.3 The schematic[113] outlining the various factors affecting the spray drying process. This explanation is valid for both the simple evaporation of solvent from an already created solid and the actual creation of a solid from solution. These are two separate processes.

The outline above is a result of massive experimentation by the authors. Their work is replete with SEM photomicrographs of varying particle sizes and morphologies as a result of varying the three major parameters.

Mezhericher, Levy and Burde[114] authored a review paper in 2010 that summarized the theoretical models of single droplet drying kinetics. What is especially noteworthy about this contribution to the literature is the compilation and explanation of various boundary conditions and assumptions necessary to solve the material and energy balance equations. In addition, the authors attempted to correlate results obtained from CFD simulations with analytical and

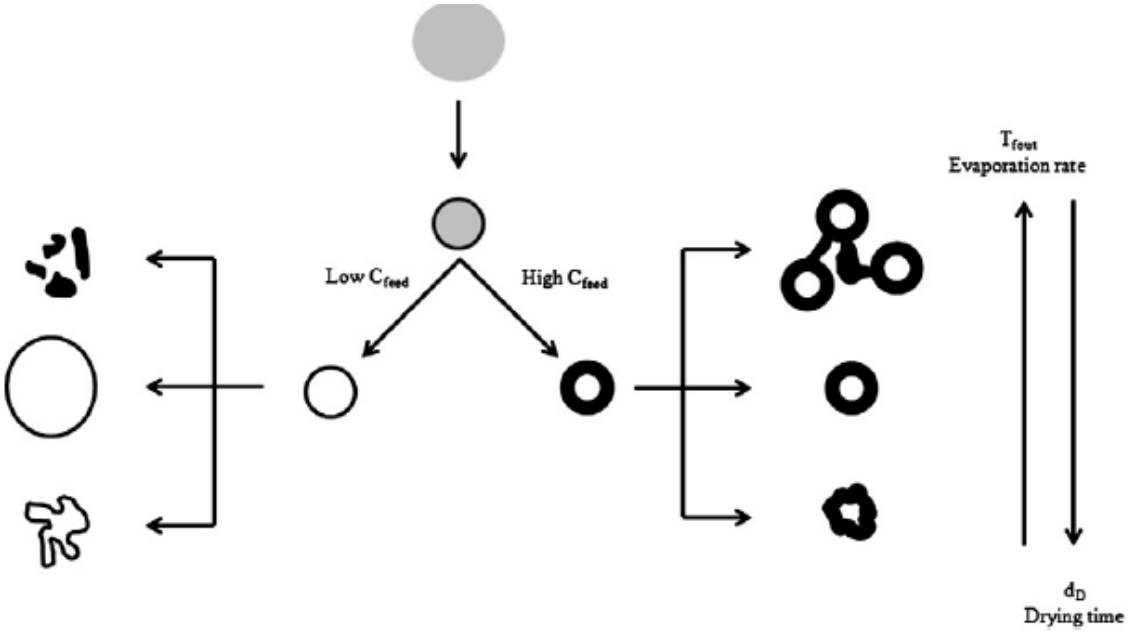

Fig. II 3.4 Notice how three parameters T, c_f, and d_D affect the size and morphology of the resulting particle. This schematic is a rationalization and simplification of the many factors involved in spray drying[113]. Particles are shriveled at slow drying times and low temperatures. The optimum shape is the sphere.

numerical solutions to the equations of change. The goal of any analysis is the prediction of size and shape of the particle.

Perhaps one of the best of the papers reviewed by the author of this dissertation was written in 2009, by Dobry *et al*[116]. It was posited that though spray drying had long

been a prominent unit operation in the pharmaceutical industry it was only after extensive pilot plant testing and statistical analysis of the product attributes could an industrial-scale process be constructed. Two specific but important control volumes are identified within the spray drying chamber and the thermodynamics therein investigated. The goal was through the use of fundamental models a quick definition of a complete process could be delineated. The *macroscopic control volume* encompasses the entire spray drying chamber. The *microscopic control volume* is enclosed in the macroscopic control volume[116]. **Fig II 3.5** below is a beautifully descriptive schematic of the process.

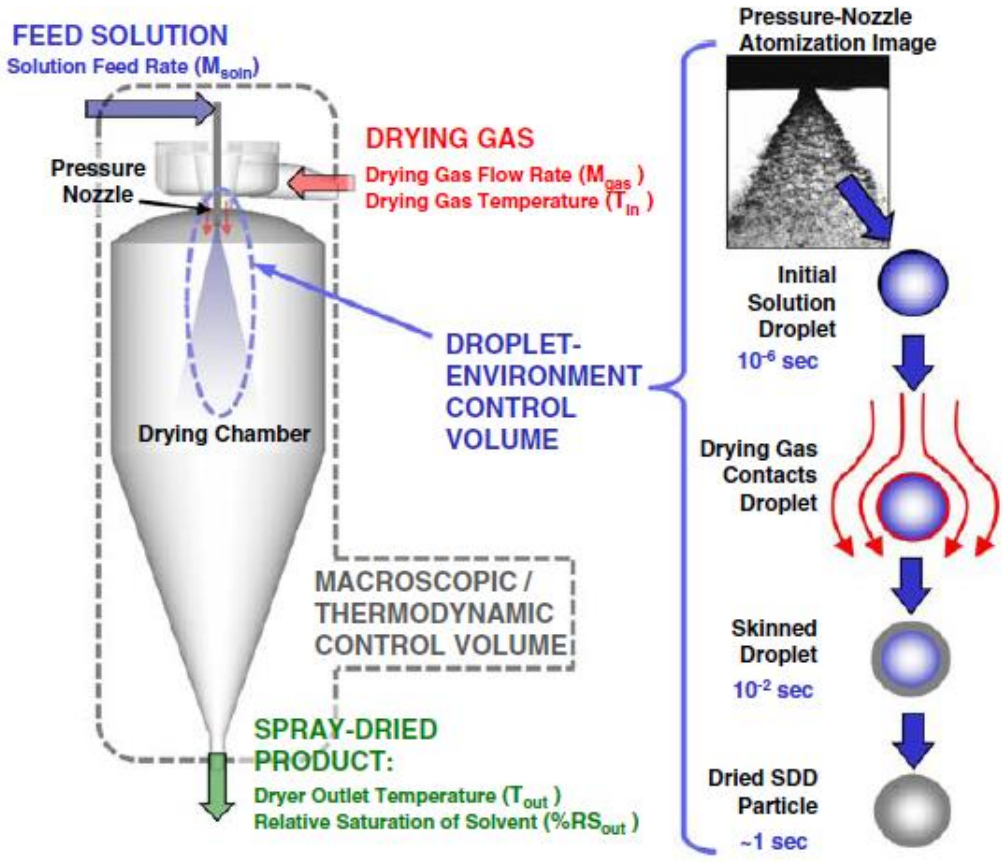

Fig II 3.5 Two separate control volumes are depicted in this schematic of the spray drying process. Notice the time scale delineated on the right side of the drawing[116]. The control volumes permit the use of thermodynamics to aid in the construction of a process.

For spray drying, the key thermodynamic process parameters are[116]:

1. M_{soln}: The mass flow rate of the feed.
2. M_{gas}: The drying gas flow
97
3. T_{in} and T_{out}
4. % RS_{out}: The relative saturation (humidity) at the spray dryer outlet.

The energy require to vaporize the solvent is[116]:

$$\Delta E = M_{soln} \times (1 - x_{solids}) \times \Delta H_{vap} \quad \text{(II 29)}$$

where x_{solids} is the mass fraction of solids in the solution.

The energy lost by the drying gas is:

$$\Delta E = M_{gas} \times c_p \times (T_{in} - T_{out}) \quad \text{(II 30)}$$

This is an example of energy 'out' and energy 'in' assuming a well insulated drying chamber and no loss of heat to the surroundings.

$$T_{out} = f(M_{soln}, M_{gas}, T_{in}) \quad \text{(II 31)}$$

The thermodynamic process parameters can thus be determined[116].

$$T_{out} = T_{in} - \frac{M_{soln} \times (1 - x_{solids}) \times \Delta H_{vap}}{M_{gas} \times c_p} \quad \text{(II 32)}$$

$$\%RS_{out} = 100 \times \left(\frac{P_{chamber}}{P^*_{T_{out}}}\right) \times \frac{M_{soln}(1 - x_{solids})/MW_{solvent}}{[M_{soln}(1 - x_{solids})/MW_{solvent} + M_{gas}/MW_{gas}]} \quad \text{(II 33)}$$

where $P_{chamber}$ is the total pressure in the spray drying chamber and P^{*}_{Tout} is the vapor pressure of the feed solvent at the outlet conditions[116]. Thus to summarize the design of a feasible spray drying process not only must the drying kinetics of the single droplet be considered but also the thermodynamic totality.

Maximum T_{out} might be determined by the sensitivity of the dried product to degradation by excessive heat. Maximum T_{in} would be determined from T_{out} and perhaps a minimum specific drying ratio M_{soln} / M_{gas} to insure economical process throughput[116].

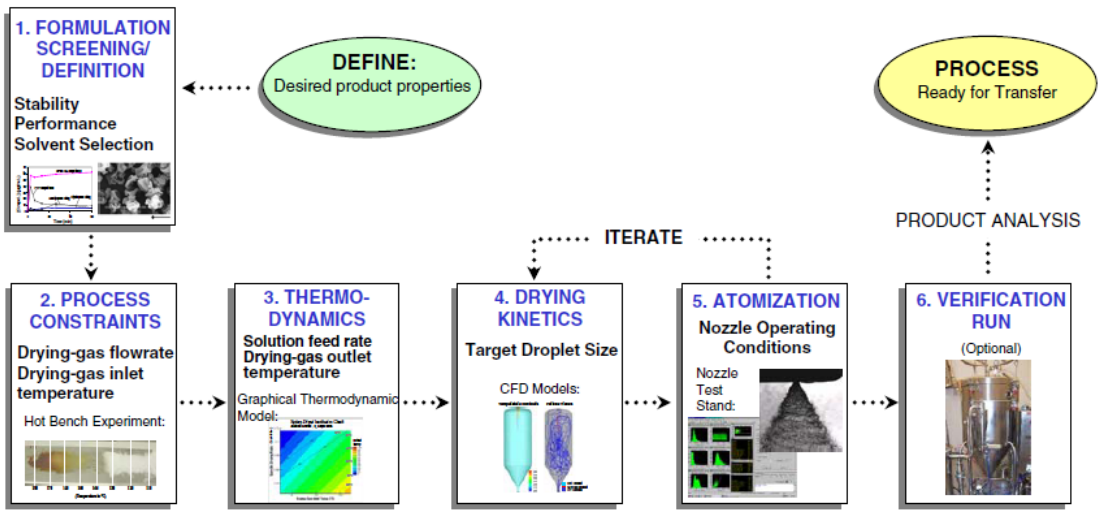

Fig II 3.6 Presented above is a schematic of a rationalized approach to the design of a commercial spray drying process. Note that there does exist a need for simulation studies (CFD) to approximate the product droplet size and thus the choice of atomizing nozzle[116].

Thus the development of a commercial spray drying process is dependent on fundamentals (thermodynamics), single-droplet drying kinetics, simulations (CFD), and state-of-the-art process characterization.

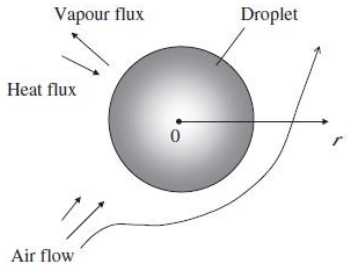

Fig II 3.7 A concise diagram displaying some elements present during spray drying[117]. The forced convection is governed by correlations for the Nusselt, Sherwood, and Schmidt numbers.

III

EXPERIMETATION

1. The production of ZIF-8

Prior to the publication of this tract the production of ZIF-8 has only been accomplished on a laboratory scale. The addition of 2.4 grams of zinc nitrate hexahydrate to 45.2 grams of methanol resulted in a solution that was combined with a solution of 5.28 grams of methylimidazole in 44.0 grams of methanol. The resulting mixture was stirred for up to 1 hour. The **zinc imidazolate framework**, ZIF-8 was captured as product after the mother-liquor was decanted off subsequent to 2-3 washings and centrifugations. The yield was approximately ¼ gram. There was substantial waste of methanol. As part of this dissertation it was proposed to attempt a more efficient and expanded method of production. It was decided to produce ZIF-8 by two different pathways; first via a continuous process using a **continuous stirred-tank reactor** (CSTR) and secondly via a **batch process**.

Venna *et al*[47,49] deduced important characteristics concerning the kinetics of crystallization and structure of ZIF-8. The diagram on the next page **Fig. III 1.1**, is a representation of ZIF-8 production. This particular organization is known as Avrami kinetics. The most important sector to consider here is region II where the bulk of

formation occurs; 12 to 60 minutes. The shape of this particular graph and its mathematical formulation hints at a sigmoid or Gaussian. When designing the CSTR is it necessary to include the $y=1-exp(-kt^n)$ mathematical expression when determining the reaction rate? No, region II can be approximated as a straight line with a slope of 6 units of % crystallinity per minute. The ideal reactor residence time τ, would be about between 20 and 40 minutes. The space velocity is the reciprocal of the residence time.

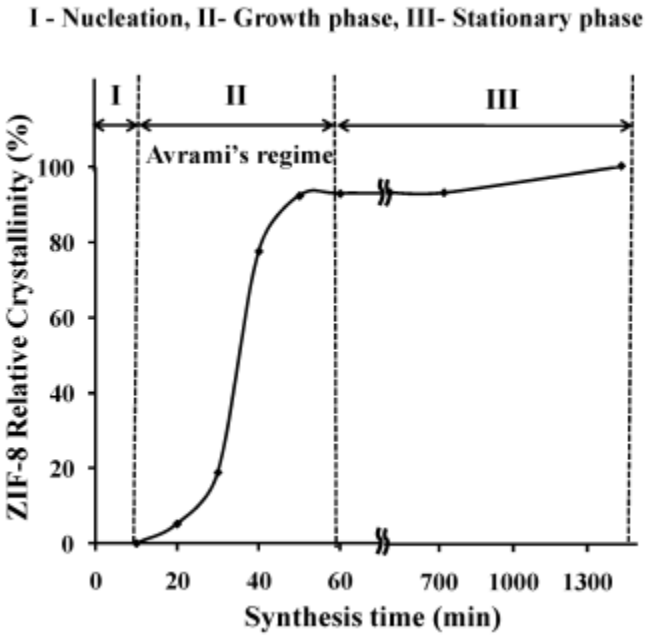

Fig. III 1.1 Venna's[47,49] use of Avrami's kinetics to describe the formation of ZIF-8 (cf. **Fig I 2.4**). For the purpose of reactor design only region II need be considered and the formation of product approximated as a first order reaction.

To date, no heat effects have been realized during this synthesis and thus this reaction is considered to be isothermal. The reactor design and start-up is relatively easy. The performance equation for the CSTR is:

$$V / F_A = X_A / -r_A \quad \text{(III.1)}$$

Where V is the reactor volume, F_A is the flow rate of component A, X_A is the conversion of component A, and r_A is the reaction rate of component A.

The *residence time* τ, is the average amount of time a discrete quantity of reagent spends inside the tank. Along with the performance equation (III.1), the design of the CSTR cam be accomplished by realizing:

$$\tau = V / F_A \quad \text{(III.2)}$$

In a chemical process the reactor may not always be limiting operation and thus the volume of the reactor can be sized accordingly. F_A is the flow rate of the product in liters/minute. For most first order reactions the time to reach steady state in the CSTR is 3 to 4 times τ. The reactor was sized at 1.0 liter capacity and it was decided to use only 85% 0f the total volume. With a residence time of 30 minutes, the total flow rate is 0.02833 liters/minute. This is split between two mixing tanks. The first contains 52. 8 grams of methylimidazole with 440 grams of methanol. The second contains 24 grams of zinc nitrate hexahydrate and 452 grams of methanol. To provide for adequate time to reach steady state the total flow rate to the CSTR was reduced to 0.0094 liters per minute. After 90 minutes, about 3 to 4 times the residence time, the reactor was assumed to have reached steady state and product from the CSTR was released and captured in another vessel. The total product obtained measured 1210 ml. It took approximately 8 hours to decant off the mother liquor and harvest the wet ZIF-8 crystals. The yield was 12.0 grams of ZIF-8 after drying at 70° C (cf. **Fig. I 4.2)**. This yield while better than the typical laboratory synthesis is still not economically viable from a production standpoint. The X-ray diffraction pattern (XRD) is the ‘crystalline’ fingerprint for ZIF-8 and we use the

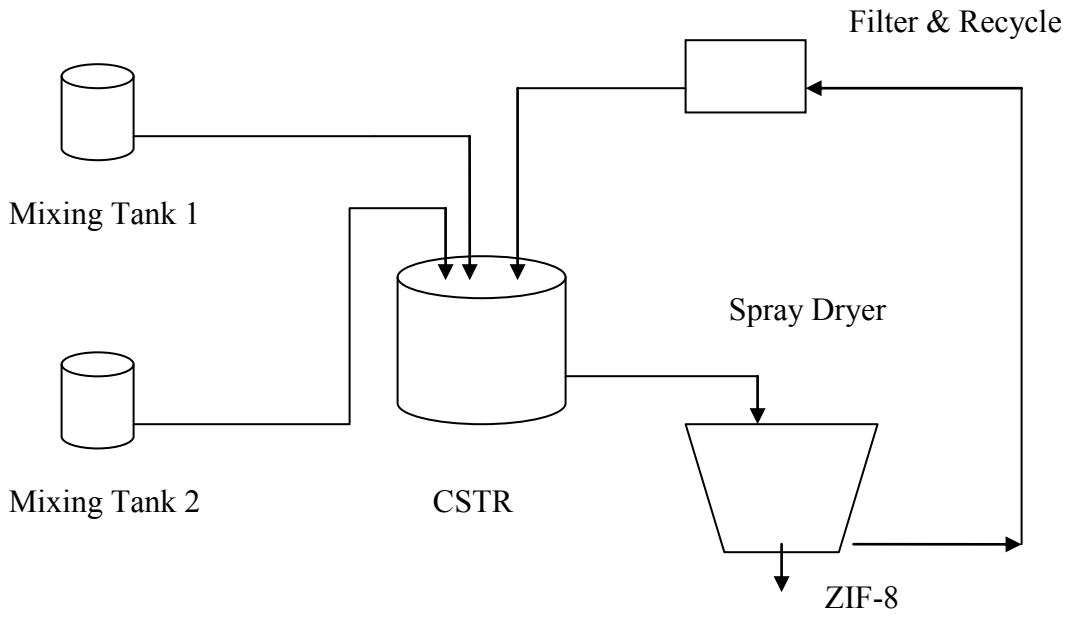

Fig. III 1.2 A continuous process to produce ZIF-8 nanoparticles at room temperature. Mixing tank 1 consists of methanol and zinc nitrate hexahydrate. Mixing Tank 2 consists of methanol and 2-methylimidazole. Nitrogen at 1.25 atm. pressure must be pumped into all of the vessels to displace oxygen and prevent fire. It is proposed to insert an additional separation via nanopore filtration to capture any stray product and recycle the methanol. The Buchi B2909 spray dryer facilitates the recapture of solvents under a nitrogen blanket and can process 1 liter per hour of slurry.

results obtained by Venna[47,49] as our template. The first XRD pattern obtained was highly irregular and bore no resemblance to the standard. The results are displayed in **Fig. III 1.3, Fig. III 1.4** and **Fig. III 1.5**. The first chart displays the classical XRD pattern generated by ZIF-8 while the second shows a raw ZIF-8 sample obtained from the CSTR with no washing and little drying. The original scheme was to have the product from the CSTR enter the spray dryer immediately.

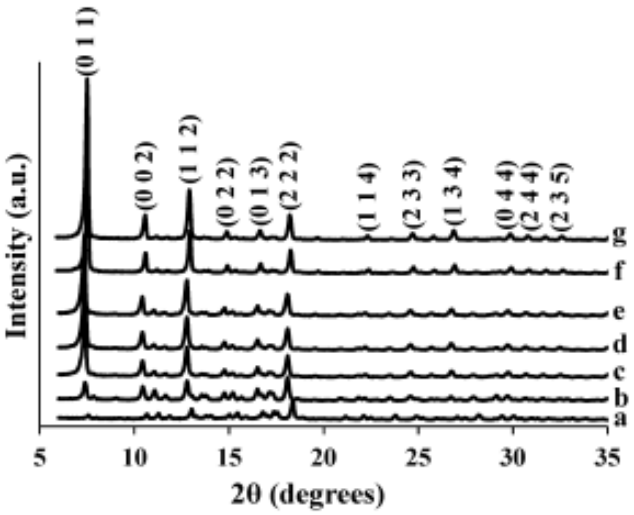

Fig. III 1.3 The XRD pattern generated by ZIF-8 as it progresses through time from a) 12 minutes through g) 24 hours. This chart was obtained after numerous washings and centrifugations, (3) with drying at 70° C for 24 hours[47,49].

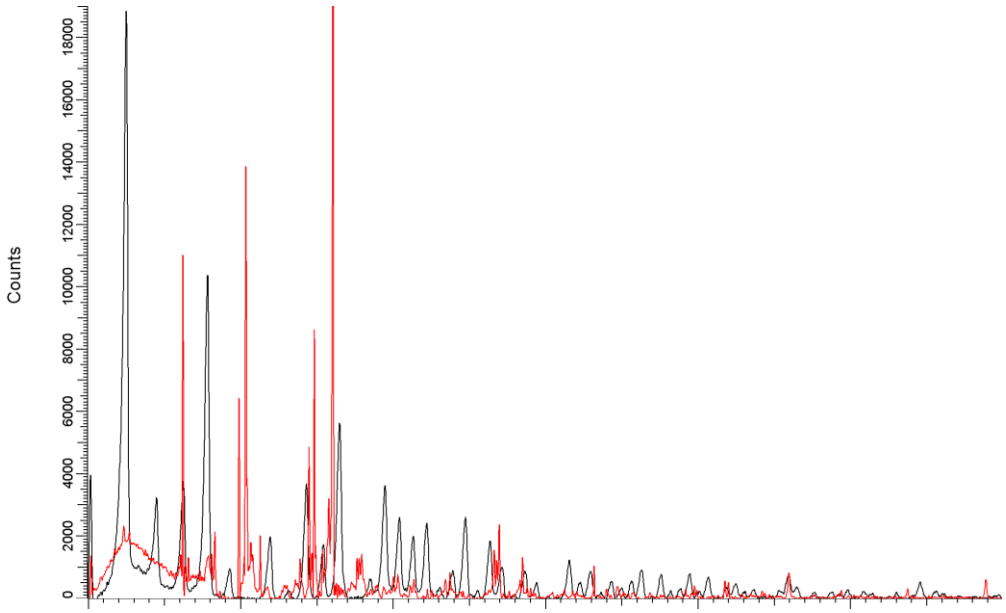

Fig. III 1.4 This XRD pattern is a composite of 2 samples obtained from the CSTR process with no washing and minimal drying. At first appearance it seems that the product is not ZIF-8.

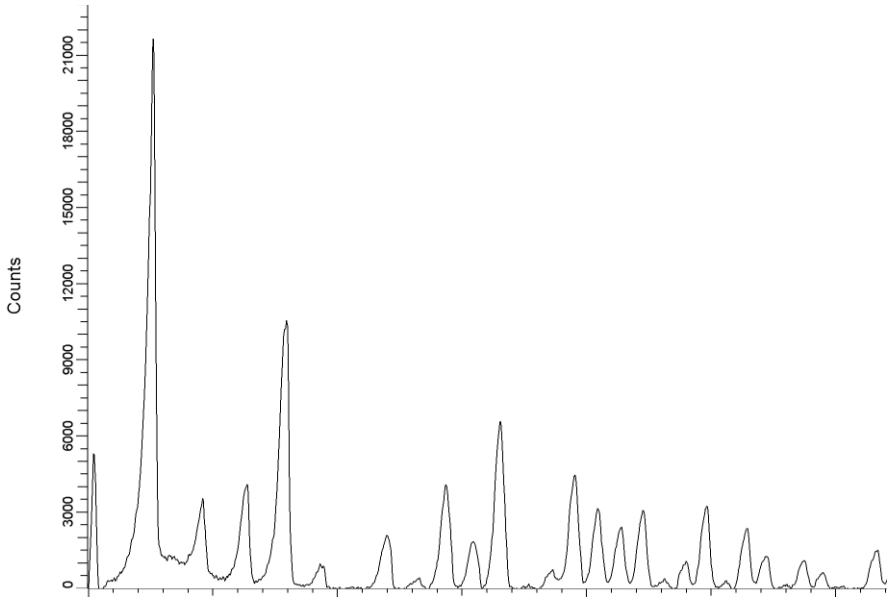

Fig. III 1.5 This is the CSTR product after 2 washings and centrifugations with drying. At 70° C for 24 hrs. The XRD scale is shifted from **Fig. III 1.3** yet shows the characteristic peaks of ZIF-8. This sample would probably need more drying time. The massive surface area and intrinsic polarity of ZIF-8 makes this MOF capable of grabbing any impurities into its cage-like structure.

While the XRD is the definitive fingerprint, two other analytical tests help solidify the characterization of a crystalline product; the Brunauer-Emmett-Teller (BET) surface area and a scanning electron micrograph (SEM). As a template for comparison we use the results of the solvosynthesis generated by Pan *et al*[126] from 2011. His group used a synthetic route much like Venna[47,49] and provided BET isotherms and SEM photos of their product. Unlike the work presented in this dissertation, their work was done on a laboratory scale.

The BET surface area test was carried out on a micromeritics Tristar 3000 porosimeter using liquid nitrogen as a coolant. The synthesized ZIF-8 was degassed at 160°C for 160 minutes. The single point surface area ($P/P_0 = 0.314$) was 1302 m^2 g^{-1}. The BET and

Langmuir surface areas for a ZIF-8 studied in literature[126] are 1079 and 1173 m^2 g^{-1}, respectively. These surface areas are comparable and within a similar range. The plots for the isotherms of the experimental and literature ZIF-8 can be seen in **Fig. III 1.6** and **Fig. III 1.7**, respectively. These two isotherms have a similar shape, even though the amount adsorbed in Pan's sample is almost twice that of the experimental sample.

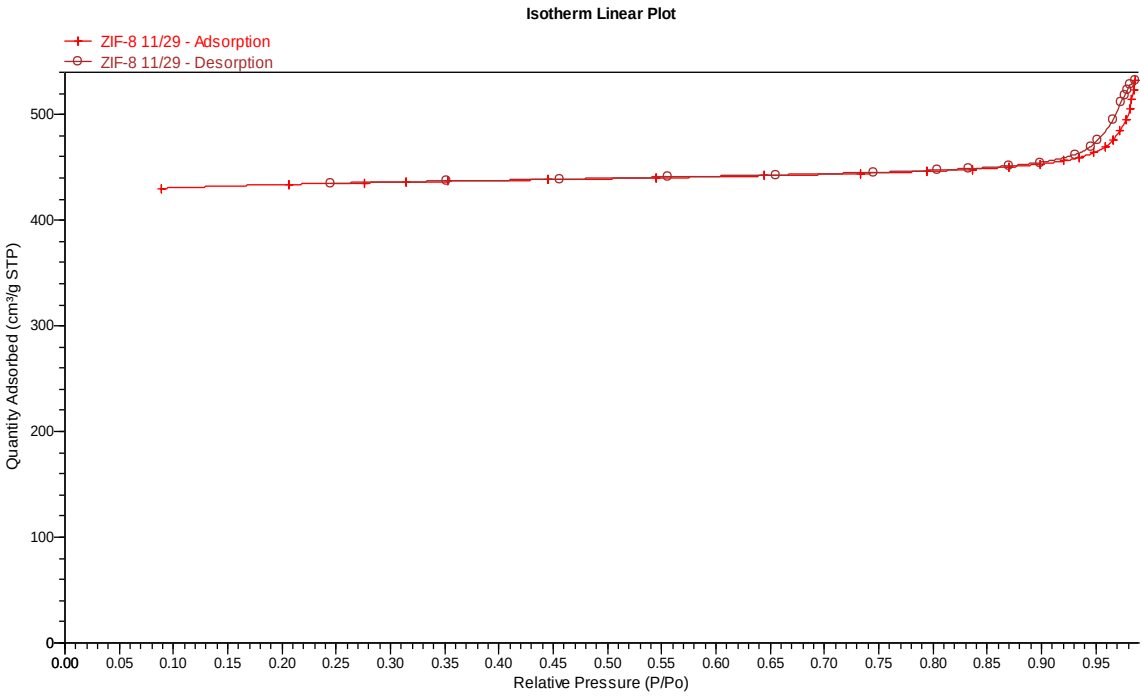

Fig. III 1.6 The Brunauer-Emmett-Teller (BET) plot of a ZIF-8 sample harvested from the solvosynthetic reaction within the CSTR designed for this dissertation. Compare this chart with the one generated by Pan's group, **Fig. III 1.7**[126]

The results for this test carried out in the Materials Characterization Laboratory at the University of Louisville are postulated on Langmuir and BET adsorption theory. This is briefly explained in **Part I**. It was thought that perhaps a 5-point BET analysis might provide more insight into the total surface area of the crstalline ZIF-8 product and plans were made to generate this test.

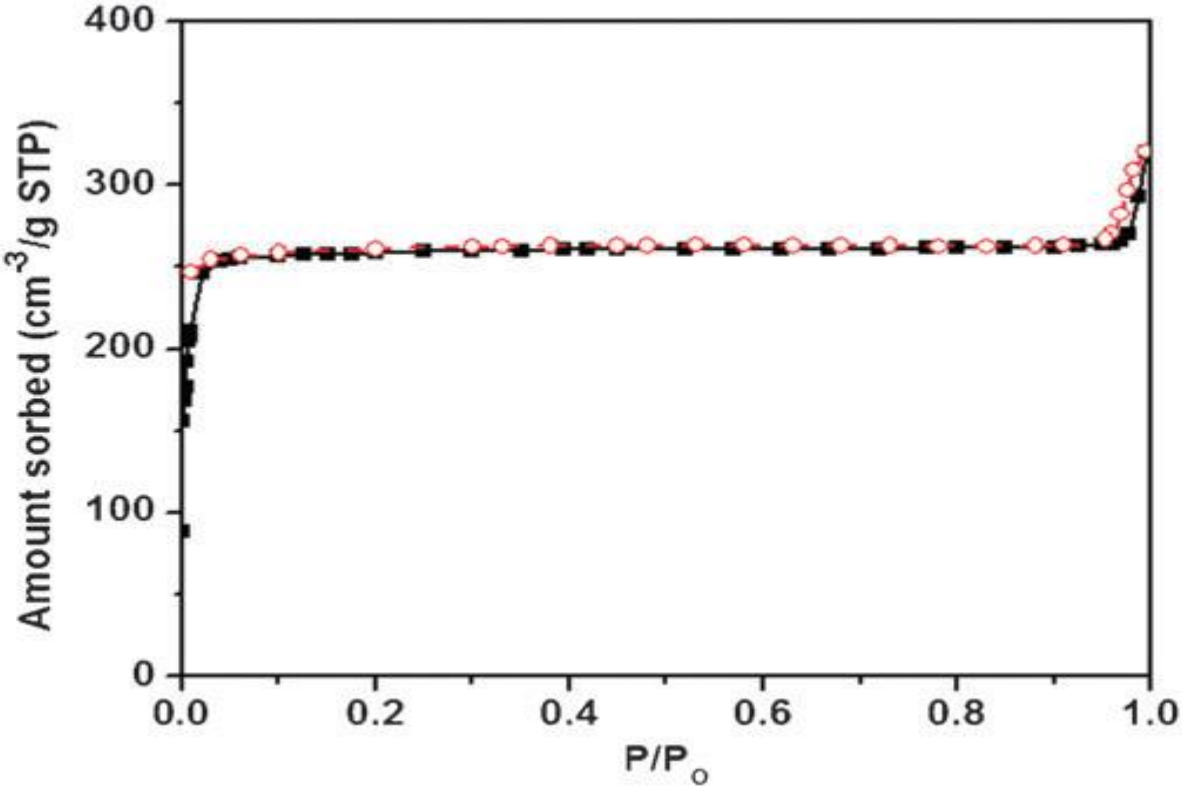

Fig. III 1.7 Here is the BET isotherm generated by the product of a solvosynthesis completed in the laboratories of Pan *et al*[126]. Notice that half of the amount of nitrogen gas has been adsorbed in this ZIF-8 sample.

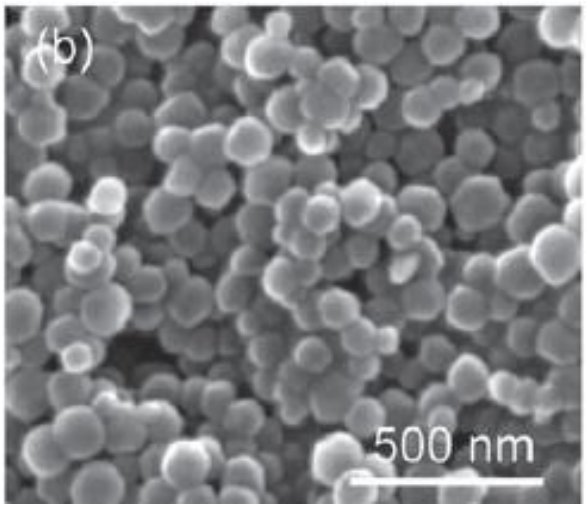

Fig. III 1.8 SEM micrographs of ZIF-8 generated by Pan's lab group. It appears the spherical particles are less than 100 nm in size; a true nanoparticle[126].

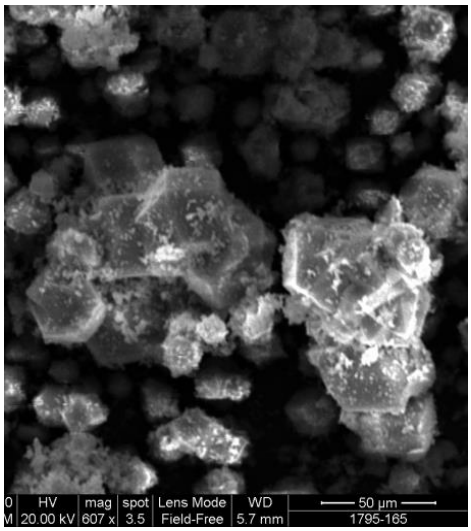

Fig. III 1.9 SEM micrographs generated via the product of the CSTR solvosynthesis in this dissertation. The particles are not spherical and more that 100 µm in size. The increased nitrogen adsorption (double) might now be understood. The size of these ZIF-8 crystals qualifies them as *macroparticles.*

In an attempt to predict future reaction histories with the CSTR designed for this dissertation, it was decided to model the process in Simulink, The MATLAB simulation module. The models prepared were done in the most generic and flexible of fashions.

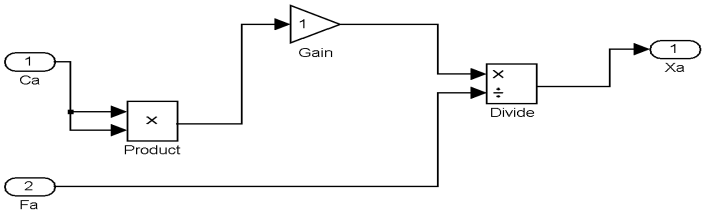

Fig. III 1.10 This is the Simulink configuration of the CSTR performance equation (III.1). The flow rate F_a can be adjusted along with the concentration C_a [127].

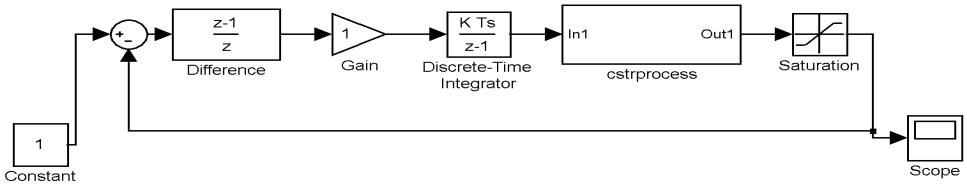

Fig. III 1.11 Here is the actual Simulink model of the process to make ZIF-8. The CSTR process from **Fig. III 1.10** is inserted above as a subsystem. It was decided to insert a discrete-time integrator rather than a continuous model: most often the data for the reaction will come in the form of chart of values compiled from conductivity or concentration measurements[127].

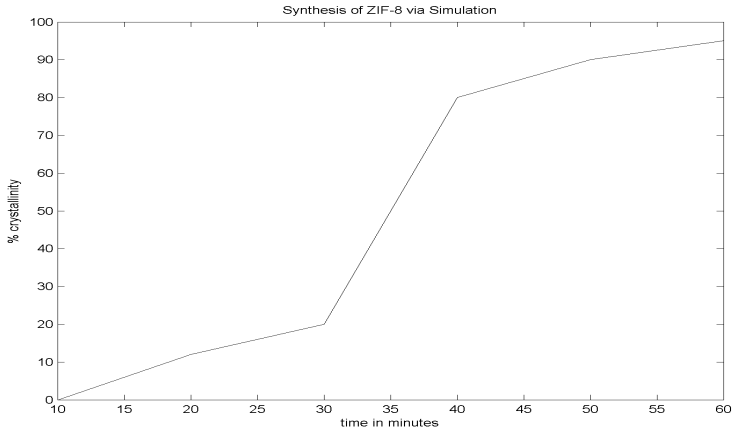

Fig. III 1.12 Output of the Simulink/Matlab program for CSTR production of ZIF-8. A set of difference equations modeled the reactor behavior. This would be similar to the use of a collection of data points generated by conductivity or concentration measurements.

I traveled to the Research Laboratories of the Buchi Corporation in Wilmington, Delaware in March of 2014 to conduct tests on the Mini B-290 Spray Dryer with the hopes of improving process yield and efficiency. These tests comprised the **batch process** aspect of the synthesis. The B290 Spray Dryer is capable of about 1000 ml of throughput per hour. The process reagents were prepared in the same manner as for the CSTR process. The reactants were split between two mixing tanks. The first contained 52. 8 grams of methylimidazole with 440 grams of methanol. The second contained 24 grams of zinc nitrate hexahydrate and 452 grams of methanol. This consisted of a total of about 1200 ml. The first batch process was permitted to react for 20 minutes before being submitted to the spray drying process. The ZIF-8 product obtained from this separation operation measured 44.53 grams and more importantly 1050 ml of methanol was recovered. The flow rate of ZIF-8/methanol slurry through the dryer was recorded at 20 ml/min. with the N_2 drying flow rate recorded at 40 mm/min. The nitrogen temperature was maintained between 90 and 100º C. It was presumed that a portion of the methanol mother liquor remained occluded within the ZIF-8 cage with the rest mixing with the drying agent and vented to the fume hood. The nitrogen gas was used as a drying agent due to the flammability of methanol and the total process lasted 1.5 hours.

A second batch was run with a reaction time of 40 minutes before submission to the spray drying process. This time 40.20 grams of ZIF-8 product was harvested along with 1015 ml of methanol. This process lasted 1.75 hours. In a little more than 3 hours, 84.73 grams of ZIF-8 was produced and almost 85% of the methanol mother liquor recovered. This amount 84.73 grams of ZIF-8 would have taken about 170 days to make in the

laboratory at 0.5 grams per day. The samples were to be submitted to testing for verification of product.

Powder X-ray diffraction was first investigated, using a Bruker D8-Discover Diffractometer in the Materials Characterization Laboratories at the University of Louisville . The XRD pattern for the ZIF-8 material experimentally synthesized is shown in **Fig. III 1.13**.

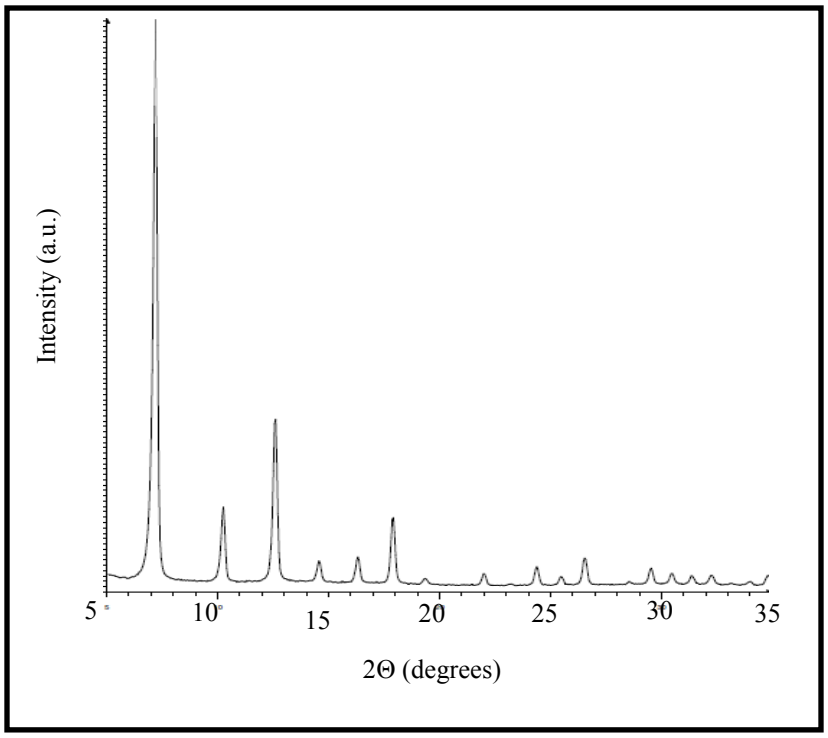

Fig. III 1.13 This is the powder XRD pattern generated by the ZIF-8 product produced during the 20 minute batch process and then submitted to the Buchi Mini 290 Spray Dryer. Compare this with the pattern generated by the laboratory synthesis of Venna *et al* **Fig. III 1. 3** This product was dried in an oven at 70º C for 24 hours.

The ZIF-8 product was submitted to the Particle Technology Laboratory of Downers Grove Illinois for 5-point BET determination as a conclusive proof of product. This particular laboratory uses strict ASTM procedures for property determination. The Micrometrics Tristar II Surface Area and Porosity system was used to generate BET

surface plot according to the ASTM 3663-99 (Appendix) protocol. The plot is shown in **Fig. III 1.14**.

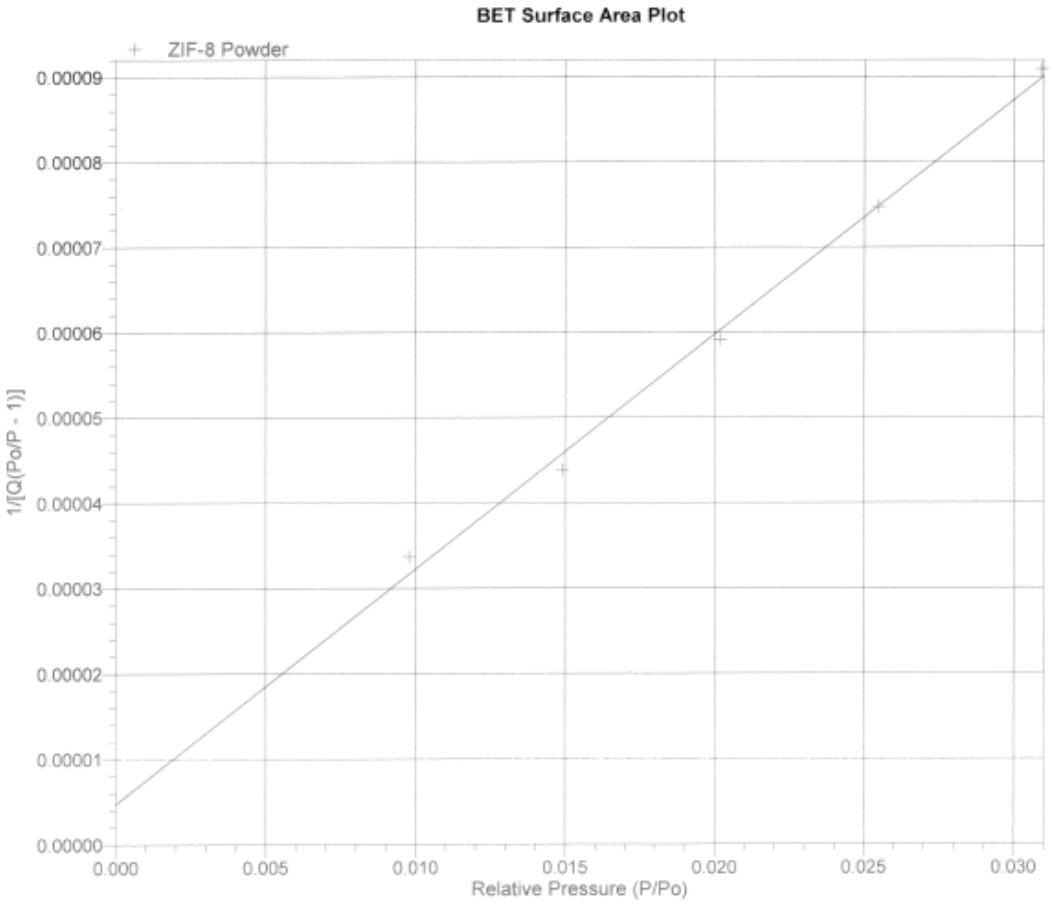

Fig. III 1.14 Here is the 5-point BET plot generated by the ZIF-8 sample from the 20 minute batch reaction. This analysis yielded a BET surface area of 1578 m^2 / gram ± 63.08 m^2 / gram. This area compares favorably with the 1302 m^2 / gram generated via the single point method. The size of the particles produced by the spray drying process was approximately 13.0 microns.

The Buchi corporation has always claimed that the Mini 290 was capable of high throughput with controlled particle size. The batch process along with the spray dryer (and an additional tray-drying sequence) seems to produce an acceptable ZIF-8 product. It remains to be seen whether the CSTR product would be improved by passing it through the spray dryer. As of now, the CSTR product is barely acceptable.

2. The Properties of ZIF-8

Before any engineering work and heat transfer analysis could be done it was necessary to determine important physical properties of ZIF-8 which had yet to be published. It was naïve of this author to think that density of the cage-like ZIF-8 could be measured with a pycnometer. I traveled to Particle Technology Laboratory in Downers Grove IL to make use of their Micrometrics AccuPyc II which uses the ASTM B-293-10 method of helium gas pycnometry to determine density. Helium, a quantum gas, is small enough to penetrate the pores of ZIF-8. The results for the ZIF-8 samples from both the continuous and batch processes were similar. After 10 separate measurements:

The volume **V**, of ZIF-8 sample was 0.2263 cm^2 ± 0.0002 cm^2.

The density **ρ**, of ZIF-8 sample was 1.4902 g/cm^3 ± 0.0015 g/cm^3.

The ASTM procedure is included in the Appendices.

The determination of thermal conductivity **k**, proved to be a problem. The test apparatus at the University of Louisville could not provide accurate and repeatable results. I traveled to the laboratories of Dynelyn in Easton, PA to observe determination of thermal conductivity via ASTM D5470 (Appendices). This used a simple but accurate test chamber and the formation of a tightly controlled sample size to determine thermal conductivity. The sample was measured 5 different times using 5 different samples.

The thermal conductivity **k**, measured 0.113 W/m K.

It is interesting to compare the test results with those of the molecular simulation conducted by Zhang[110] which reported a **k** of 0.165 W/m K. This is an error of 46%.

Molecular simulations that do not provide result within 5% of the true value are worthless.

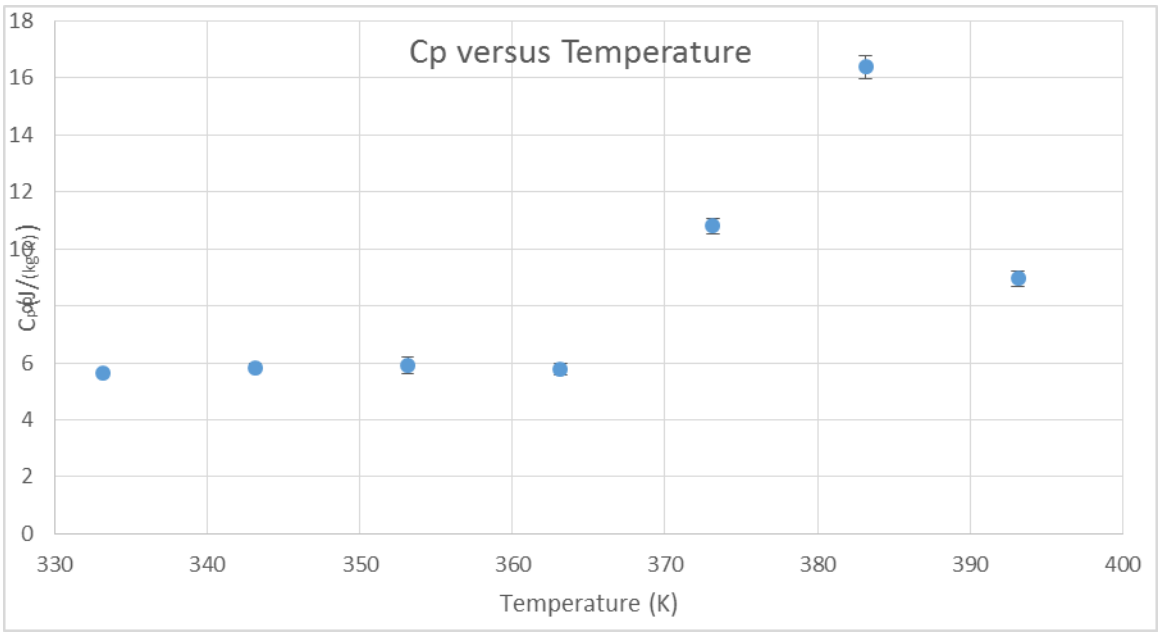

Fig. III 2.1 This a plot of the specific heat of ZIF-8 conducted according to the test method of Max Slaton which is compiled in the Appendices. This test was repeated 25 times. Notice how small the error bars are.

The specific heat of ZIF-8 was determined in the Materials Characterization Laboratories at the University of Louisville. Really, only a small portion of the ZIF-8 specific heat contributes to the calculation of the nanofluid heat capacity: the volume fractions of microparticle in the base fluid are minute.

3. ZIF-8 as a Heat Transfer Agent

Systematic error in laboratory experimentation is only evident once it is found. This was particularly manifested with measurements taken from the heat transfer rig in the Heat Transfer Laboratory at the University of Louisville.

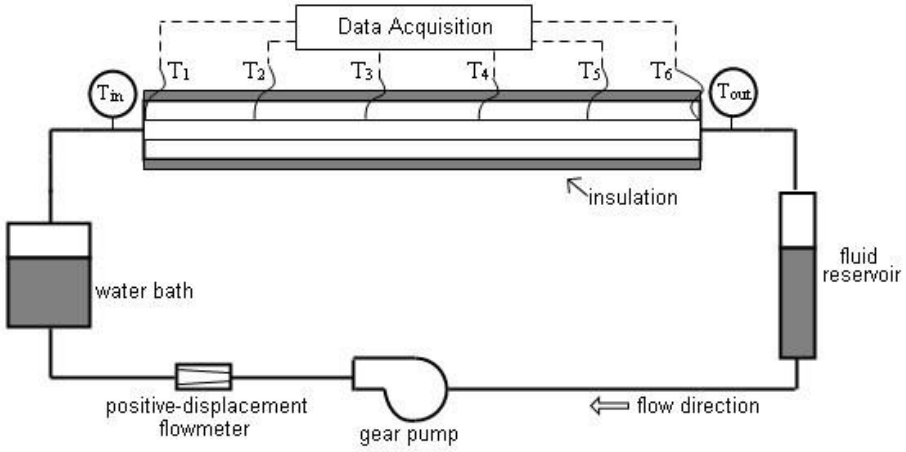

Fig. III 3.1 The heat transfer rig used for nanofluid studies at the University of Louisville. After a laboratory accident in October 2014, the rig was dismantled, refurbished and re-assembled. During this process it was found that some of the thermocouple connections (T_1- T_6), were faulty thus leading to incorrect measurements. This discovery has led to the establishment of a baseline test for rig integrity. The baseline standard shall be Amsoil 0 wt Synthetic Motor Oil.

Heat transfer coefficients of prepared base/nanofluids were measured using a lab-built test rig. A schematic of heat transfer test rig is shown in **Fig. III 3.1**. The entire system is made from ¼ inch stock copper tubing and fittings. In the flow system, a copper pipe serves as a reservoir for the nanofluids and is capable of holding 2 liters of fluid. The fluid flows from the reservoir through a variable speed gear pump (Grainger 6NY97). The gear pump is sized to cover a wide range of flowrates up to 4.8 gal/min. Based on the properties of the nanofluid, particularly viscosity, the pump will cover a Re range from 50 to 7000. Flowrates are measured using an inline flowmeter connected to an electronic

readout. From here the fluid flows through a copper coil held in a hot water bath which can maintain the test fluid from room temperature up to 96°C. The fluid then enters the heat exchange section. There are two thermocouples placed in the fluid at both the inlet and outlet of this section. The section itself is formed form ¼ inch high thermal conductivity copper refrigerator tubing. Six type-T thermocouples are attached equidistant along the exterior of the copper tube in this section. The entire heat exchange section is wrapped in heat tape which provides a constant heat flux to the fluid. Two layers of insulation are wrapped around the heating tape to ensure low heat loses within the heat exchange section. Temperatures are monitored in real time using a Labview program designed for the system. The program also provides real time calculation of the heat transfer coefficient based on the fluid properties and flowrates. By altering the control variables; heating power, inlet fluid temperature, and fluid flow rate, a series of tests were conducted to determine the heat transfer coefficients of base/nanofluids. The ratio of heat transfer coefficient of nanofluid **h**, to base fluid $\mathbf{h_o}$, was calculated to determine if there was any enhancement $\mathbf{h/\ h_o}$. In an effort to reduce experimental bias, the flow rates were adjusted in a non-linear manner.

Three samples of the Amsoil / ZIF-8 were prepared in the following manner. The ZIF-8 sample was mixed with PAO oil at 0.50, 1.0, and 2.0 wt % using a Model 500 Sonic Dismembrator from Fisher Scientific that is able to deliver up to 400 watts of power. Dodecanethiol at 0.1 wt% was used as a surfactant to help stabilize fluid suspension. Each sample was sonicated for 20min. All the samples were left to sit for 48 hours after sonicating and shaken well before further testing. Viscosity measurements of the mixtures were taken to insure Newtonian fluid behavior.

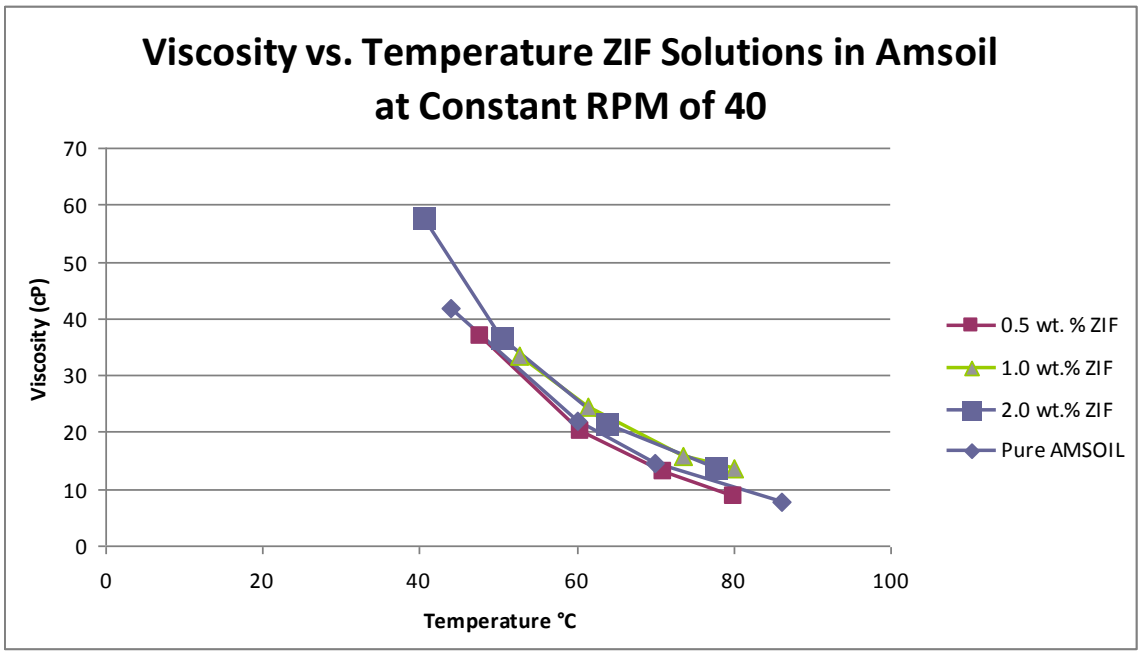

Fig. III 3.2 Viscosity measurements of the ZIF-8 / Amsoil mixtures. This behavior is reminiscent of Newtonian fluid behavior. Also it is important to note these measurements are consistent with Amsoil data sheets.

It was hoped that the massive surface area of ZIF-8 would afford enhanced heat transfer; heat transfer is all-about surface area. In comparison the surface area of 10nm copper surface area is approximately 10 m^2 / gram. The surface area of our ZIF-8 molecule is about 1400 m^2 / gram; 140 times the difference. Unfortunately the thermal conductivity of ZIF-8 is only 0.113 W/m K which when compared to copper is about 850 times less. Is there a possibility of increased *phonon effect* due to the size of the molecule? The accompanying Excel spreadsheets on the following pages reveal that in fact the ZIF-8 molecule fails miserably as a heat transfer agent. The molecule is more 'organic' than 'metallic'. Since Therminol 66 is so expensive, no further testing was done with this as a base oil. No further data analysis was necessary.

Fluid	.5 wt.% ZIF in Amsoil					.5 wt.% ZIF in Amsoil					.5 wt.% ZIF in Amsoil				
Power	60%					60%					60%				
Temp Set	41.9°C					62.4°C					82.1°C				
Water Bath	41.9	41.9	41.9	41.9	41.9	62.4	62.4	62.4	62.4	62.4	82.1	82.1	82.1	82.1	82.1
Flow (ml/s)	10	20	30	40	60	10	20	30	40	60	10	20	30	40	60
inlet	43.107	44.544	41.137	45.92	47.213	59.78	60.701	61.885	62.289	63.225	78.203	80.334	80.791	81.156	81.611
1	55.57	55.46	55.29	55.51	56.26	72.48	71.51	71.54	71.16	71.54	90	90.3	89.5	89.32	89.41
2	70.93	65.66	64.05	63.28	63.51	87.93	81.49	79.74	78.79	78.2	104.3	99.68	97.64	96.41	95.36
3	77.18	68.77	66.21	64.76	64.12	94.07	84.69	81.38	79.4	78.06	110.1	102.4	98.3	96.42	94.96
4	84.7	78.59	71.91	69.33	67.93	100.4	90.31	85.03	82.73	81.69	115.2	105.7	101.3	99.58	98.59
5	87.06	78.11	74.64	72.23	70.79	101.7	93.28	88.2	85.67	84.29	116.3	108.8	104.2	102.2	100
6	87.77	79.62	76.23	74.05	71.67	101.5	94.33	89.43	86.06	84.54	116.2	109.8	104.3	102.2	100.9
outlet	61.211	54.23	51.262	49.971	49.997	77.008	68.611	65.869	61.095	65.303	92.037	85.354	84.06	83.374	83.178
density	853.4	853.4	853.4	853.4	853.4	853.4	853.4	853.4	853.4	853.4	853.4	853.4	853.4	853.4	853.4
viscosity (cP)	0.04673	0.044538	0.042017	0.043398	0.043919	0.027143	0.024187	0.023571	0.021843	0.023877	0.009211	0.007411	0.00708	0.006953	0.007055
specific heat	2050	2050	2050	2050	2050	2120	2120	2120	2120	2120	2220	2220	2220	2220	2220
therm cond	0.151261	0.151261	0.151261	0.151261	0.151261	0.151261	0.151261	0.151261	0.151261	0.151261	0.151261	0.151261	0.151261	0.151261	0.151261
T_{out}-T_{in}	18.104	9.686	10.125	4.051	2.784	17.228	7.91	3.984	-1.194	2.078	13.834	5.02	3.269	2.218	1.567
avg ΔT	25.00114	21.62578	21.83228	18.57188	17.10195	24.57982	21.26086	18.6672	18.94574	15.45123	23.5316	19.92449	16.77367	15.41825	14.13857
total heat in	316.724	338.9073	531.4015	283.4841	292.2315	311.6904	286.2167	216.2365	-86.4078	225.5721	262.0918	190.2126	185.7983	168.0843	178.1254
avg heat flow	19269.19	20618.8	32329.96	17246.9	17779.08	18962.94	17413.15	13155.62	-5256.97	13723.59	15945.41	11572.35	11303.79	10226.09	10836.98
Nusselt #															
Reynolds #	4.84E+01	1.02E+02	1.62E+02	2.09E+02	3.09E+02	8.34E+01	1.87E+02	2.88E+02	4.15E+02	5.69E+02	2.46E+02	6.11E+02	9.59E+02	1.30E+03	1.93E+03
Prandtl #	633.3218	603.6091	569.4427	588.1578	595.2269	380.4304	338.9951	330.36	306.1395	334.6498	135.181	108.7618	103.9039	102.0409	103.5441
Graetz #															
$\Delta T_{fluid}/\Delta T_{wall}$	0.724127	0.447891	0.463763	0.218126	0.162788	0.7009	0.372045	0.213423	-0.06302	0.134488	0.58789	0.251951	0.194889	0.143856	0.110832
heat transf coeff	770.7323	953.4359	1480.833	928.6571	1039.594	771.4842	819.0239	704.7456	-277.475	888.1872	677.6169	580.8107	673.901	663.2459	766.4833
	enhancement ratio														
	1.022275	1.067994	1.614796	1.085187	1.027911	0.729856	1.050455	1.066702	-0.40083	1.032547	0.870763	0.869395	1.045246	0.962918	1.062537
Peclet #	3.07E+04	6.14E+04	9.20E+04	1.23E+05	1.84E+05	3.17E+04	6.35E+04	9.52E+04	1.27E+05	1.90E+05	3.32E+04	6.64E+04	9.97E+04	1.33E+05	1.99E+05

In this table are the results of testing ZIF-8 as a nanoparticle addition to Amsoil motor oil for the purposes of increasing heat transfer
The key quantity to look at is the enhancement ratio . This is the increase in heat transfer above the base oil alone. Any increases less than 5% may be attributed to experimental error.
The ZIF-8 molecule offers no increase in heat transfer

Fluid	2 wt.% ZIF in Amsoil					2 wt.% ZIF in Amsoil					2 wt.% ZIF in Amsoil				
Power	60%					60%					60%				
Temp Set	39.9°C					61°C					82°C				
Water Bath	39.9	39.9	39.9	39.9	39.9	61	61	61	61	61	82	82	82	82	82
Flow (ml/s)	10	20	30	40	60	10	20	30	40	60	10	20	30	40	60
inlet	42.923	44.114	44.72	45.542	46.663	61.54	62.38	63.062	63.239	64.12	77.268	79.378	80.771	81.753	82.47
1	55.28	54.86	54.78	55.02	55.65	73.62	72.99	72.38	71.95	72.24	89.11	89.21	89.1	89.7	90.09
2	69.48	64.91	63.19	62.57	62.75	87.59	82.56	80.41	79.39	78.92	103.7	98.4	96.83	96.36	95.8
3	74.61	67.9	65.21	63.97	63.48	93.04	85.66	81.97	79.89	78.71	109.1	101	97.25	96.18	95.45
4	81.78	74.63	70.71	68.41	67.36	99.2	90.97	85.51	83.18	82.27	113.9	104.3	100.2	99.5	98.98
5	84	76.85	73.23	71.1	70.15	101.2	93.66	88.51	86.08	84.93	115.4	107.3	103.2	102.1	101.3
6	85.15	78.4	74.88	73	71.31	100.9	94.9	89.63	86.49	85.2	114.9	108.1	103.3	102.2	101.3
outlet	58.96	53.681	50.152	49.19	49.358	75.548	69.616	66.854	65.953	66.051	91.189	84.796	83.769	83.712	83.921
density	853.4	853.4	853.4	853.4	853.4	853.4	853.4	853.4	853.4	853.4	853.4	853.4	853.4	853.4	853.4
viscosity	0.064166	0.061929	0.06033	0.060253	0.060958	0.037244	0.034458	0.03332	0.032923	0.033459	0.008442	0.006098	0.006299	0.006805	0.007311
specific heat	2050	2050	2050	2050	2050	2120	2120	2120	2120	2120	2220	2220	2220	2220	2220
therm cond	0.152045	0.152045	0.152045	0.152045	0.152045	0.152045	0.152045	0.152045	0.152045	0.152045	0.152045	0.152045	0.152045	0.152045	0.152045
T_{out}-T_{in}	16.037	9.567	5.432	3.648	2.695	14.008	7.236	3.792	2.714	1.931	13.921	5.418	2.998	1.959	1.451
avg ΔT	24.07172	20.67222	19.55154	18.30397	17.09999	24.01554	20.7754	18.10164	16.56111	15.2884	23.42457	19.28557	16.03646	14.93634	13.95451
total heat in	280.5625	334.7436	285.0936	255.2827	282.8893	253.4339	261.8286	205.8155	196.4076	209.6148	263.74	205.2932	170.3956	148.4568	164.9393
avg heat flow	17069.15	20365.48	17344.82	15531.15	17210.71	15418.67	15929.4	12521.62	11949.25	12752.77	16045.69	12489.84	10366.71	9031.969	10034.75
Nusselt #															
Reynolds #	3.53E+01	7.31E+01	1.13E+02	1.50E+02	2.23E+02	6.08E+01	1.31E+02	2.04E+02	2.75E+02	4.06E+02	2.68E+02	7.42E+02	1.08E+03	1.33E+03	1.86E+03
Prandtl #	865.1451	834.9818	813.4145	812.3815	821.8924	519.3074	480.4532	464.5819	459.0575	466.5277	123.2624	89.03971	91.96419	99.35527	106.7543
Graetz #															
$\Delta T_{fluid}/\Delta T_{wall}$	0.666218	0.462795	0.27783	0.199301	0.157602	0.583289	0.348296	0.209484	0.163878	0.126305	0.59429	0.280935	0.186949	0.131157	0.103981
heat transf coeff	709.0958	985.1616	887.1334	848.513	1006.475	642.0291	766.7433	691.7396	721.5249	834.1463	684.994	647.6263	646.4463	604.6976	719.1049
	enhancement ratio														
	0.940523	1.103531	0.967387	0.991534	0.995165	0.607386	0.983402	1.047016	1.042278	0.969722	0.880243	0.969409	1.002663	0.877916	0.996858
Peclet #	3.05E+04	6.10E+04	9.16E+04	1.22E+05	1.83E+05	3.16E+04	6.31E+04	9.47E+04	1.26E+05	1.89E+05	3.31E+04	6.61E+04	9.92E+04	1.32E+05	1.98E+05

In this table are the results of testing ZIF-8 as a nanoparticle addition to Amsoil motor oil for the purposes of increasing heat transfer
The key quantity to look at is the enhancement ratio . This is the increase in heat transfer above the base oil alone. Any increases less than 5% may be attributed to experimental error.
The ZIF-8 molecule offers no increase in heat transfer

IV

CONCLUSIONS AND FURTHER WORK

ZIF-8 is remarkable molecule in the class of MOFs. This author has shown that it can be made via a continuous and batch process with an order of magnitude savings both in time and money. The spray drying unit operation is the key to this. The density, specific heat, thermal conductivity, and BET surface area were determined experimentally. To our knowledge we are the first to report this. Unfortunately the low thermal conductivity, 0.113 W/m K renders the ZIF-8 molecule useless as an enhancer of heat transfer in a base fluid. The systematic error in the heat transfer rig at the University of Louisville has been discovered and eliminated. The literature suggests that experimental results of nanoparticle heat transfer experiments are rarely reproducible. Enhancement ratios less than 1.05 may be considered useless due to experimental error. This has inhibited commercial applications.

For further investigation:

1. Fouling of the heat transfer rig components after nanofluid processing.
2. Nanoparticle deformation after processing.
3. Use of high-flow, low-shear pumps for nanofluid processing.
4. Spray drying of CSTR products as a unit operation.
5. Use of ZIF-8 in other mass transfer operations.

REFERENCES

1. Yu, W., et al., *Review and Assessment of Nanofluid Technology for Transportation and Other Applications.* 2007.

2. Choi, S.U.S. and J.A. Eastman, *Enhancing thermal conductivity of fluids with nanoparticles.* The American Society of Mechanical Engineers, 1995.

3. Hwang, Y., et al., *Stability and thermal conductivity characteristics of nanofluids.* Thermochimica Acta, 2007. **455**(1/2): p. 70-74.

4. Hwang, Y., et al., *Stability and thermal conductivity characteristics of nanofluids.* Thermochimica Acta, 2007. **455**(1/2): p. 70-74.

5. Jang, S.P. and S.U.S. Choi, *Effects of various parameters on nanofluid thermal conductivity.* Journal of Heat Transfer-Transactions of the Asme, 2007. **129**(5): p. 617-623.

6. Choi, S.U.S., et al., *Anomalous thermal conductivity enhancement in nanotube suspensions.* Applied Physics Letters, 2001. **79**(14): p. 2252-2254.

7. Xuan, Y. and Q. Li, *Heat transfer enhancement of nanofluids.* International Journal of Heat and Fluid Flow, 2000. **21**(1): p. 58-64.

8. Xuan, Y.M. and Q. Li, *Investigation on convective heat transfer and flow features of nanofluids.* Journal of Heat Transfer-Transactions of the Asme, 2003. **125**(1): p. 151-155.

9. Wen, D.S. and Y.L. Ding, *Experimental investigation into convective heat transfer of nanofluids at the entrance region under laminar flow conditions.* International Journal of Heat and Mass Transfer, 2004. **47**: p. 5181-5188.

10. Xie, H.Q., Y. Li, and W. Yu, *Intriguingly high convective heat transfer enhancement of nanofluid coolants in laminar flows.* Physics Letters A, 2010. **374**(25): p. 2566-2568.

11. Choi, C., H.S. Yoo, and J.M. Oh, *Preparation and heat transfer properties of nanoparticle-in-transformer oil dispersions as advanced energy-efficient coolants.* Current Applied Physics, 2008. **8**(6): p. 710-712.

12. Yang, Y., et al., *Heat transfer properties of nanoparticle-in-fluid dispersions (nanofluids) in larninar flow.* International Journal of Heat and Mass Transfer, 2005. **48**(6): p. 1107-1116.

13. Li,Zhou Tung, Schneider, and Xi. *A review on the development of nanofluid preparation and chaaacterization.* Powder Technology, 196, (2009), 89-101.

14. McKetta J. J. (Executive Ed.), Cunningham W. A. (Associate Ed.), *Encyclopedia of Chemical Processing and Design*, Marcel Decker, New York, 20 (1984) 177.

15. An Ullmann Encyclopedia: *Industrial Organic Chemicals*: Starting Materials and Intermediates, vol. 2, Wiley-VCH, New York, 1999, p.1045.

16. Srivastava R., Srinivas D., Ratnasamy P., *Catal. Lett*. 89 (2003) 81.

17. Srivastava R., Srinivas D., Ratnasamy .P, *Catal. Lett*. 91 (2003) 133.

18. Srivastava R., Manju M. D., Srinivas D., Ratnasamy P., *Catal. Lett*. 97 (2004) 41.

19. Srivastava R., Bennur T. .H, Srinivas, D., *J. Mol. Catal. A. Chemical* 226 (2005) 199.

20. Srivastava R., Srinivas D., Ratnasamy P., *J.Catal.* 233 (2005) 1.

21. Srivastava R., Srinivas D., Ratnasamy P., *Appl. Catal. A: General*. 289 (2005) 128.

22. Srivastava R., Srinivas D., Ratnasamy P., *Microp. Mesop. Mater.* 90 (2006) 314.

23. Srivastava R., Srinivas D., Ratnasamy P., *Tetrahedron Lett*. 47 (2006) 4213.

24. Srivastava R., Srinivas D., *Handbook of Heterogeneous Catalysis*, 2nd Edition, Edited by Ertl G., Knozinger H., Schuth F., Weitkamp J., Wiley-VCH. 7 (2008) Chapter 14, 3717.

25. Srinivas D., Srivastava R., Ratnasamy P., *US. Patent.* 7405319 (2008).

26. Srinivas D., Srivastava R., Ratnasamy P., *US. Patent.* 7518012 (2009).

27. An Ullmann Encyclopedia: *Industrial Organic Chemicals*: Starting Materials and Intermediates, vol. 2, Wiley-VCH, New York, 1999, p.1045.

28. Li K.T., Peng Y.J., *J. Catal.* 143 (1993) 631.

29. Chen B., Chuang S.S.C., *J. Mol. Catal. A: Chem.* 195 (2003) 37.

30. Dell'Amico D.B., Calderazzo F., Labella L., Marchetti F., Pampaloni G., *Chem. Rev.* 103 (2003) 3857.

31. Aresta M., Quaranta E., *Tetrahedron* 48 (1992) 1515.

32. Li Q., Wang J., Dong W., Kang M., Wang X., Peng S., *J. Mol. Catal. A: Chem.* 212 (2004) 99.

33. Aresta M., Dibenedetto A., Quaranta W., Bascolo M., Larsson R., *J. Mol. Catal. A: Chem.* 174 (2001) 7.

34. Shi F., Deng Y., *J. Catal.* 211 (2002) 548.

35. Wolf A., Schuth F., *Appl. Catal. A* 226 (2002).

36. Sima T., Guo S., Shi F., Deng Y., *Tetrahedron Lett.* 43 (2002) 8145.

37. Hayashi H., Cote A. P., Furukawa H., O'Keeffe M., Yaghi O. M., *Nature Mater. 6 (*2007) 5.

38. Banerjee R., Phan A., Wang B., Knobler C., Furukawa H., O'Keeffe M., Yaghi O. M., *Science.*319 (2008) 939.

39. Wang B., Coˆte A. P., Furukawa H., O'Keeffe M., Yaghi O. M., *Nature.* 453 (2008) 207.

40. Morris W., Doonan C. J., Furukawa H., Banerjee R., Yaghi, O. M., *J. Am. Chem. Soc. 130 (*2008) 12626.

41. Phan A., Doonan, C. J., Uribe-Romo F. J., Knobler C.B, O'Keeffe M., Yaghi O. M., *Acc. Chem. Res.*43 (2010).

42. Cravillon J., Muzer S., Lohmeier S. J., Feldhoff A., Huber K., Wiebcke M., *Chem. Mater.* 21 (2009) 1410.

43. Kalidindi S. B., Esken D., Fischer R. A., *Chem. Eur. J.* 17 (2011) 6594.

44. Tran U. P. N., Le K. K. A., Phan N. T. S., *ACS Catalysis* 1 (2) (2011)120.

45. Nguyen L. T. L., Le K. K. A., Phan N. T. S., *Chinese Journal of Catalysis* 33(4) (2012) 688.

46. Miralda C. M., Macias E. E., Zhu M., Ratnasamy P., Carreon M. A., *ACS Catal.* 2 (1) (2012) 180.

47. Zhu M., Venna S. R., Jasinski J. B., Carreon M. A., *Chem. Mater.* 2011, 23 (16), pp 3590.

48. Avrami, M. J. *Chem. Phys.* 1939, 7, 1103. (b) Avrami, M. J. *Chem. Phys.* 1940, 8, 212. (c) Avrami, M. J. *Chem. Phys.* 1941, 9, 177.

49. Venna S. R., Jasinski J. B., Carreon M. A., *J. Am. Chem. Soc.* 132 (2010) 18030.

50. Vozár L, A Computer-Controlled Apparatus for Thermal Conductivity Measurement by the Transient Hot Wire Method, 1996, *Journal of Thermal Analysis*, **46**, 495-505.

51. Verderman, et al., *Drying Technology*: 22, 6, 1403-1461 (2004).

52. Simpson, J.A., Weiner, E.S.C.. *The Oxford English Dictionary*. Clarendon Press, Oxford: 1986.
53. Willing, G.. Tatarko, J.L.. *Unpublished Papers* submitted to the *Journal of Applied Physics*.
54. http://www.tankonyvtar.hu/hu/tartalom/tamop425/0032_hidrologia/ch06s05.html
55. http://iopscience.iop.org/1748-3190/7/4/046003/pdf/1748-3190_7_4_046003.pdf
56. http://surfguppy.com/particles-suspended-liquid/
57. http://glass.phys.uniroma1.it/dileonardo/Abstracts.php?topic=SoftMatter
58. http://www.aviation-for-kids.com/the-magnus-force.html
59. http://www.sepscience.com/Techniques/LC/Articles/702-/HPLC-Solutions-10-Pore-Size-vs-Particle-Size
60. Mezhericher, Maksim. *Theoretical Modeling of Spray Drying Processes*. Lambert Academic Publishing, Saarbrucken, Germany: 2011.
61. Sastry, Susarla, V.A.R., Kumar, Kalamchety,S.R.R.. *Fuzzy Logic Control of Continuous Stirred Tank Reactor (CSTR)*. Lambert Academic Publishing, Saarbrucken, Germany: 2012
62. http://uctchem.blogspot.com/2011/01/spray-dryer.html
63. http://www.buchi.nl/Spray-Drying-Spray-Dryer-BU.1947.0.html
64. Timofeeva et al. *Nanoscale Research Letters* 2011, 6:182
65. http://en.wikipedia.org/wiki/Surfactant
66. http://encyclopedia.che.engin.umich.edu/Pages/Reactors/CSTR/CSTR.html
67. http://en.wikipedia.org/wiki/Phonon
68. Renewable energy book
69. Huang, D.. *Modeling of Particle Formation During Soray Drying*. European Drying Conference 2010.
70. Brenn, G.. Concentration fields in drying droplets, *Chemical Engineering Technology*, 27 (12) 1252-1258, 2004.
71. http://www.consultexim.hu/katalogus/armfield/dshtml/images/d_cex.gif
72. Ratner, Bruce. *Statistical Modeling and Analysis for Database Marketing*. CRC Press, Boca Raton: 2003.
73. http://www.cse. Monash.edu.Au/courseware/CSE5301.
74. http://en.wikipedia.org/wiki/
75. Evans, W., Fish, J., Keblinski, P., Role of Brownian motion hydrodynamics on nanofluid thermal conductivity. *Applied Physics Letters*. 88,093116 (2006).

76. http://www.springer.com/cda/content/document/cda_downloaddocument/9781461479895-c2.pdf?SGWID=0-0-45-1411617-p175260237.

77. *Zumbuhllab.unibas.ch/pdf/talks/080425_Tobias.*

78. Yu, W., et al., *Review and Assessment of Nanofluid Technology for Transportation and Other Applications.* 2007.

79. Chen, L.F. and H.Q. Xie, *Silicon oil based multiwalled carbon nanotubes nanofluid with optimized thermal conductivity enhancement.* Colloids and Surfaces a-Physicochemical and Engineering Aspects, 2009. **352**(1-3): p. 136-140.

80. Jwo, C.S., et al., *Performance of overall heat transfer in multi-channel heat exchanger by alumina nanofluid.* Journal of Alloys and Compounds, 2010. **504S**: p. S385-S388.

81. Chun, B.H., H.U. Kang, and S.H. Kim, *Effect of alumina nanoparticles in the fluid on hea trasnfer in double pipe heat exchanger system.* Korean Journal of Chemical Engineering, 2008. **25**: p. 966-971.

82. Yang, Y., et al., *Heat transfer properties of nanoparticle-in-fluid dispersions (nanofluids) in larninar flow.* International Journal of Heat and Mass Transfer, 2005. **48**(6): p. 1107-1116.

83. Wen,D., Lin,G., Vafaei, S., Zhang, K..*Review of nanofluids for heat transfer applications*. Particuology 7, (2009), p 141-150.

84. Saidur, R., Leong, K.Y., Mohammed, H.A.. *A review on applications and challenges of nanofluids.* Renewable and Sustainabel Energy Reviews. 15, (2011), 1646-1668.

85. *nanoparticle-blog.com*

86. Pang,C., Lee, J.W., Hong, H., Kang,Y.T.. *Heat conduction mechanisms in nanofluids.* Journal of Mechanical Science and Technology. 28, (7), (2014), 2925-2936.

87. Nine, Md. J., Chung, Hanghik, Tanshen, Md. Riyad, Osman, N.A.B. Abu, Jeong, Hyomin. *Is metal nanofluid reliable as a heat carrier.* Journal of Hazardous Materials, 273,(2014) 183-191.

88. Zerradi,Hicham, Ouskit, Said, Dezairi, Aouatif, Loulijai, Hamid, Mizanai, Sofia. *New Nusselt nuber corelations to predict thermal conductivity of nanofluids.* Advanced Powder Technology. 25,(2014), 1124-1131.

89. Haddad, Zoubida, Abid, Cherifa, Oztop, Haran, Mataoui, Amina. *A review on how Researchers Prepare their nanofluids*. International Journal of Thermal Sciences. 76, (2014),168-169.

90. Kosmulski M. *Surface Charging and Points of Zero Charge*. CRC Press: Boca Raton, 2009.

91 Shima, P.D., Philip, John. *Role of Thermal conductivity of dispersed nanoparticles on heat transfer properties of nanofluid.* Ind. Eng. Chem. Res. 2014, 53, 980-988.

92. Ali, M., El-Leathy, M., Al-Sofyany, Z.. *The Effect of Nanofluid concentration on the Cooling System of Vehicles radiator.* Advances in Mechanical Engineering. 2014, 962510.

93. Hussein, Adnan, Sharma, K.V., Bakar,R. A., Kadirgama, K.. *A review of forced convection heat transfer enhancement and hydrodynamic characteristics of a nanofluid.* Renewable and Sustainable Energy Reviews. 29, (2014), 734-743.

94. Anoop, P.K., Cox, J., Sadr, R.. *Thermal evaluation of nanofluids in heat exchangers*. International Communications in Heat and Mass Transfer. 49, (2013), 5-9.

95. Xuan,Y., Li, Q., Tie, P.. *The effects of surfactants on heat transfer feature of nanofluids*. Experimental Thermal and Fluid Science. 46, (20130, 259-262.

96 Sharul, I.M., Mahbubul, S.S., Kaleduzzamann, S.S., Saidur, R., Sabri, M.F.M.. *A comprehensive review on the specific heat of nanofluyids for energy perspective.* Renewable and Sustainable Energy Reviews. 38, (2014), 88-98.

97. Shaker, M., Birgersson, E., Mujumdar, R.S.. *Extende Maxwell model for the thermal conductivity of nanofluids that accounts for nonlocal heat transfer.* International Journal of Thermal Sciences. 84, (2014), 260-266.

98. Said, Z. Sajil, M.H., Saidur, R., Komaisarvestawi, M.,Rahim, N.A.. *Radiative Properties of nanofluids.* International Communications in Heat and Mass Transfer. 46, (2013) 74-84.

99. Brewster, M.Q., Brewster. *Thermal Radiative Transfer and Properties.* Willey: New York 1992.

100. Boqui, Xiao, Yi, Yang, Lingxia, Chen. *Developing a novel form of thermal conductivity of nanofluids with Brownian motion effect by means of fractal geometry.* Powder Technology. 239, (2013) 409-414.

101. Michaelides, E. *Transport properties of naofluids. A critical review.* J. of Non-equilibrium Thermodynamics. 38, (2013), 1-79.

102. Demir, N.K., Topuz, B., Yilmaz, L., Kalipcilar, H.. *Synthesis of ZIF-8 from recycled mother liquors.* Microporous . and Mesoporous Materials, 198, (2014) 291-300.

103. Chen, B., Yang, Z., Zhu, Y., Xia, Y.. *Zeolitic imidazolate framework materials: recent progress in synthesis and applications.* Journal of Materials Chemistry A. 2104, 2 16811.

104. Tan, J., Bennett, T., Cheetham, A.. *Chemical structure, network topology. And porosity effects on the mechanical properties of zeolitic imidazolate frameworks.* PNAS, June 1, 2010 no. 22.

105. Low, Z. X., Yao, J., Lin, Q., He, M., Wang, Z., Akkihebhal, S., Bellare, J., Wang, H.. *Crystal transformation in zeolitic-imidazolate framework.* Crystal Design and Growth. 2104,14, 6589-6598.

106. Chen, B., Bai, F., Zhu, Y., Xia, Y.. A cost-effective method for the synthesis of zeolitic *imidazolate framework-8 materials from stoichiometric precursors via aqueous ammonia modulation at room temperature.* Microporous and Mesoporous Materials. 193, (2014) 7-14.

107. Kida, K., Okita, M., Fujita, K., Tanaka, S., Miyako, Y.. Cryst.Eng Comm. 15 (2013) 1764.1801.

108. Bazer-Bachi, D., Assie, L., Lecocq, V., Harbuzaru, B.. *Towards, Industrial use of metal organic framework: impact of shaping on MOF properties.* Powder Technology. 255, (2014) 52-59.

109. Cho, H. X.., Kim, Jun, Kim, Se-Na, Ahn, W.S.. *High yield synthesis of ZIF-8 via sonochemical route 1-L.* Microporous and Mesoporous Materials. 169 (2013) 180-184.

110. Zhang, X., Jiang, J.. *Thermal conductivity of zeolitic imidazolate framework -8; a molecular simulation study.* Journal of Physical Chemistry C. 2013, 117, 18441-18447.

111. Vehring, Reinhard, Foss, Willard, Lechuga-Ballesteros, D.. *Particle Formation in Spray Drying*. Aerosol Science 38 (2007), 728-746.

112. Anandharamakrishna, C.. *Fluid Dynamics Applications in Food Processing*. Springer Briefs in Food, Health, and Nutrition. 2013.

113. Vincente, J., Pinto, J., Menezes, J., Gaspar, F.. *Fundamental Analysis of Particle Formation in Spray Drying.* Powder Technology. 247 (2013), 1-7.

114. Mezericher, M., Levy, A., Burde, I.. *Theoretical Models of Single Droplet Drying Kinetics.* Drying Technology. 28,278-293, 2010.

115. Masters, K..*Spray Drying, An Introduction to Principles, Operational Practice, and Applications.* Leonard Hill Books: London, 1972.

116. Dobry, D., Settell, D., Baumann, J.M., Ray, R., Graham, L., Reyerinick, R.A.. *A Model-Based Methodology for Spray Drying Process Development.* J. Pharm. Innov. (2009),4:133-142.

117. Chen, D.X.. *Heat-Transfer and Structure Formation During Drying of Single Food Droplets.* Drying Technology. Vol. 22 Nos. 1 and 2, 179-190, 2004.

118. Leong, K.Y., Saidur,R., Mahlin, T.M.I., Yau, Y.H.. *Entropy generation analysis of nanofluid flow in a circular tube subjected to constant wall temperature.* International Communications in Heat and Mass Transfer. 39 (2012), 1169-1175.

119. Kamyar, A., Saidur, R., Hasanuzzaman, M.. *Application of Computational Fluid Dynamics (CFD) for nanofluids.* International Journal of Heat and Mass Transfer. 55 (2012), 4104-4115.

120. Wu, J.M., Zhao, Jiyun. *A review of nanofluid heat transfer abd critical heat flux enhancement- research gap to engineering application.* Progress in Nuclear Energy. 66 (2013), 13-24.

121. Liu, L., Kim, E.S., Park, Y.G., Jacobi, A.. *The Potential Impact of Nanofluid Enhancements on the Performance of Heat Exchangers*. Heat Transfer Engineering. 33 (1):31-41, (2012).

122. Hui, Wu, Wei, Zhou, Taner, Yildrim. *Hydrogen Storage in a Prototypical Zeolitic Imidazolate Framework-8*. J. Am. Chem. Soc., 2007, 129, 5314-5315.

123. Hertag, Bux, Caro,Chmelik, Remsungnen, Knauth, Fritzsche. *Diffusion of CH_4 and H_2 in ZIF-8*. Journal of Membrane Science, 2011, 377, 36-41.

124. Cravillon, Schroder, Nayuk, Gummel, Huber, Wiebcke. *Fast Nucleation and Growth of ZIF 8*. Angewandte Chemie, 2011, 50, 8067-8071.

125. Jimenez, Moggach, Wharmby, Wright, Parsons, Duren. *Opening the Gate: Framework Flexibility in ZIF-8 Explored by Experiment and Simulation*. J. Am. Chem. Soc., 2011, 133, 8900-8012.

126. Pan, Y.; Liu, Y.; Zeng, G.; Zhao, L.; Lai, Z., *Rapid synthesis of zeolitic imidazolate framework-8 (ZIF-8) nanocrystals in an aqueous system*. ChemComm 2011, 47, 2071-2073.

127. Sastry, S.V.A.R., Kumar, K.S.R.. *Fuzzy Logic Control of Continuous Stirred Tank Reactor (CSTR)*. Lambert Academic Publishing: Saarbrucken, De., 2012.

128. Hung, Yi-Hsuan, Teng, Tun-Ping, Teng, Tun-Chen, Chen, J.H.. *Assesment of heat dissipation performance for nanofluid.*Applied Thermal Engineering, 32 (2102), 132-140.

129. http:\www.advancedlab.org/mediawiki/index.php/simulating_Brownian_Motion.

APPENDICES

APPENDIX A

MATLAB Code for Brownian Motion[129]

```
N = 1000;
displacement = randn(1,N);
plot(displacement);


hist(displacement, 25);


x = cumsum(displacement);
plot(x);
ylabel('position');
xlabel('time step');
title('Position of 1D Particle versus Time');


particle = struct();
particle.x = cumsum( randn(N, 1) );
particle.y = cumsum( randn(N, 1) );
plot(particle.x, particle.y);
ylabel('Y Position');
xlabel('X Position');
title('position versus time in 2D');


dsquared = particle.x .^ 2 + particle.y .^ 2;
plot(dsquared);


d    = 1.0e-6;              % radius in meters
eta  = 1.0e-3;              % viscosity of water in SI units (Pascal-
seconds) at 293 K
kB   = 1.38e-23;            % Boltzmann constant
T    = 293;                 % Temperature in degrees Kelvin

D    = kB * T / (3 * pi * eta * d)

ans =
      4.2902e-013

dimensions = 2;         % two dimensional simulation
tau = .1;               % time interval in seconds
time = tau * 1:N;       % create a time vector for plotting

k = sqrt(D * dimensions * tau);
dx = k * randn(N,1);
dy = k * randn(N,1);

x = cumsum(dx);
y = cumsum(dy);
```

```
dSquaredDisplacement = (dx .^ 2) + (dy .^ 2);
 squaredDisplacement = ( x .^ 2) + ( y .^ 2);

plot(x,y);
title('Particle Track of a Single Simulated Particle');



clf;
hold on;
plot(time, (0:1:(N-1)) * 2*k^2 , 'k', 'LineWidth', 3);      % plot
theoretical line

plot(time, squaredDisplacement);
hold off;
xlabel('Time');
ylabel('Displacement Squared');
title('Displacement Squared versus Time for 1 Particle in 2
Dimensions');

simulatedD = mean( dSquaredDisplacement ) / ( 2 * dimensions * tau )

ans =
     4.2192e-013

standardError = std( dSquaredDisplacement ) / ( 2 * dimensions * tau *
sqrt(N) )
actualError = D - simulatedD

standardError =
               1.3162e-014

actualError   =
               7.1019e-015


dx = dx + 0.2 * k;
dy = dy + 0.05 * k;

x = cumsum(dx);
y = cumsum(dy);

dSquaredDisplacement = (dx .^ 2) + (dy .^ 2);
 squaredDisplacement = ( x .^ 2) + ( y .^ 2);

simulatedD    = mean( dSquaredDisplacement ) / ( 2 * dimensions * tau )
standardError = std(  dSquaredDisplacement ) / ( 2 * dimensions * tau *
sqrt(N) )
actualError = D - simulatedD

plot(x,y);
title('Particle Track of a Single Simulated Particle with Bulk Flow');

simulatedD    =
               4.2926e-013
standardError =
```

```
               1.3694e-014
actualError   =
              -2.3859e-016

clf;
hold on;
plot(time, (0:1:(N-1)) * 2*k^2 , 'k', 'LineWidth', 3);      % plot
theoretical line
plot(time, squaredDisplacement);
hold off;

xlabel('Time');
ylabel('Displacement Squared');
title('Displacement Squared versus Time with Bulk Flow');

particleCount = 10;
N = 50;
tau = .1;
time = 0:tau:(N-1) * tau;
particle = { };             % create an empty cell array to hold the
results

for i = 1:particleCount
    particle{i} = struct();
    particle{i}.dx = k * randn(1,N);
    particle{i}.x = cumsum(particle{i}.dx);
    particle{i}.dy = k * randn(1,N);
    particle{i}.y = cumsum(particle{i}.dy);
    particle{i}.drsquared = particle{i}.dx .^2 + particle{i}.dy .^ 2;
    particle{i}.rsquared = particle{i}.x .^ 2 + particle{i}.y .^ 2;
    particle{i}.D = mean( particle{i}.drsquared ) / ( 2 * dimensions *
tau );
    particle{i}.standardError = std( particle{i}.drsquared ) / ( 2 *
dimensions * tau * sqrt(N) );

help SimulateParticles

particle = SimulateParticles(N, particleCount, tau, k);

usage: out =
SimulateParticles( N, particleCount, tau, k )

N is the number of samples
particleCount is the number of particles
tau is the sample period
k is the standard deviation of dx and dy

returns a cellular array of length particleCount

clf;
hold on;
for i = 1:particleCount
    plot(particle{i}.x, particle{i}.y, 'color', rand(1,3));
end

xlabel('X position (m)');
ylabel('Y position (m)');
```

```
title('Combined Particle Tracks');
hold off;

% compute the ensemble average
rsquaredSum = zeros(1,N);

for i = 1:particleCount
    rsquaredSum = rsquaredSum + particle{i}.rsquared;
end

ensembleAverage = rsquaredSum / particleCount;

% create the plot
clf;
hold on;
plot(time, (0:1:(N-1)) * 2*k^2 , 'b', 'LineWidth', 3);      % plot
theoretical line

plot(time, ensembleAverage , 'k', 'LineWidth', 3);          % plot
ensemble average
legend('Theoretical','Average','location','NorthWest');

for i = 1:particleCount
    plot(time, particle{i}.rsquared, 'color', rand(1,3));   % plot each
particle track
end

xlabel('Time (seconds)');
ylabel('Displacement Squared (m^2)');
title('Displacement Squared vs Time');
hold off;

clear D e dx;

% extract the D value from each simulation and place them all into a
single
% matrix called 'D'
for i = 1:particleCount
    D(i) = particle{i}.D;
    dx(i,:) = particle{i}.dx;
    e(i) = particle{i}.standardError;
end

% compute the estimate of D and the uncertainty
averageD = mean(D)
uncertainty = std(D)/sqrt(particleCount)

% plot everything
clf;
hold on;

plot(averageD * ones(1,particleCount), 'b', 'linewidth',
3);                    % plot estimated D
plot((averageD + uncertainty) * ones(1,particleCount), 'g-',
'linewidth', 1);   % plot upper error bar
plot((averageD - uncertainty) * ones(1,particleCount), 'g-',
'linewidth', 1);   % plot lower error bar
```

```
errorbar(D,e,'ro');
         % plot D values with error bars

xlabel('Simulation Number');
ylabel('Estimated Diffusion Coefficient');
title('Estimated Diffusion Coefficient with Error Bars')
legend('Average Value of D', 'location', 'NorthWest');

hold off;

averageD    =
             4.2886e-013

uncertainty =
             2.3294e-014
```

APPENDIX B

SAMPLE CACULATIONS

Derivation of Peclet Number from the species transport equation.

$$\partial c / \partial t + v_x \, \partial c / \partial x + v_y \, \partial c / \partial y = 0 \qquad \text{(B 1)}$$

Let's define characteristic scales.

$v_i^* = v_i / U$ Where v_i is a velocity in the *ith* direction and U is a scaling velocity.

$x_i^* = x_i / L$ Where x_i is a length in the *ith* direction and L is a scaling length.

$c^* = c / c_o$ Where c_o is a characteristic concentration.

∂_j^* is the derivative with respect to the dimensionless spatial variable x_j^*

Substituting into the species transport equation (B 1):

$$(U c_o / L) \; v_j^* \; \partial_j^* \, c^* = (D \, c_o / L^2) \, \partial_j^* \partial_j^* \, c^*$$

The Peclet number thus becomes ($U L / D$) where D is the mass diffusivity.

The Peclet number for mass transport is the ratio of convection to diffusion.

The Peclet number for heat transfer is similar with the diffusivity *D* replaced with *α,* the thermal diffusivity.

Calculations for processing parameters for nanofluids (such as thermal conductivity k), are

based on **% volume** fractions NOT % weight fractions.

$$\frac{k}{k_f} = \frac{1 + 2\beta\phi}{1 - \beta\phi} \qquad \text{(B 2)}$$

Where k is the conductivity of the nanofluid, k_f the base fluid, θ, the volume fraction of the nanoparticle and $\beta = (k_p - k_f) / (k_p - 2k_f)$.

For the specific heat: $\boldsymbol{C_p}$

$$(C_p)_{nf} = [(1-\phi)(\rho C_p)_f + \phi(\rho C_p)_n]/[\phi\rho_n + (1-\phi)\rho_f] \qquad \text{(B 3)}$$

Where φ is the volume fraction of the nanoparticle and the subscripts *f* and *n* refer to the base fluid and nanoparticle respectively. The density is ρ.

APPENDIX C

BET Surface Area Analyzer Instructions

By Zachary Herde

Signing Up for Times/Log Book

Before beginning any experiments, you must first book your time in the log book as well as fill out the required information in the logging portion.

1. Sign up for time
2. Place all information in the logging portion

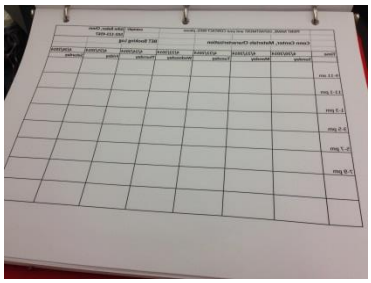

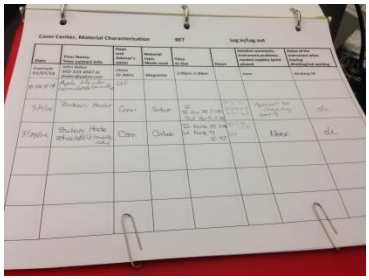

Degassing Sample

To begin, you must degas your sample to remove any gas that could be trapped in the pores and other surfaces of your material, this ensures that you get an accurate reading when you use the machine.

1. Zero the balance with the metal, red, pencil cup on the platform.
2. Weigh a clean and dry tube by placing it in the pencil cup and record the mass. (You will need this later.)
3. Weigh out between 0.1 and 0.5 grams of your sample.
4. Using the plastic cylinder funnel, pour the sample into your sample tube and then take the mass of the tube with the sample and record. (You will want this for comparison.)


5. Repeat steps 1-4 as necessary for all your samples.
6. To degas, your material must be heated. The temperature will depend on how well your sample can stand up to heat. However, the temperature generally used is 160˚C. Adjust the degas system to your temperature using the arrow buttons on the degas machine. (Note, the red display is the actual temperature and the green display is the temperature that the system is set to.)

7. Take the first needle/hose mechanism and slide it into your tube until the tip of the metal piece is right above your sample.

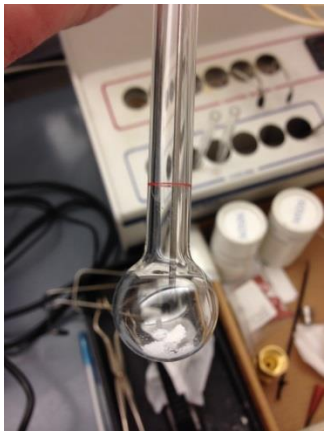
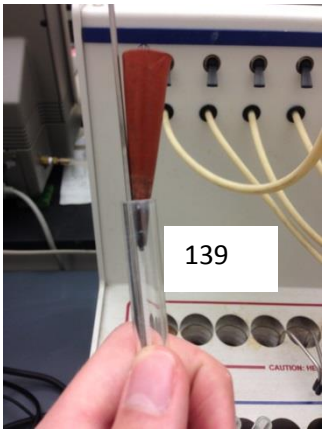

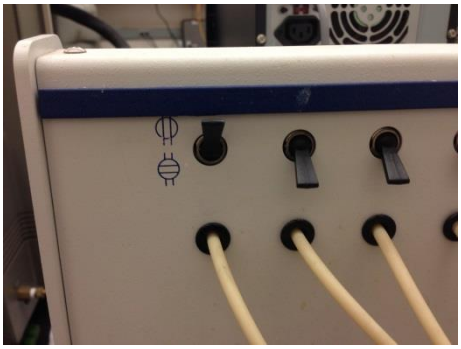

8. Place one of the rubber cylinders into the mouth of the tube to hold the metal piece in place.

9. Place the tube in the heating side (red border) of the degas machine and flip the switch above where the hose leads into the machine to the open position. (This allows any gas coming off of the sample to be removed.)
10. Repeat for your other samples.
11. Allow the tubes to heat for your desired time. (Usually about 2-3 hours)
12. After degas, remove the hose, flip the switch back, and weigh the tube using the pencil cup again. (Hold your finger over the tube opening to prevent any gas from getting in during transport from the machine to the balance. This mass should be less than your previous mass measured in step 4. If not, try again by zeroing the balance. If it still does not end up being less, then something is not correct.)

13. Place one of the glass filler rods into the tube to prevent gas from getting into the tube and place the tube into the cooling side of the degas machine.


14. Repeat for all your samples.
15. Turn the degas machine's temperature back down to zero.

Entering Sample Information

1. Click on File→Open→Sample Information
2. A Box will appear with file selections and a number in the file name box. Press ok without selecting anything.
3. A Box will appear saying that the file number does not exist and do you want to create it. Click yes.

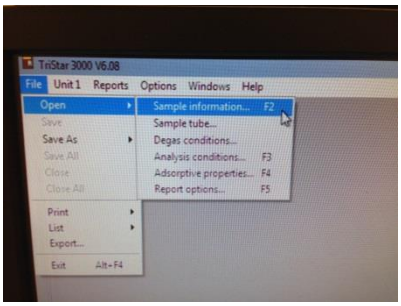

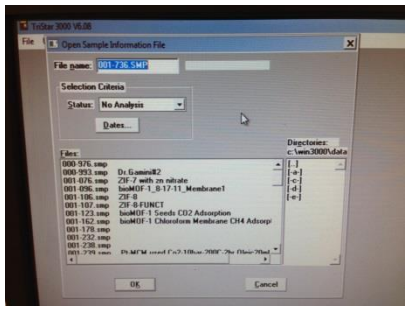

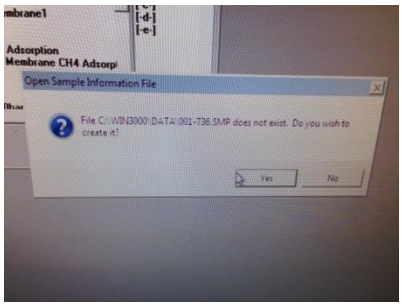

4. A new window will appear. This is where you will enter the data for your sample. In the sample information tab you will enter the sample name, your name as the operator, and the mass in the mass bar. To calculate the mass, take the mass of your tube with the degassed sample and subtract the mass of the tube by itself.

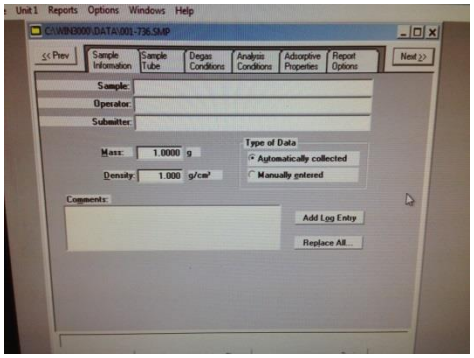

5. In the sample tube tab you will not have to do anything.

6. The Degas conditions tab allows you to set up the parameters by which you did your degas. Change the soak temperature to the temperature that you degassed your samples at. Leave the ramp rate alone and change the soak time to the amount of time in minutes that you degassed your samples.

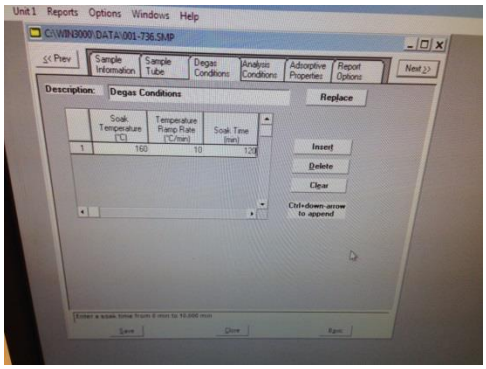

7. The Analysis Conditions tab allows you to change the points and various pressures at which the machine will take data. Click on “Pressures”, then a new window will appear. Click on “inse 141 fined”. Another window will appear with four drop down boxes. For surface area, select “5 point low pressure”. For t-plot micropore, select “10 Point”. And for BJH Adsorption and Desorption, select “20 Point” for both. Click “ok”.

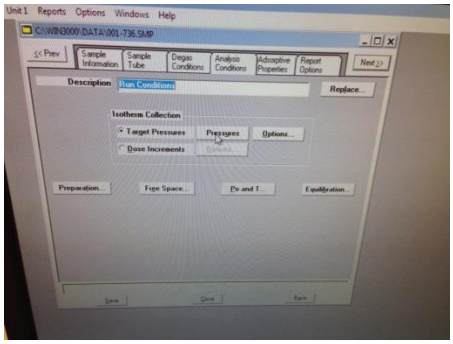
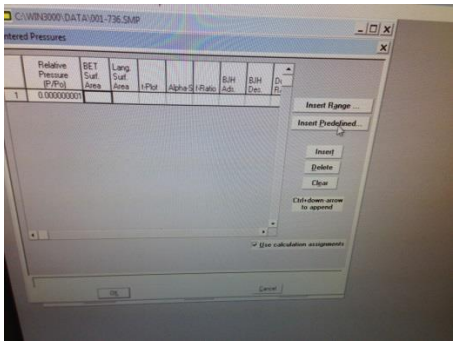
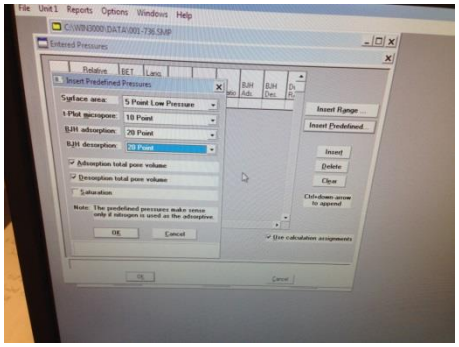

8. When you click ok, a chart with X's will appear. For the first two columns (BET and Langmuir), click in every box that 0.30000>. Fill in the third column by clicking the boxes from 0.06000 to 0.550000.

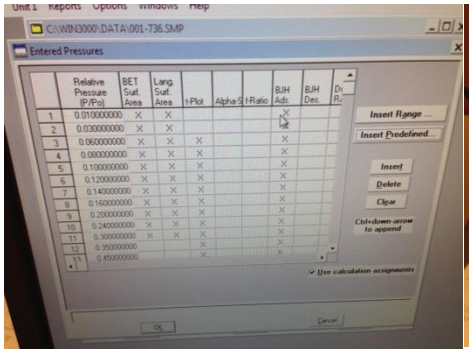
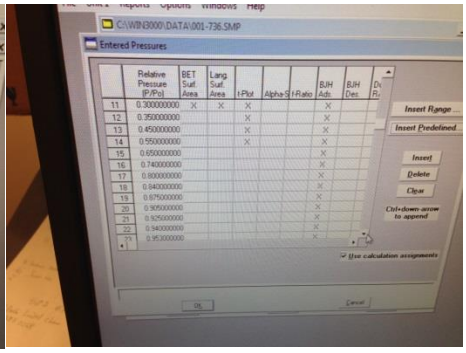

9. Ignore Alpha-S and f-Ratio Columns.

10. Fill the BJH Ads. Column from 0.010000 to 0.989000. At that point, there should be an X right next to it in the BJH Des. Column. Leave that one marked and then fill the rest of the BJH Des. column. Click "ok" when finished.

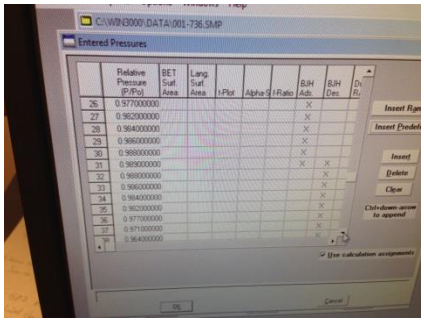
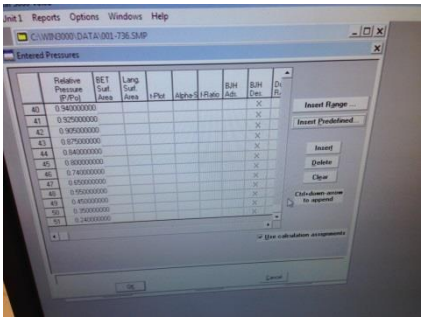

11. Skip the adsorptive properties tab.
12. In the report options tab, click on replace and a window will pop up. Select the "full report set" and click "ok". Click on "save' and then "close".

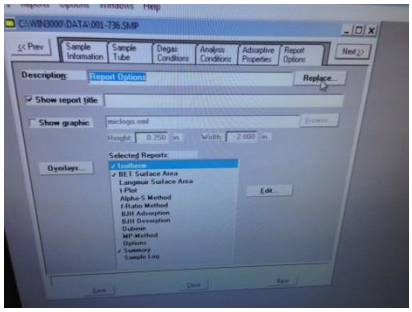
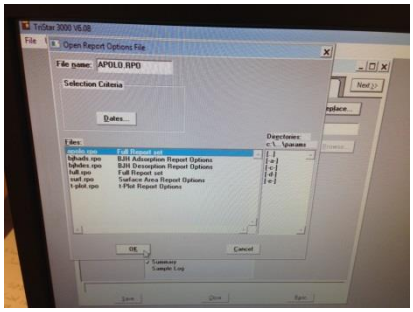

13. Repeat the above steps for your other samples.

Placing the Tubes into the Machine

1. Take the large metal dewar and dewar gauge and fill the dewar with liquid nitrogen obtained from the large tank until the level of the nitrogen is between the bottom of the gauge and the hole on the gauge. (Make sure to mark on the calendar next to the liquid nitrogen tank that you used it for BET. Cover with a piece of paper while you finish set-up.)

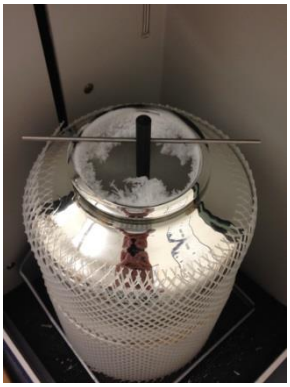

2. Place the dewar back on the platform inside the machine.
3. The machine has three ports total. There is a diagram on the back panel of the machine that explains which port is which. When loading the tubes, always load from the back if you are using all three ports. (Ex. I have three samples; I load my 3rd sample into port 3 first.)
4. Take the isothermal jacket and slide it over the sample tube until the bottom of the jacket reaches the red line on the tube.

5. Slide the circular foam piece onto the metal rod in the machine and then place your tube through the appropriate hole in the foam.

6. Take a metal coupler and slide it over the sample tube, it should be on top of the foam.
7. Take a black o-ring and place on the sample tube.

8. Gently push the tube straight up into the port and screw the couple in until it is tight. (Sometimes it is easier to push the ring in with the inner couple first to straighten the tube and get it into place before screwing it all together.)



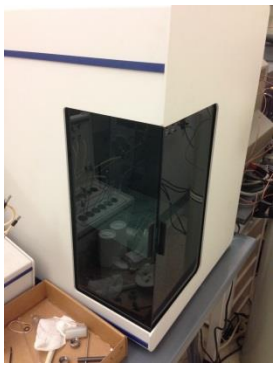

9. Repeat for other sample tubes.
10. Close the door panels.

Starting the Experiment

1. Click on the Unit 1 menu at the top of the screen and then sample analysis.

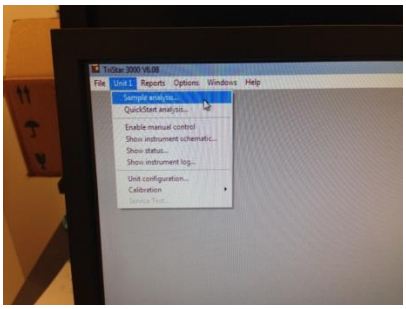
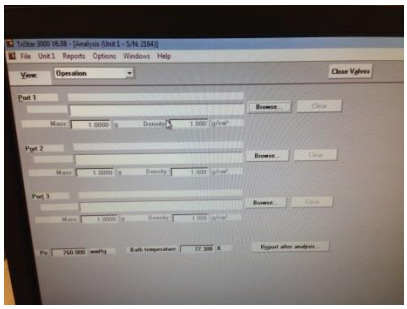

2. The information bars for three samples will come up. Each information section corresponds to a port on the machine. Make sure to place the correct sample information into the correct port section.
3. Click on browse to search for your sample. Change the status to “no analysis” and find your file from that selection. (It will appear as the name of the sample you entered earlier.)

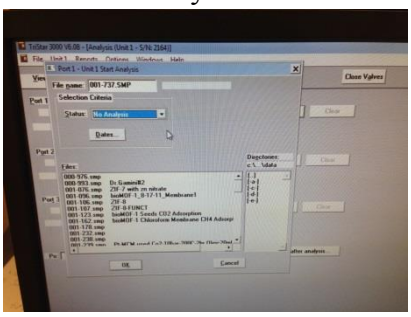

4. Click on your sample file and then “open”
5. Repeat for the remaining ports.
6. Click start and let it run. The process usually takes about 4-5 hours. In most cases you 145 it in the afternoon and can leave it overnight.

Clean Up and Data Acquisition

1. Remove the tubes by carefully unscrewing them and removing them from the ports.
2. Return or dispose your sample and clean out the tube using water and/or acetone and allow to air dry.
3. To obtain data, click on the report buttons at the top for each port.

4. When you open a report, there will be a button on the side that says “Save As”. Click on it and save the file as an excel sheet to the local disk in the DATA 1 folder or to a flash drive. (The flash drive will allow you to take the data with you.)
5. Cover the dewar with the foam piece or a piece of paper if there is liquid nitrogen still inside the dewar.
6. Fill out remaining information in the log book. Let Tatiana know if there are any issues.

APPENDIX D

VISCOMETER PROCEDURE

General Start Up (For cp-40 cone)

1. Make sure viscometer is level. Make sure bubble on top of unit is inside the circle.
2. Turn viscometer on. The switch is on the back.
3. Viscometer will prompt you to remove spindle and do auto-zero.
4. Remove plate and cone from viscometer.
5. Press button to start auto-zero.
6. When auto-zero is complete replace spindle.
7. Make sure viscometer has the correct spindle selected. Should say CP-40 in top right corner.
8. Add 0.5 mL of fluid to center of plate and reassemble. Try not to make contact with cone.

Operating Viscometer

1. To start rotation of cone, simply type in what rpm you want to set it to and hit next.
2. The sheer stress, sheer speed, and viscosity can be read off the display and toggled through by pressing “Select Display”.
3. Typically a range of sheer speed will want to be used to check for non-Newtonian behavior.
4. To turn off rotation either press “motor off” button or set RPM to “0”.

Shut down of Viscometer

1. Make sure motor is off.
2. Turn viscometer off.
3. Remove Plate and clean out fluid.
4. Gently wipe of cone and remove cone.
5. Finish cleaning cone.
6. Replace cone and plate.

Operating Water Bath.

1. Fill one liter beaker with water and place on hot plate.
2. Make sure tubing is set up for pump, fluid flows into viscometer through the bottom connection and out through the top connection.
3. Pump need to be placed below the beaker to maintain fluid pressure.

4. Run electrical leads to the variable voltage and current connections on transformer.
5. Set knobs to half of max voltage and current.
6. Make sure all tubing is connected and the two ends are submerged in the water.
7. Before you turn the pump on make sure that the tubing doesn't start to fly around and spray water everywhere. TH 147 HAPPEN IF YOU ARE NOT CAREFUL.
8. Place thermocouple for viscometer in the center of the water bath.
9. Turn on the hot plate and let water circulate and heat up. The hot plate can reach a range of 40 to 100 ^{o}C with a setting of 2.5 to 4.5.

NOTE if a different cone is used an additional start up procedure is required. This can be found in the appendix 1 of the Brookfield DV-II owners manual. It requires raising and lowering the cone.

APPENDIX E

Sonicator Microtip Operating Procedure

The microtip attachment is to be used when processing a sample of 5 to 50 mL in volume. Be sure to use a tall cylindrical vial to hold your sample. The microtip directs all of the sound waves DOWN, out of the tip. Thus a thin and tall vial is ideal when using the micotip.

Attaching microtip

1. Ensure sonicator unit is turned off before attaching microtip.
2. Lay sonicator flat on the lab counter.
3. Using wrench, remove the flat tip from the sonicator.
4. Using Ethanol or DI water, clean the threading to remove debris.
5. Attach microtip and tighten using wrench. (Do not use excessive force when tightening)

   Note: Be sure to inspect the microtip before proceeding to make sure it is clean and undamaged. Some of the microtips have visible wear and tear, these should not be used.

Using Sonicator

1. Prepare cooling bath for the sample.

   Note: Sonication produces excessive amounts of heat, this can cause oil to 'burn' and can also cause damage to the microtip. If a sample with a relatively low viscosity is being used an ice water bath is recommended. If a sample with a higher viscosity is being used a water bath is recommended and sonication should be done in 5-10 minute intervals to ensure extreme temperature are not reached. Sonication works by producing sound waves that cause small bubbles in the fluid

to form and collapse causing mixing. The higher the fluid viscosity the harder it will be to cause this to happen.

2. Place sample in ice bath and support by clamping it to the ring stand.

3. Clamp sonicator to ring stand so the tip is at least submerged ½ inch. (2 times tip diameter) Never allow the sonicator tip to touch the walls of the processing vessel. This WILL cause damage to the tip and can cause the vessel to break.

   Note: Never attach a clamp to any part of the sonicator except the convertor (the top and largest part of the sonicator). Attaching a clamp to the horn (immediately below convertor) can cause damage to sonicator. A stable set up is sitting sonicator on the black ring clamp (stop from falling down) and then attaching clamp to convertor (stop from sliding back and forth.

4. Turn sonicator on, set processing time and power setting.

   Note: Never use a power setting above 70% when operating the microtip. An operating value around 30-40% typically is enough. Start low and work up.

5. Start sonicator and watch the sample. There should be obvious fluid movement in the container. If not turn sonicator off and reposition.

   Note: For first time operating the microtip using a sample with no nanoparticles may be ideal. This will allow you to easily see the movement of the fluid in the container to understand how far down or up the tip needs to be.

6. Allow sonication to proceed. Typical processing lengths are 20-40 minutes total, depending on particle and fluid properties. During sonication it is considered good lab etiquette to try and suppress the loud piercing noise generated from the sonicator for the mental health of those around. Do so by placing a large cardboard box over the unit. If you are short, ask someone to help you with this so you don't knock over the sonicator or your sample.

   Note: If a very high pitch squealing noise is coming from the sonicator, turn sonicator off and ensure the microtip is securely attached to the horn and make sure the tip is not in contact with the sides of the vessel. If the sound still proceeds you may try a different microtip or different power amplitudes to see if this remedies the situation.

7. After sonication is complete turn sonicator off.

Clean Up

1. Ensure sonicator is turned off.
2. Remove sonicator from sample and wipe off micro tip.
3. Using the wrench remove the microtip and place back in lab drawer.
4. Reattach the flat tip and tighten using wrench.
5. Remove sample from clamp and empty the cooling bath in the sink. Make sure the lab bench is as clean or cleaner then the way you found it.

CURRICULUM VITAE
John L. Tatarko

University of Louisville
Department of Chemical Engineering
216 Eastern Parkway Louisville, KY 40292
jltata01@louisville.edu

Education

Ph.D. Chemical Engineering, University of Louisville 2015
Advisor: Prof. G.A. Willing

M.S. Electrical Engineering, University of Louisville 2013
Advisor: Prof John Lilly
Concentration: Controls

M.S. Chemical Engineering, Cleveland State University 2010
Advisor: Prof. Rolf Lustig
Thesis: *Thermodynamics of Fluid Phase Benzene via Molecular Simulation*

B. Chemical Engineering (cum laude), Cleveland State University 2008

Research Interests

Enhanced transport properties of nanoparticle-infused base oils

Non-linear regression analysis via self-organizing feature maps (SOFMs)

Process analysis, simulation, and control; fuzzy, robust, optimal, and minimum variance

Six-sigma methodology within the chemical process industry (CPI)

Positions

President/Owner, KMD Precisioneering 1978 to present

Served as project manager along with Pentair Corporation for the design, manufacture, and construction of all components for the first reverse-osmosis water desalinization plant for island nation of Trinidad-Tobago

Served as project manager along with Lorisal Corporation for the manufacture and construction of all components for a polyester spinning plant in Pakistan

Instructor, CHE 430 Computer Apps in Chemical Engineering 2015

Instructor, CHE 461 Process Control, U of L. 2014/2015

Teaching Assistant, Chemical Process Safety, (undergrad) U.of L. 2011

Instructor, ESC 120 Engineering Design, Cleveland State University 2009

Undergraduate Research Assistant 2008
Advisor: Prof. Rolf Lustig

Honors and Awards

Ohio Space Grant Scholar 2006-2008

University Fellow, University of Louisville 2011-2013

Tau Beta Pi 2007

Academic Excellence Award, Cleveland State University 2007

Professional Societies

AIChE

IEEE

ISA

Conferences and Proceedings

Midwest Thermodynamic Conference, Notre Dame University 2009

ACS Colloids and Surface Science Conference, Johns Hopkins University 2012
Presenter: *Heat Transfer Enhancement of PAO Motor Oil Infused with Cu nanoparticles*

AIChE National Conference 2013
Presenter: *A Different Look at Data Analysis Using Self-Organizing Feature Maps (SOFMs)*

Publications

1. John L.Tatarko, M. Nasser Sadaatzi, Kan Liu, and Gerold A. Willing
Department of Chemical Engineering, University of Louisville, Louisville, KY 40292

Heat transfer measurement of oil based copper nanofluids I: a novel approach to data analysis using dimensionless numbers.

Submitted to the Journal of Applied Physics

2. John L.Tatarko, M. Nasser Sadaatzi, and Gerold A. Willing
Department of Chemical Engineering, University of Louisville, Louisville, KY 40292

Heat transfer measurement of oil based copper nanofluids II: a different approach to data analysis using self-organizing feature maps, (SOFM).

Submitted to the Journal of Applied Physics

3. John L.Tatarko, Naethan Mundker, and Gerold A. Willing
Department of Chemical Engineering, University of Louisville, Louisville, KY 40292

Heat transfer measurement of oil-based copper nanofluids III: the use of CuO nanoparticles and Therminol 66 makes a difference.

Submitted to the Journal of Applied Physics